

Final Report for research entitled:
UAV Flight Control Using Distributed Actuation and Sensing

Under the direction:
Ndaona Chokani and Charles Hall, Jr.

This report contains research and documents produced under a research grant from the National Aeronautics and Space Administration. The report consists of this introduction and three Documents, a Master's Thesis, an AIAA Conference Paper, and an Update Report. The Thesis details work done on Tasks 1-6 and the results obtained. During the initial flight test attempts the UAV was damaged and the project was re-aligned with an emphasis on full scale wind tunnel testing in the NASA 12' tunnel. This work is detailed in the AIAA Paper and the subsequent update report.

| | |
|--|----|
| Distributed Actuation and Sensing on an Uninhabited Aerial Vehicle, Master's Thesis William Garrard Barnwell | 2 |
| Wind Tunnel Test of an RPV with Shape-Change Control Effector and Sensor Arrays, AIAA2004-5114 David L. Raney, Randolph H. Cabell, et. al. | 75 |
| UAV Flight Control Using Distributed Actuation and Sensing, Update Report S. Todd Lion | 87 |

ABSTRACT

Barnwell, William Garrard Distributed Actuation and Sensing on an Uninhabited Aerial Vehicle. (Under the direction of Dr. Ndaona Chokani)

An array of effectors and sensors has been designed, tested and implemented on a Blended Wing Body Uninhabited Aerial Vehicle (UAV). This UAV is modified to serve as a flying, controls research, testbed. This effector/sensor array provides for the dynamic vehicle testing of controller designs and the study of decentralized control techniques. Each wing of the UAV is equipped with 12 distributed effectors that comprise a segmented array of independently actuated, contoured control surfaces. A single pressure sensor is installed near the base of each effector to provide a measure of deflections of the effectors.

The UAV wings were tested in the North Carolina State University Subsonic Wind Tunnel and the pressure distribution that result from the deflections of the effectors are characterized. The results of the experiments are used to develop a simple, but accurate, prediction method, such that for any arrangement of the effector array the corresponding pressure distribution can be determined. Numerical analysis using the panel code CMARC verifies this prediction method.

Distributed Actuation and Sensing on an Uninhabited Aerial Vehicle

by

William Garrard Barnwell

A thesis submitted in partial fulfillment of
the requirements for the degree of
Masters of Science

Aerospace Engineering

North Carolina State University

2003

Approved by:

Dr. Ndaona Chokani
Chair of Supervisory Committee

Dr. Charles E. Hall, Jr.
Member of Supervisory Committee

Dr. Harvey J. Charlton
Member of Supervisory Committee

B i o g r a p h y

William Garrard Barnwell was born August 9, 1976 in Indianola, a small town in the Mississippi Delta. He has received his Bachelors and Masters of Science in Aerospace Engineering from North Carolina State University.

Acknowledgments

First, I would like to acknowledge my committee members. Dr. Chokani, my faculty advisor, is commended for his continual faith and support. Also I would like to recognize Dr. Hall who has served as co-investigator on the project and provided assistance on countless occasions. Also appreciation is given to Dr. Charlton for his devotion to mathematics and his adoration of literature.

Next, I would like to thank Stearns Heinzen for his unending support. He has been a wonderful teacher, mentor and friend.

Finally I would like to give my dedication to my fiancé and life partner Laura McCrain. Without her undying devotion and support none of this would have been possible. Thank you, Laura, may we wear white in the BR.

TABLE OF CONTENTS

| | <i>Page</i> |
|---|-------------|
| List of Tables..... | vi |
| List of Figures..... | vii |
| List of Symbols | ix |
| 1. Introduction | 1 |
| 1.1 Aircraft Morphing Concepts | 1 |
| 1.2 UAV Overview and Research | 1 |
| 1.3 Decentralized Control Techniques for Distributed Systems..... | 1 |
| 1.4 NASA Morphing Wing..... | 2 |
| 1.5 Objectives of Project..... | 4 |
| 2. Experimental and Numerical Approach..... | 5 |
| 2.1 Experimental Set-Up..... | 6 |
| 2.1.1 Wind Tunnel..... | 6 |
| 2.1.2 Instrumentation | 6 |
| 2.1.2.1 Pressure Measurement System | 6 |
| 2.1.2.2 Servo Serial Boards | 6 |
| 2.1.3 UAV BWB Delta..... | 7 |
| 2.1.4 Wing Panels | 7 |
| 2.1.5 Distributed Effectors and Sensors | 7 |
| 2.1.5.1 Effectors | 8 |
| 2.1.5.2 Sensors | 8 |
| 2.2 Computational Methods..... | 9 |
| 2.2.1 XFOIL..... | 9 |
| 2.2.2 CMARC..... | 9 |
| 3. Results and Discussion..... | 10 |
| 3.1 XFOIL Results | 11 |
| 3.1.1 Effect of Flap Deflection..... | 11 |
| 3.1.2 Effect of Reynolds Number..... | 12 |
| 3.1.3 Effect of Hinge Location..... | 12 |
| 3.1.4 Effect of Surface Geometry | 13 |
| 3.2 CMARC Results | 14 |
| 3.2.1 Control Power Analysis..... | 14 |
| 3.2.2 Pressure Characterization..... | 15 |
| 3.2.2.1 Single Effector Movement..... | 16 |
| 3.2.2.2 Multiple Effector Movement..... | 17 |
| 3.3 Wind Tunnel Results | 18 |
| 3.3.1 Single Effector Characterization..... | 18 |
| 3.3.2 Multiple Effector Characterization..... | 19 |

| | |
|---|----|
| 3.3.3 UAV Readiness for Flight Testing..... | 20 |
| 3.3.3.1 Effector Calibrations | 21 |
| 3.3.3.2 Comparison of Pressure Systems..... | 21 |
| 4. Concluding Remarks | 22 |
| 4.1 Summary of Results..... | 22 |
| 4.2 Continuing Research | 23 |
| 4.3 Recommendations for Future Work..... | 23 |
| 5. Tables | 24 |
| 6. Figures | 27 |
| 7. Bibliography | 61 |

LIST OF TABLES

| <i>Number</i> | <i>Page</i> |
|---|-------------|
| Table 1: Sensitivity Matrix from CMARC | 24 |
| Table 2: Sensitivity Matrix for Starboard and Port Wing Matrices of $\frac{d\Delta C_p}{d\delta_f}$ | 25 |
| Table 3: Calibrations for Effector Deflections from -15 to 15 degrees | 26 |

LIST OF FIGURES

| <i>Number</i> | |
|--|----|
| Figure 1: SMA Actuated Smart Wing Contoured Surface | 27 |
| Figure 2: Comparison of Contoured and Conventional Control Surfaces | 27 |
| Figure 3: CL vs. AOA Runs for Smart Wing and Conventional Surface | 27 |
| Figure 4: Cp Pressure Distribution for Smart Wing and Conventional Surface | 28 |
| Figure 5: Theoretical Effector Array | 29 |
| Figure 6: UAV BWB DELTA | 29 |
| Figure 7: Construction History of Outboard Wing Panels | 29 |
| Figure 8: Actuator Design - Deflected (left) and Undeflected (right) | 30 |
| Figure 9: Starboard Wing with Effectors Attached | 31 |
| Figure 10: Effect of Flap Deflection on Aerodynamic Performance | 31 |
| Figure 11: Effect of Reynolds Numbers on Aerodynamic Performance | 32 |
| Figure 12: Effect of Hinge Location on Aerodynamic Performance | 33 |
| Figure 13: XFOIL Analysis of Conventional and Contoured Surfaces | 34 |
| Figure 14: XFOIL Plot of Coefficient of Pressure vs. x/c for Contoured Airfoil | 35 |
| Figure 15: XFOIL Plot of Coefficient of Pressure vs. x/c for Conventional Airfoil | 36 |
| Figure 16: Elevator Control Powers | 36 |
| Figure 17: Steady State Roll Rates | 37 |
| Figure 18: CMARC Model of Outboard Wing Panel with Effector Deflection | 37 |
| Figure 19: Pressure Distribution from CMARC with an inset of a deflected effector | 38 |
| Figure 20: CMARC Pressure Response for Inboard Effector Movement (#3) | 39 |
| Figure 21: CMARC Pressure Response for Inboard Effector Movement (#6) | 40 |
| Figure 22: CMARC Pressure Response for Inboard Effector Movement (#10) | 41 |
| Figure 23: CMARC Sensitivity Coefficients | 42 |
| Figure 24: Port Wing in Wind Tunnel with Various Effector Arrangements | 43 |
| Figure 25: Pressure Response for Inboard Effector Movement (#3) | 44 |
| Figure 26: Pressure Response for Mid-Span Effector Movement (#6) | 45 |
| Figure 27: Pressure Response for Outboard Effector Movement (#10) | 46 |
| Figure 28: CMARC, Port, and Starboard Sensitivity Coefficients for Inboard Effector (#3) | 47 |
| Figure 29: CMARC, Port, and Starboard Sensitivity Coefficients for Mid-Span Effector (#6) | 48 |
| Figure 30: CMARC, Port, and Starboard Sensitivity Coefficients for Outboard Effector (#10) | 49 |

| | |
|---|----|
| Figure 31: Measured and Predicted Pressure Response for Sine Wave ($A = 15^\circ$, $\omega = 0.1$) | 50 |
| Figure 32: Measured and Predicted Pressure Response for Sine Wave ($A = 15^\circ$, $\omega = 0.25$) | 51 |
| Figure 33: Measured and Predicted Pressure Response for Sine Wave ($A = 15^\circ$, $\omega = 0.5$) | 51 |
| Figure 34: Measured and Predicted Pressure Response for Sine Wave ($A = 15^\circ$, $\omega = 0.75$) | 52 |
| Figure 35: Measured and Predicted Pressure Response for Constant Deflection ($A = -10^\circ$) | 53 |
| Figure 36: Measured and Predicted Pressure Response for Constant Deflection ($A = -15^\circ$) | 54 |
| Figure 37: Measured and Predicted Pressure Response for One-Up-One-Down Deflection ($A = 4^\circ$) | 55 |
| Figure 38: Measured and Predicted Pressure Response for One-Up-One-Down Deflection ($A = 12^\circ$) | 56 |
| Figure 39: BWB DELTA with Distributed Effector Wings | 57 |
| Figure 40: Calibrations for Port Wing | 58 |
| Figure 41: Comparison of ESP vs. Scanivalve | 59 |
| | 60 |

LIST OF SYMBOLS

Roman Symbols

| | |
|------------------|--|
| b | Wing Span |
| c | Chord Length |
| C_l | Two-dimensional lift coefficient |
| C_L | Three-dimensional lift coefficient |
| $C_{l_{\alpha}}$ | Change in lift coefficient due to aileron deflection |
| C_{l_p} | Change in lift coefficient due to roll |
| C_m | Pitching moment coefficient |
| $C_{m_{\alpha}}$ | Change in pitching moment coefficient due to elevator deflection |
| C_{m_a} | Change in pitching moment coefficient due to angle of attack |
| C_p | Pressure coefficient |
| L/D | Lift-to-drag ratio |
| P_s | Steady state roll rate |
| Re | Reynolds Number |
| V_∞ | Freestream velocity |

Greek Symbols

| | |
|------------|---------------------------|
| α | Angle of attack |
| δ_a | Aileron deflection angle |
| δ_e | Elevator deflection angle |
| δ_f | Flap deflection angle |
| μ | Viscosity |
| ρ | Density |

Abbreviations

| | |
|------|--------------------------------|
| BWB | Blended Wing Body |
| UAV | Uninhabited Aerial Vehicle |
| MEMS | Microelectromechanical Systems |
| SMA | Shape Memory Alloy |

1. INTRODUCTION

1.1 Aircraft Morphing Concepts

The National Aeronautics and Space Administration (NASA) Aircraft Morphing program has the objective of integrating research from a broad range of disciplines in order to incorporate smart technologies into high payoff aircraft applications.¹ Smart technologies may be defined as embedded actuation, sensing, and control logic that are tightly coupled in a feedback loop. Therefore, the primary focus for the Morphing program is to develop closed-loop devices having dynamic actuation, local sensing, and feedback control. Consequently, a combined approach to control systems and system identification is being used in the Morphing program to address the control laws and controller responses required for the individual devices, as well as addressing the global requirements for distributed arrays of devices that are used to achieve an overall system benefit.² Thus, it is within this framework that NC State and NASA have partnered to develop a flying controls test bed that is equipped with distributed actuation and sensing.

1.2 UAV Overview and Research

Uninhabited Aerial Vehicles (UAVs) are used for a wide range of purposes including military, civilian and research. In military applications, the UAV can be used for in-field reconnaissance or high altitude surveillance.^{3,4} The U.S. military is also developing Uninhabited Combat Aerial Vehicles (UCAVs) to complement and/or replace fighter aircraft.^{4,5} Civil use of UAVs include aerial photography and observation of traffic patterns.^{6,7} In agriculture UAVs can be used to inspect crops and provide local applications of pesticide and/or herbicides.^{8,9} High altitude, long range UAVs also serve as upper atmospheric weather stations.¹⁰ Finally the use of highly instrumented UAV's in research applications provides a

quick, safe and inexpensive method to validate a wide variety of novel designs and concepts.^{11,12}

New flow control methods are under investigation to reduce fuel consumption, increase range/endurance, increase control authority and enhance maneuverability throughout the entire flight envelope of an air vehicle.¹³ This approach is in contrast to traditional, passive control approaches that have inherently poor performance at off-design conditions. In general, active flow control devices can yield more reduced drag, increased lift and better control of unsteady aerodynamics than passive devices.¹⁴

Recent activity at NC State's Flight Research Laboratory has demonstrated the advantages of highly instrumented UAVs in validating flow and flight control technologies under actual flight conditions.^{15,16} In the current work an existing UAV platform is modified to evaluate multiple controller designs. An innovative replacement for traditional flaps (ailerons, elevators, rudders, etc.) is used in order to gain enhanced control of the aircraft.

1.3 Decentralized Control Techniques for Distributed Systems

New developments in decentralized control techniques have provided methods to control distributed arrays with a large number of individual elements. These techniques have been useful in a wide variety of applications. Studies have shown that the decentralized control methods provide a viable option for distributing air/ground traffic separation.¹⁷ Several studies have investigated the robust control of multiple vehicles, including UAVs, traveling in formation and show that a decentralized control method provides optimal control while reducing the complexity of the control algorithm.^{11,18} Furthermore, recent discoveries in material science and fluidics have been used to create a variety of shape-change and fluidic effector devices to enable new approaches to aerospace vehicle flight

control. Microelectromechanical systems (MEMS) make feasible the concept of combining actuation, sensing, computing, and telecommunications to produce a very large array of distributed configurations with unprecedented capabilities for control.¹⁹ Future aerospace vehicles might use distributed arrays with hundreds of such devices for stabilization and maneuver control, thereby augmenting or replacing conventional ailerons, flaps and/or rudders.²⁰

The underlying theme in each of the distributed systems is that standard control techniques have severe limitations because the overall system is rich and complex, and requires high levels of connectivity and massive computations.²¹ However, many systems contain similar elements that interact with their nearest neighbor in a simple and predictable fashion. The goal of developing decentralized control techniques is to obtain tractable algorithms for controlling the simple systems and then applying the technique to a more vast, overall scheme.

The current work develops a test-bed with a distributed actuation and sensing suite that provides the capability to test and evaluate a large number of controllers and control methods, such as decentralized control. Control objectives include active separation control, stabilization and maneuver control, disturbance rejection or upset recovery, mission-adaptive performance enhancement, and failure accommodation.¹³ In addition to the aforementioned control objectives, reduced fuel consumption, enhanced maneuverability and reconfigurability are potential benefits of distributed effector and sensor arrays.^{24,25} Sophisticated controller designs using elegant inputs, such as modal shapes that only vary amplitude and frequency across the effector array will be used to provide multi-axis aircraft control.

1.4 NASA Morphing Wing

The Smart Wing program was developed and sponsored by DARPA, AFRL and NASA. The program evaluated smart materials through a multi-disciplinary investigation for high payoff aircraft.²² Phase 1 of the Smart Wing program concluded with wind tunnel testing in 1997. One aspect of the Smart Wing design was a Shape Memory Alloy (SMA) actuated trailing edge device that replaced a traditional control surface. This design produced a contoured wing, or a hingeless control surface (Figure 1).²³ The benefits of a contoured wing are illustrated in Figure 2. The conventional hinged flap, due to its abrupt change in curvature, is more prone to separation than the smooth transition of the contoured control surface. Figure 2 shows that the contoured wing yields a higher value of the maximum lift coefficient, $C_{L_{max}}$, thus increasing the stall envelope of the aircraft. Another benefit is an increase in the upper corner of the drag bucket, which indicates an increase in L/D_{max} .

Wind tunnel testing of the Smart Wing was conducted at NASA Langley's 16 ft Transonic Dynamic Tunnel on a 16% scale F/A - 18 E/F model. The model was tested with both the traditional, hinged control surfaces and the contoured, SMA actuated surface. The Smart Wing showed significant aerodynamic improvements.²⁴ Figure 3 shows that for any given angle of attack, α , there is an increase in the lift coefficient, C_L , resulting in 8% increase in lift. The pressure distribution around the airfoil, Figure 4, shows that the Smart Wing produces increased amount of suction on the upper surface near the trailing edge of the airfoil. This increase in negative pressure directly contributes to the increased lift. The Smart Wing also shows improved aerodynamic performance by using the contoured wing design.

1.5 Objectives of Project

The current project develops a UAV test-bed to test decentralized control methods using a distributed array of contoured control surfaces. The effector and sensor suite are designed to evaluate, in the future, a wide range of control objectives. The implementation of the distributed effector array is illustrated in Figure 5. The continuous control surface proved very difficult to manufacture; therefore, in the current work the effector array is approximated with a series of segmented and independently actuated effectors. Surface pressure measurements will be used as sensors for the array. A recent study has shown that as few as four pressure measurements on an airfoil can provide information on the overall lift.²⁵ Thus the pressure sensors are designed to provide feedback in the controllers. Each effector is paired with a single sensor; therefore, the effector/sensor pair forms a subsystem. Each subsystem is first characterized and then the subsystems are used to predict the response for the more complete effector/sensor array.

2. EXPERIMENTAL AND NUMERICAL APPROACH

2.1 Experimental Set-Up

2.1.1 Wind Tunnel

The NC State Subsonic Wind Tunnel is a closed return wind tunnel with a test section 32" high * 45" wide * 46" long. The wind tunnel operates at a maximum dynamic pressure of 12 lb/ft²; thus the maximum velocity is approximately 85 ft/s. The tunnel is equipped with Plexiglass® side walls at the test section. A solid door was constructed to replace one of the Plexiglass® side walls. This door is equipped with a 6" offset splitter plate onto which the model is mounted. The splitter plate is used to eliminate the influence of the wind tunnel walls' boundary layer on the model and to position the model in the center portion of the test section.

2.1.2 Instrumentation

2.1.2.1 Pressure Measurement System

Two pressure scanning devices are used to measure the surface static pressures on the model. A Scanivalve® system equipped with 96 channels and a $\pm 3.5''$ H₂O transducer is used as the primary pressure measurement system. A Pressure Systems, Inc. Electronic Scanning Pressure (ESP) module was also used. The ESP module has 16 independent $\pm 10''$ H₂O transducers that are contained within a lightweight and compact case; this module is capable of measuring up to 32 channels.

2.1.2.2 Servo Serial Boards

Servo serial boards, manufactured by BASIC-X™ are used to command the positions of the servos/effectors. The boards allow the command of 256

positions for each servo. Up to eight serial servo boards can be linked together therefore providing independent control of up to 64 servos using a single serial connection.

2.1.3 UAV *BWB Delta*

The testbed is the UAV *BWB (Blended Wing Body) DELTA* that was designed, built and flight tested at NC State (Figure 6). The flying wing platform is similar to the design of the NASA BWB.²⁶ The root chord and tip chord are 58" and 5 1/4", respectively. The 9.5' wingspan aircraft is powered by an Aviation Microjet Technology™ (AMT) mini-turbojet engine that is rated at 18-lbf static thrust.^{27,28} The cruise and stall speeds are 120 ft/s and 45 ft/s, respectively. The UAV has no landing gear; instead the aircraft is dolly-launched and skid recovered. The aircraft has a dry weight of 30 lb. with a payload capacity of 15 lbs. *BWB DELTA* is an ideal candidate for the effector array because the flying wing design allows the trailing edge surfaces of the aircraft to provide pitch and/or roll control. The UAV *BWB DELTA* has removable outboard wing panels; therefore, new wing panels equipped with the distributed effectors were constructed.

2.1.4 *Wing Panels*

The outboard wing panels of the aircraft have a 21" root chord with a 5 1/4" tip. The airfoil section is a NACA 0015. The wing span is 31 1/4". Figure 7 shows details of the wing during construction. The skins for the wings are made of a wet-laminate fiberglass/graphite composite which incorporates a 1/8" Korex™ honeycomb core. The internal formers are 1/8" birch plywood. Aluminum bars are integrated into the skin to provide attachment points for the effectors. A hatch provides access to all of the servo motors, effectors, and pressure ports.

Twelve effectors, adjacent to each other, are installed on each wing. The effector #1 is at the root and effector #12 is 18" from the root. Because of the thin cross-section at the most outboard portion of the wing, a conventional hinged control surface is installed. A second conventional control surface is located on the main body section of the aircraft. Thus the arrays of distributed effectors are backed-up by conventional surfaces which give redundancy to the control surfaces of the aircraft. Figure 8 shows the starboard wing with the complete distributed effector array.

Each outboard wing panel equipped with the distributed effectors, servos and other hardware has a weight of 3.5 lbs. The baseline wing panels have a weight of 2.25 lbs. Thus, the net increase in the weight of the wings is 1.5 lbs. There are additional power requirements to operate the 24 servos (one for each effector); however, the additional batteries are used to replace the ballast that is required in the nose of the aircraft. Thus the overall weight increase of the modified wing panels and its accessories is less than the available payload weight of 5 lbs.

2.1.5 Distributed Effectors and Sensors

2.1.5.1 Effectors

The arrays of independently actuated surfaces, also termed effectors, are designed to operate with the same bandwidth (1-2 Hz) and maximum deflection ($\pm 15^\circ$) as the conventional control surfaces. Therefore the modified vehicle can operate similar to the baseline vehicle when the effectors are deployed as a conventional surface.

The actuation of the effectors is provided by commercially available, off-the-shelf servo motors, Hobbico™ CS-5 nano-servos. The design of the effectors incorporates a hingeless, contoured control surface. Each effector is comprised of two rectangular elements of thin spring steel having dimensions of 0.007"

(thickness), 1.5" (width) and 4" (length), one each on the upper and lower surfaces. The effectors are deflected by the servos through a pull-pull wire linkage; the opposing surface restores the actuated surface to its neutral position. An undeflected and deflected full-scale prototype of an effector is shown in Figure 9.

2.1.5.2 Sensors

An array of 24 surface pressure taps (12 taps per wing) is used to monitor the deflections of the effectors. One pressure tap, 0.040" in diameter, is located 4.05" from the trailing edge of each effector. The pressure taps are equally spaced at intervals of 1.5" in the spanwise direction with the first pressure tap located 0.75" from the root chord. Therefore there is one pressure tap located immediately forward of each effector. The pressure tubulations are connected to the pressure scanning system through 0.040" diameter nylon tubing.

2.2 Computational Methods

2.2.1 XFOIL

The effect of Reynolds number, flap hinge location, and flap deflection are examined using XFOIL. XFOIL is a two-dimensional inviscid analysis code based on the linear vorticity stream function.²⁹ In the present work an airfoil, whose undeflected cross-section is the NACA 0015, is examined. The CAD program, Unigraphics™, is used to generate undeflected and deflected trailing edge airfoil sections. The contour of the modified wing panel is modeled by the deflected trailing edges of the airfoil section. A range of deflected airfoil sections with hinge locations of $x/c = 0.4-0.9$ and flap deflection angles of 10-60° are examined.

2.2.2 CMARC

The aerodynamic analysis code CMARC is used to examine the pressure distribution on the UAV *BWB DELTA* equipped with the array of distributed effectors. CMARC is a three-dimensional, inviscid, panel code method based potential flow theory.³⁰ The geometry of the UAV, with and without deflection of the effectors, is modeled in Unigraphics™. A representative aerodynamic model of the wing panels is shown in Figure 10; the inset shows a close-up of the deflected effectors.

3. RESULTS AND DISCUSSION

Numerical and experimental results of the performance of the distributed effector and sensor are presented in this chapter. The performance is first examined using the two-dimensional analysis code XFOIL (3.1); then a three-dimensional analysis using CMARC (3.2) is presented; finally the results of an experimental wind tunnel investigation are presented (3.3).

3.1 XFOIL Results

The outboard wing panel of UAV *BWB DELTA* is tapered. This variation in the geometry results in different cross-sections across the span of the effector array. XFOIL provides a quick method to isolate the effect of the varying geometry by examining two-dimensional, airfoil, cross-sections of the wing. This analysis delineated the influence of changing flap deflection, Reynolds Number and hinge location. Also the potential aerodynamic benefits of a contoured design versus a conventional hinged flap are examined.

3.1.1 Effect of Flap Deflection

Figure 11 shows the effect of changing flap deflection, δ_f . Three airfoils with deflections of 10° , 15° and 20° deflections are presented. The hinge location is $x/c = 0.7$ and the Reynolds number is 1×10^6 . The lift and pitching moment coefficients are plotted versus angle of attack, α . As the deflection angle is increased, the C_l is larger for a given angle of attack, while $C_{l,max}$ is unchanged. Thus, the flow over the effectors is neither separated nor stalled even at large deflection angles. This is verified by the fact that the pitching moment coefficient remains constant for all cases.

3.1.2 Effect of Reynolds Number

Figure 12 shows the results for the change in Reynolds number for an airfoil with a deflection of 15° and hinge location $x/c = 0.7$. Reynolds Number is defined as:

$$Re = \frac{\rho V c}{\mu} \quad (3.1)$$

Thus the chord length, c , is proportional to the Reynolds Number. The chord length of the airfoil cross-section varies from 19" (inboard) to 8" (outboard) due to taper in the wing. The Reynolds Number varies from 1×10^6 - 2.5×10^6 across the span of the effector array at the cruise velocity of the aircraft (120 ft/s). The results show that although the Reynolds number changes considerably there is little effect on the aerodynamic performance of the airfoil. The section lift coefficient, C_l , differs only slightly near stall and the pitching moment coefficient, C_m , shows very little deviations for all cases.

3.1.3 Effect of Hinge Location

Figure 13 shows XFOIL results for airfoils with various hinge locations. Each effector has a different hinge location, because the chord of the wing changes, but the length of each effector is 4". Thus the hinge location varies from $x/c \approx 0.8$ for the inboard effector to $x/c \approx 0.5$ for the outboard. Each of the airfoils has a 15° deflection with a Reynolds Number of 1×10^6 . Since the chord length is proportional to increasing the Reynolds Number, Figure 12, shows varying the chord length will not change the results.

The results show that the outboard effectors in the array provide a greater C_l for a given angle of attack, α . However, this also suggests the onset of stall, defined as $C_{l,\max}$, will occur at a lower α for the outboard effectors. Therefore, although the outboard effectors are the most effective, they stall first, and the aircraft is more susceptible to wing tip stall. This tip stall of the aircraft has been has been

previously observed in the wind tunnel analysis of a sub-scale model and in the initial vehicle flight testing; the present XFOIL analysis clarifies these previous results.²⁸ The only slight variations in pitching moment due to the hinge location occur at negative angles of attack that are unobtainable by the aircraft; it is thought that this variation does not change with hinge location.

3.1.4 Effect of Surface Geometry

The NACA 0015 airfoil with a conventional, hinged control surface and the contoured airfoil are next examined. Figure 14 shows the comparison for a 15° flap deflection at a Reynolds Number of 1×10^6 and a hinge location of $x/c = 0.7$. C_l and C_m of the contoured airfoil are increased compared to the conventional airfoil at any given angle of attack; therefore, there is a clear benefit in the performance of the airfoil that utilizes the contoured trailing edge. Similar results are also obtained by varying flap deflection, Reynolds Number and hinge location for the two airfoils. These results agree very well with the wind tunnel observations in the Smart Wing program (Figure 3). The wind tunnel results for the Smart Wing show an increase in lift coefficient of approximately 8%; whereas, the XFOIL analysis shows improvements of approximately 10%. The improvement in pitching moment also suggests that there are considerable improvements in the control authority of the contoured control surface.

Although the magnitude increase in C_l compare well, the pressure distributions from the XFOIL analysis differs from the wind tunnel results for the Smart Wing. The Smart Wing shows an overall increase in suction mainly due to an increase at the trailing edge location (Figure 4). However, the results from XFOIL show that the suction spike produced by the sharp transition at the flap deflection is flattened out, while there is an overall increase in the magnitude of the upper surface pressures (Figure 15 and Figure 16). This overall increase in magnitude is what accounts for the lift improvement for the contoured airfoil.

The improvement in lift is significant, and possibly could be even greater if the gap between the traditional surface and airfoil is also modeled. The gap may cause greater flow separation, and degrade the performance; whereas, the modified airfoil very closely represents the manufactured design.

In summary, the analysis shows that the effectors can be used in a wide range of conditions without degradation to the performance. The study further suggests that the array of effectors will have additional aerodynamic benefits due to the contoured geometry of the design.

3.2 CMARC Results

3.2.1 Control Power Analysis

The CMARC simulations are used to provide an inviscid, three-dimensional analysis of the UAV. The CMARC analysis reported in Ref(27) provides the baseline information for control power effectiveness of the control surfaces. The trailing edge surfaces of the UAV are designed to provide pitch and roll control; therefore, the two figures of merit used to evaluate the control power effectiveness for roll and pitch are p_{ss} and $d\alpha/d\delta_e$, respectively. The following equations are used to calculate the control power estimates:

$$\text{Elevator Control Power} = \frac{d\alpha}{d\delta_e} = \frac{C_{m_{de}}}{C_{m_a}} \quad (3.2)$$

$$\text{Steady State Roll} = p_{ss} = -\frac{2C_{l_{da}} V_\infty}{C_{lp} b} \Delta\delta_a \quad (3.3)$$

Previous UAV research at NC State has shown good aircraft handling qualities are obtained for values of p_{ss} near $360^\circ/\text{s}$ and $d\alpha/d\delta_e$ between 1 - 2.³¹

The control power of the effector array, predicted by CMARC analysis, ascertained that the modified control surfaces can provide adequate control of the aircraft.³² The analysis determined the amount of control power the effector array could provide without the assistance of the conventional surfaces. The pitch and roll authority the baseline vehicle, modified vehicle, and the effector array are shown in Figure 17 and Figure 18. The results show the vehicle outfitted with the effector array provides similar control authority to the baseline vehicle. Therefore, the modified vehicle with the effectors deployed as conventional surfaces result in handling that is similar to the baseline vehicle. A modal deflection, where the spatial distribution of tip deflections form a sine wave whose peak amplitude is 15°, is also examined. The control power is comparable to that of the baseline vehicle. Figure 17 and Figure 18 also show the control power estimates using only the effector array; it is seen that the effector array provides up to half the control power.

The effector array provides a good measure of pitch and roll authority without use of the conventional surfaces. During a flight test scenario all surfaces are used in a conventional manner for the more difficult maneuvers such as takeoff, approach and landing. Once a holding flight pattern is established at altitude, the conventional surfaces are disabled and the ability of the effector array to navigate the aircraft and perform simple maneuvers can be examined. Following the flight test the conventional surfaces can be re-engaged and the vehicle landed with a conventional control surface configuration.

3.2.2 Pressure Characterization

Figure 10 shows the CMARC panel model; in the inset of a close-up of a deflected effector is shown. The symmetry along the centerline of the aircraft simulates the presence of the sidewall in the wind tunnel tests. The CMARC model of the wing determined the pressure response to a single effectors

movement. Finally, a sensitivity matrix related the pressure response for multiple effectors movements.

3.2.2.1 Single Effector Movement

CMARC yields predictions of the aerodynamic coefficients, such as lift coefficient by calculating the pressure at each panel and then integrating to find the aerodynamic coefficients. Therefore, the pressure at the panel nearest to the location of the pressure sensor can be compared to the measurement of the pressure sensor.

Figure 19, shows a plot of the CMARC pressure distribution; the inset shows effector #3 at a 10° deflection. CMARC analysis with no effector deflections provides the baseline data. The baseline data set is subtracted from the predicted pressure with the deflected effectors. The baseline data is used as a reference to determine the net change in pressure due to the displacement of the effectors. The following equation is used to quantify the pressure change, ΔC_p ,

$$\Delta C_p = C_{p, \text{Recorded}} - C_{p, \text{Baseline}} \quad (3.4)$$

The change in pressure on all sensors is measured for +5° and +10° deflections of each effector. Since the wing has a symmetric airfoil section, the pressures on the upper and lower surface for both positive and negative deflections are obtained in a single run. Figure 20, Figure 21 and Figure 22 show the pressure response for deflections of an inboard (#3), a mid-span (#6), and an outboard effector (#10). In general, the change in pressure varies linearly with deflection.

Thus, the pressure response to a single effector at any deflection angle can be predicted. It is observed that the sensor nearest to the actuated effector is most sensitive to the deflection. This sensitivity decreases for sensors further away

from the actuated effector; the sensitivity is negligible more than three sensors away from the actuated effector.

3.2.2.2 Multiple Effector Movement

The change in pressure due to the actuation of a single effector, $\frac{d(\Delta C_p)}{d\delta_f}$, is the slope of the linear fit shown in Figure 20-Figure 22. These slopes, sensitivity coefficients, are plotted in Figure 23 for three representative cases. They can also be summarized in a matrix of the form:

$$A = \begin{matrix} a_{11} & a_{12} & \cdots & a_{1N} \\ a_{21} & a_{22} & \cdots & a_{2N} \\ \vdots & \vdots & \ddots & \vdots \\ a_{N1} & a_{N2} & \cdots & a_{NN} \end{matrix} \quad (3.5)$$

where $a \equiv \frac{d(\Delta C_p)}{d\delta_f}$, and the row and column numbers represent the effector and sensor numbers, respectively. The sensitivity coefficients derived in this manner from the CMARC analysis are shown in Table 1. The results in Table 1 and Figure 23 confirm that the most sensitive sensor is that which is nearest to the actuated effector. Also, the neighboring sensors equidistant to the actuated effector have approximately the same response to deflection of the effector.

The results above also suggest that the distributed actuation and sensing array could be used for failure monitoring and fault detection. Specifically, each effector configuration is uniquely related to the pressure distribution of the sensors. Therefore, for a given effector configuration, an inconsistency in the pressure distribution can be used to identify a faulty sensor. Conversely for a

measured pressure distribution, an inconsistent effector indicates the possible failure of an effector.

3.3 Wind Tunnel Results

Figure 24, shows a representative series of effector configurations in the wind tunnel that were evaluated during the testing. Three modal shapes with varying spatial frequency and a one-up-one-down configuration are shown. The purpose of the wind tunnel tests is to access the ability to characterize the pressure response due to the actuation of a single effector and then for actuation of multiple effectors.

3.3.1 *Single Effector Characterization*

Initially the wind tunnel experiments followed the same test matrix as the CMARC analysis. A single effector was deflected over a range of angles and the pressure response was measured. Figure 25, Figure 26 and Figure 27 show the results for a representative inboard (#3), mid-span (#6) and outboard (#10) effector moved through a $\pm 15^\circ$ degree sweep. The effectors are displaced with two degree increments to provide good resolution for the linear curve fit. The results are similar to the CMARC simulations. The change in pressure with respect to deflection of an effector is linear. The magnitudes of the pressure changes are also comparable to the CMARC analysis. As was previously observed the largest sensitivity is measured at the sensor closest to the actuated effector. The neighboring pairs of equidistant also show a similar response. The slopes of the linear fit to the data are summarized in the sensitivity matrices shown in Table 2.

The sensitivity coefficients from the CMARC analysis and the wind tunnel results are shown for three representative cases in Figure 28, Figure 29 and Figure 30. The results from the wind tunnel show that the CMARC simulations over predict

the pressures for the sensor that is closest to the actuated effector, but at the neighboring sensors the experiment and CMARC are in good agreement. The source of error could be attributed to the wake separation between the main wing and the actuated effector in the CMARC modeling. Nonetheless, the results provided a method to estimate the pressure change due to the actuation of a single effector using experimental or numerical data.

3.3.2 Multiple Effector Characterization

The effect of flap deflection on the change in pressure can be written in matrix form as:

$$Ax = b \quad (3.5)$$

The sensitivity coefficients a_{mn} in matrix A are given in Table 1 and Table 2 for the CMARC analysis and the wind tunnel experiment, respectively. The vectors x and b are given as

$$x = \begin{matrix} \delta_{f1} \\ \delta_{f2} \\ \vdots \\ \delta_{f(N-1)} \\ \delta_{fN} \end{matrix} \quad (3.6)$$

and

$$b = \begin{matrix} \Delta C_{P1} \\ \Delta C_{P2} \\ \vdots \\ \Delta C_{P(N-1)} \\ \Delta C_{PN} \end{matrix} \quad (3.7)$$

where x is a vector of flap deflections and b is a vector of change in pressure coefficient. The matrix equation therefore provides a method to combine the effects of the actuation of a single effector into the actuation of multiple effectors.

Figure 31Figure 38 show the predicted and measured pressure response for several commanded effector deflections. The prediction method is evaluated in each wing for several effector deflections including modal shapes with varying frequency, constant deflection angles, and one-up-one-down configurations. The prediction method uses Equation 3.5 to estimate the pressure response. The results show that the linear combination of the single effectors provides a reliable prediction for the multiple effector deflections for a range of effector deflections.

The above results show that the distributed effector/sensor array has the capability to meet many of the proposed mission objectives. All of the elements for closed loop control within the bandwidth limitations of the sensors and actuators are in place. Specifically, for a given effector position there is a measurable response from sensors. Therefore effectors can be commanded to a desired configuration whose resultant pressure distribution optimizes a particular flight condition, such as maximum L/D. The feedback can be potentially used for stabilization and maneuver control, disturbance rejection or upset recovery. The overall performance of the vehicle can be improved because the effector array can be actively controlled to optimize several phases of the flight regime, such as take-off, landing and cruise.

3.3.3 UAV Readiness for Flight Testing

The distributed effector and sensor array has been designed, manufactured, tested and installed. Figure 39 shows UAV *BWB DELTA* equipped with the distributed effector and sensor array. The UAV is therefore ready to enter the

flight testing phase of the project. Final evaluations of the system which included effector calibrations and comparison of the in-flight and wind tunnel pressure monitoring systems have also been conducted.

3.3.3.1 Effector Calibrations

A servo is employed to actuate each effector. The deflection angle, for a given servo position may differ; due to slight manufacturing inconsistencies, physical taper in the wing and the varying tension in the wire linkages. Therefore, a calibration of servo position versus deflection angle was made for each effector. Figure 40 shows a graph of the calibrations for the port wing. Effectors 1-6 have a slope of equal magnitude, but opposite sign, of effectors 7-12; this is because the separate banks of servos are mounted in opposite directions (Figure 7). Table 3 summarizes the calibration results for both wings. These calibrations are incorporated into a look-up table that may be used in a flight computer system to command an effector to a specific deflection angle.

3.3.3.2 Comparison of Pressure Systems

Figure 41 shows a comparison of the measured pressures using the two pressure monitoring systems used during the wind tunnel testing. The Scanivalve™ system is a mechanically multiplexed, pressure system permanently mounted the wind tunnel; the ESP module is a compact lightweight, electronically multiplexed system that will ultimately be used for in-flight pressure measurement. The results show that both systems provide identical results. Thus, the ESP module is suitable to be used as the pressure monitoring system during the flight testing portion of the project.

4. CONCLUDING REMARKS

4.1 Summary of Results

This study examines the effectiveness of multi-axis control of a UAV using a distributed actuation and sensing array that was designed, manufactured and analyzed. XFOIL and CMARC are used to computationally evaluate the design, and then wind tunnel tests are used to experimentally validate the design.

XFOIL provides a two-dimensional numerical analysis of the effects of flap deflection, Reynolds Number, and hinge location. This analysis is used to demonstrate the performance benefits of a contoured surface in the design of the effectors. The distributed array consists of 24 effectors that is 12 on each wing. The resulting effector is comprised of two plates of spring steel having dimensions 4" (chord) x 1.5" (span) x 0.007" (thickness). The effectors are actuated by a hobby servo via antagonizing pull-pull linkages. The pressure sensors, centered at the base of each effector, are located on the upper surface of the wing. An array of 24 pressure sensors provides feedback information for the system.

Subsequent three-dimensional analysis using CMARC provides comparisons of the control authority for the baseline vehicle equipped with conventional surfaces to the control authority of the modified vehicle equipped with the effector array. The modified vehicle has comparable control authority in addition to the advantages of distributed effectors. These advantages include fault tolerance, failure monitoring, and aeroelastic tailoring.

Wind tunnel testing provides an experimental evaluation of the performance of the effector array. The measured effects of the deflections compare well with the

CMARC simulations. The simulated and measured pressures, in response to the deflections of a single effector, are used to develop a simple but accurate method to determine the pressure distribution that results from deflections of multiple effectors.

4.2 Continuing Research

At the time of writing this thesis, wind tunnel testing of the fully equipped UAV is underway at the NASA-Langley 12' Wind Tunnel. The purpose of the test is to access the static and dynamic performance of the actuation and sensing suite. Preliminary results are encouraging and indicate that flight testing would be beneficial.

4.3 Recommendations for Future Work

Following the wind tunnel testing at NASA the UAV will be readied for flight testing. The present study and the wind tunnel tests at NASA provide a experimental and numerical database that can be used as the basis for multiple controller designs. The envisaged flight test plan includes the demonstration of closed loop, multi-axis control using the distributed effector and sensor arrays.

5. TABLES

Table 1: Sensitivity Matrix from
CMARC

| Sensor # \ Effector # | 1 | 2 | 3 | 4 | 5 | 6 | 7 | 8 | 9 | 10 | 11 | 12 |
|-----------------------|-------|-------|-------|-------|-------|-------|-------|-------|-------|-------|-------|-------|
| 1 | 64.80 | 38.72 | 20.48 | 12.64 | 8.88 | 6.88 | 4.16 | 4.12 | 3.48 | 2.92 | 2.50 | 2.96 |
| 2 | 41.00 | 49.15 | 37.86 | 18.44 | 11.30 | 8.14 | 4.74 | 4.62 | 3.86 | 3.16 | 2.72 | 3.18 |
| 3 | 21.32 | 33.37 | 94.88 | 39.48 | 17.74 | 10.94 | 5.80 | 5.38 | 4.30 | 3.48 | 2.92 | 3.40 |
| 4 | 13.18 | 16.80 | 38.02 | 85.96 | 35.78 | 17.92 | 7.86 | 6.64 | 5.06 | 3.90 | 3.14 | 3.64 |
| 5 | 9.26 | 10.11 | 17.34 | 34.10 | 54.02 | 37.70 | 13.10 | 9.02 | 6.36 | 4.72 | 3.62 | 4.12 |
| 6 | 7.08 | 7.12 | 10.54 | 17.46 | 35.74 | 62.08 | 27.70 | 14.08 | 8.74 | 6.04 | 4.48 | 4.92 |
| 7 | 5.58 | 5.22 | 6.66 | 8.66 | 12.46 | 23.64 | 78.32 | 45.68 | 20.60 | 11.82 | 7.84 | 7.90 |
| 8 | 4.60 | 4.25 | 5.20 | 6.34 | 8.06 | 11.64 | 27.72 | 95.80 | 48.52 | 20.76 | 11.74 | 10.52 |
| 9 | 4.14 | 3.72 | 4.44 | 5.18 | 6.14 | 7.66 | 9.22 | 30.36 | 94.94 | 48.50 | 20.96 | 15.66 |
| 10 | 3.86 | 3.43 | 4.06 | 4.52 | 5.18 | 6.06 | 5.80 | 11.54 | 30.24 | 95.88 | 48.86 | 26.70 |
| 11 | 4.00 | 3.54 | 4.12 | 4.52 | 4.94 | 5.60 | 5.10 | 8.02 | 12.32 | 30.80 | 98.22 | 57.92 |
| 12 | 4.10 | 3.65 | 4.14 | 4.48 | 4.82 | 5.38 | 4.80 | 6.96 | 8.82 | 13.14 | 31.72 | 113.2 |

** Note: All Values *1x10^5

Table 2: Sensitivity Matrix for
Starboard and Port Wing Matrices of
 $\frac{d\Delta C_p}{d\delta_f}$

Starboard

| Sensor # \ Effector # | 1 | 2 | 3 | 4 | 5 | 6 | 7 | 8 | 9 | 10 | 11 | 12 |
|-----------------------|-------|-------|-------|-------|-------|-------|-------|-------|-------|-------|-------|-------|
| 1 | 49.22 | 26.94 | 13.12 | 8.48 | 6.31 | 4.71 | 1.64 | -0.02 | 2.84 | 0.87 | 1.64 | 0.04 |
| 2 | 27.66 | 55.24 | 32.90 | 17.18 | 10.98 | 7.05 | 3.31 | 2.01 | 4.01 | 1.71 | 2.65 | 1.08 |
| 3 | 17.49 | 31.27 | 60.35 | 38.43 | 19.25 | 11.50 | 5.83 | 3.82 | 4.57 | 3.44 | 3.22 | 1.68 |
| 4 | 12.01 | 17.97 | 35.10 | 68.70 | 37.86 | 19.71 | 9.51 | 5.62 | 6.36 | 4.34 | 3.44 | 2.50 |
| 5 | 8.13 | 10.15 | 17.18 | 33.11 | 46.12 | 32.19 | 10.97 | 8.07 | 7.02 | 4.56 | 3.84 | 2.23 |
| 6 | 3.82 | 5.76 | 10.87 | 20.03 | 32.95 | 52.94 | 14.53 | 8.57 | 4.10 | -1.20 | -1.77 | -5.93 |
| 7 | 6.42 | 1.04 | -5.19 | 11.72 | 15.85 | 32.19 | 28.88 | 27.33 | 19.04 | 13.04 | 10.37 | 8.05 |
| 8 | 5.68 | 3.47 | 5.39 | 9.27 | 11.45 | 17.86 | 25.77 | 38.09 | 30.84 | 19.73 | 13.34 | 9.78 |
| 9 | 5.04 | 4.98 | 5.54 | 8.17 | 11.51 | 14.30 | 16.25 | 33.04 | 56.73 | 41.21 | 25.44 | 16.01 |
| 10 | 4.39 | 4.96 | 5.51 | 6.96 | 10.11 | 12.06 | 12.00 | 22.79 | 40.21 | 56.26 | 44.13 | 26.59 |
| 11 | 4.71 | 4.84 | 4.86 | 6.54 | 9.17 | 10.38 | 9.72 | 14.57 | 23.45 | 31.88 | 50.42 | 39.61 |
| 12 | 3.88 | 4.43 | 4.68 | 5.68 | 7.86 | 8.31 | 8.14 | 11.14 | 18.49 | 22.59 | 36.12 | 59.42 |

Port

| Sensor # \ Effector # | 1 | 2 | 3 | 4 | 5 | 6 | 7 | 8 | 9 | 10 | 11 | 12 |
|-----------------------|-------|-------|-------|-------|-------|-------|-------|-------|-------|-------|-------|-------|
| 1 | 55.21 | 34.25 | 21.63 | 15.04 | 6.08 | -4.53 | 3.66 | 4.08 | 3.64 | 2.49 | -1.68 | 2.75 |
| 2 | 36.31 | 59.25 | 39.92 | 23.85 | 13.32 | 1.28 | 6.77 | 7.17 | 4.39 | 4.56 | 0.65 | 5.05 |
| 3 | 23.15 | 38.07 | 63.78 | 40.97 | 22.90 | 9.27 | 10.24 | 11.76 | 6.78 | 6.89 | -1.53 | 4.83 |
| 4 | 17.13 | 22.30 | 37.05 | 57.57 | 37.02 | 14.23 | 10.97 | 10.87 | 4.39 | 3.31 | -3.49 | 2.03 |
| 5 | 11.22 | 15.73 | 24.36 | 38.55 | 66.44 | 34.73 | 14.54 | 9.00 | 3.09 | -0.15 | -0.06 | -1.53 |
| 6 | 11.22 | 11.59 | 17.08 | 23.87 | 39.58 | 57.17 | 22.94 | 17.86 | 10.15 | 7.52 | 6.44 | 4.68 |
| 7 | 5.20 | 7.37 | 11.03 | 13.38 | 16.37 | 26.37 | 46.44 | 38.96 | 22.02 | 15.85 | 9.80 | 9.33 |
| 8 | 5.21 | 7.43 | 8.18 | 10.81 | 13.77 | 18.08 | 29.31 | 55.01 | 34.77 | 22.88 | 11.26 | 10.97 |
| 9 | 4.63 | 6.21 | 8.76 | 9.43 | 11.16 | 12.23 | 18.54 | 36.38 | 48.79 | 36.64 | 25.30 | 15.17 |
| 10 | 4.77 | 5.67 | 7.45 | 8.34 | 8.50 | 8.94 | 12.82 | 24.23 | 31.14 | 54.29 | 37.73 | 25.60 |
| 11 | 5.51 | 6.83 | 7.73 | 8.36 | 8.69 | 7.28 | 10.55 | 19.51 | 23.81 | 32.57 | 40.19 | 36.71 |
| 12 | 3.57 | 6.24 | 6.50 | 7.44 | 8.23 | 6.71 | 9.89 | 17.39 | 17.66 | 22.99 | 29.06 | 55.28 |

** Note: All Values *10^5

Table 3: Calibrations for Effector
Deflections from -15 to 15 degrees

Port Wing

| | -15 | -13 | -11 | -9 | -7 | -5 | -3 | -1 | 0 | 1 | 3 | 5 | 7 | 9 | 11 | 13 | 15 |
|----|-----|-----|-----|-----|-----|-----|-----|-----|-----|-----|-----|-----|-----|-----|-----|-----|-----|
| 1 | 45 | 60 | 71 | 81 | 90 | 98 | 108 | 116 | 119 | 121 | 127 | 131 | 139 | 145 | 153 | 161 | 170 |
| 2 | 49 | 65 | 75 | 83 | 92 | 100 | 108 | 116 | 118 | 121 | 127 | 132 | 139 | 147 | 154 | 163 | 173 |
| 3 | 30 | 62 | 67 | 74 | 81 | 91 | 100 | 109 | 113 | 117 | 127 | 131 | 138 | 145 | 151 | 161 | 170 |
| 4 | 43 | 62 | 71 | 81 | 89 | 100 | 108 | 118 | 121 | 127 | 137 | 141 | 147 | 157 | 161 | 167 | 177 |
| 5 | 55 | 64 | 74 | 86 | 94 | 104 | 111 | 120 | 123 | 126 | 134 | 141 | 146 | 156 | 162 | 164 | 174 |
| 6 | 57 | 69 | 79 | 89 | 97 | 108 | 116 | 122 | 124 | 131 | 141 | 145 | 150 | 162 | 168 | 171 | 177 |
| 7 | 206 | 195 | 179 | 169 | 158 | 150 | 143 | 136 | 133 | 128 | 119 | 115 | 105 | 99 | 92 | 85 | 75 |
| 8 | 201 | 193 | 183 | 173 | 161 | 153 | 145 | 136 | 130 | 127 | 120 | 110 | 103 | 97 | 86 | 77 | 69 |
| 9 | 206 | 194 | 183 | 174 | 163 | 153 | 145 | 138 | 133 | 129 | 120 | 111 | 104 | 97 | 88 | 80 | 69 |
| 10 | 204 | 189 | 178 | 170 | 158 | 151 | 142 | 133 | 129 | 125 | 118 | 110 | 104 | 94 | 84 | 76 | 66 |
| 11 | 200 | 172 | 163 | 153 | 143 | 135 | 127 | 121 | 119 | 115 | 117 | 99 | 95 | 87 | 81 | 72 | 61 |
| 12 | 206 | 186 | 175 | 163 | 154 | 144 | 135 | 128 | 125 | 122 | 112 | 107 | 102 | 94 | 86 | 76 | 66 |

Starboard Wing

| | -15 | -13 | -11 | -9 | -7 | -5 | -3 | -1 | 0 | 1 | 3 | 5 | 7 | 9 | 11 | 13 | 15 |
|----|-----|-----|-----|-----|-----|-----|-----|-----|-----|-----|-----|-----|-----|-----|-----|-----|-----|
| 1 | 184 | 181 | 173 | 168 | 158 | 151 | 143 | 136 | 132 | 129 | 122 | 115 | 106 | 98 | 88 | 77 | 63 |
| 2 | 188 | 180 | 170 | 162 | 152 | 144 | 138 | 131 | 126 | 124 | 117 | 111 | 102 | 94 | 86 | 75 | 64 |
| 3 | 189 | 179 | 167 | 159 | 149 | 142 | 134 | 128 | 124 | 122 | 116 | 109 | 102 | 94 | 87 | 78 | 65 |
| 4 | 193 | 181 | 171 | 162 | 151 | 145 | 137 | 131 | 126 | 124 | 119 | 110 | 102 | 93 | 84 | 74 | 61 |
| 5 | 193 | 182 | 171 | 164 | 152 | 147 | 138 | 132 | 127 | 125 | 119 | 111 | 104 | 96 | 88 | 77 | 66 |
| 6 | 189 | 178 | 168 | 160 | 149 | 144 | 136 | 128 | 125 | 121 | 114 | 105 | 97 | 88 | 80 | 69 | 61 |
| 7 | 66 | 81 | 95 | 102 | 115 | 118 | 126 | 133 | 135 | 139 | 143 | 154 | 161 | 170 | 177 | 188 | 204 |
| 8 | 70 | 87 | 99 | 105 | 115 | 118 | 124 | 131 | 132 | 138 | 142 | 152 | 160 | 164 | 173 | 181 | 190 |
| 9 | 63 | 85 | 97 | 104 | 113 | 117 | 121 | 130 | 132 | 136 | 141 | 150 | 158 | 161 | 170 | 177 | 187 |
| 10 | 60 | 84 | 94 | 102 | 110 | 115 | 118 | 127 | 129 | 134 | 138 | 148 | 155 | 158 | 167 | 171 | 179 |
| 11 | 57 | 79 | 92 | 104 | 111 | 117 | 121 | 130 | 132 | 137 | 142 | 151 | 159 | 162 | 172 | 178 | 187 |
| 12 | 54 | 75 | 86 | 99 | 108 | 118 | 123 | 133 | 137 | 142 | 149 | 160 | 168 | 171 | 178 | 184 | 188 |

6. FIGURES



Figure 1: SMA Actuated Smart Wing
Contoured Surface

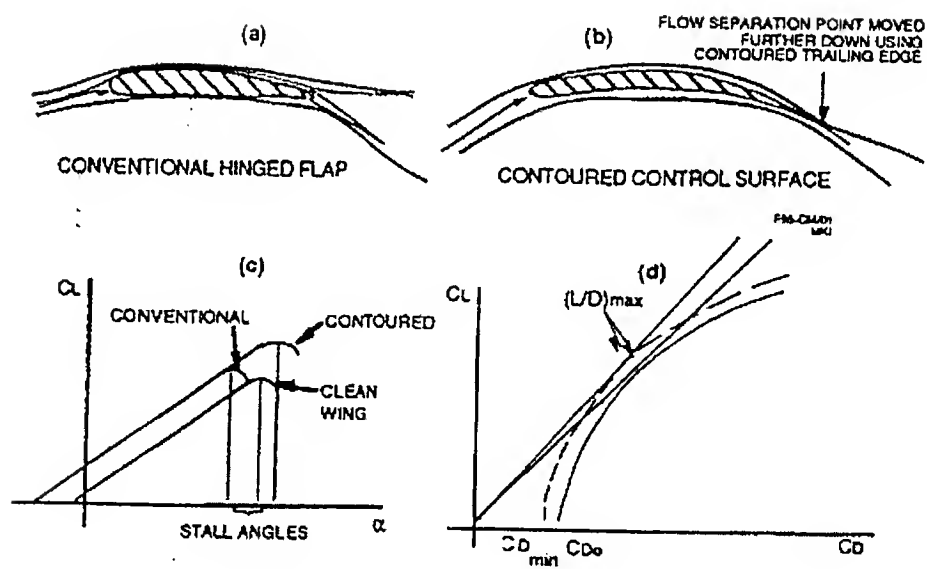


Figure 2: Comparison of Contoured and Conventional Control Surfaces

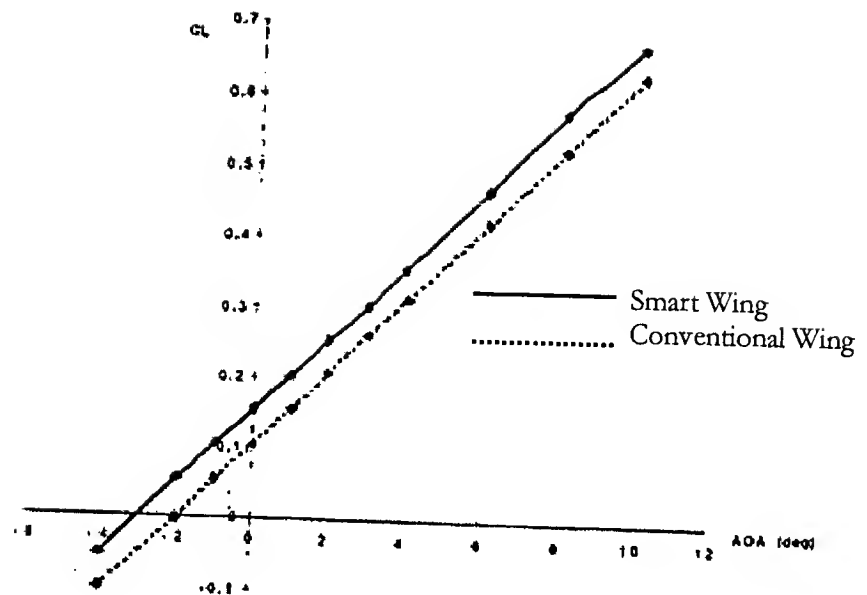


Figure 3: CL vs. AOA Runs for Smart Wing and Conventional Surface

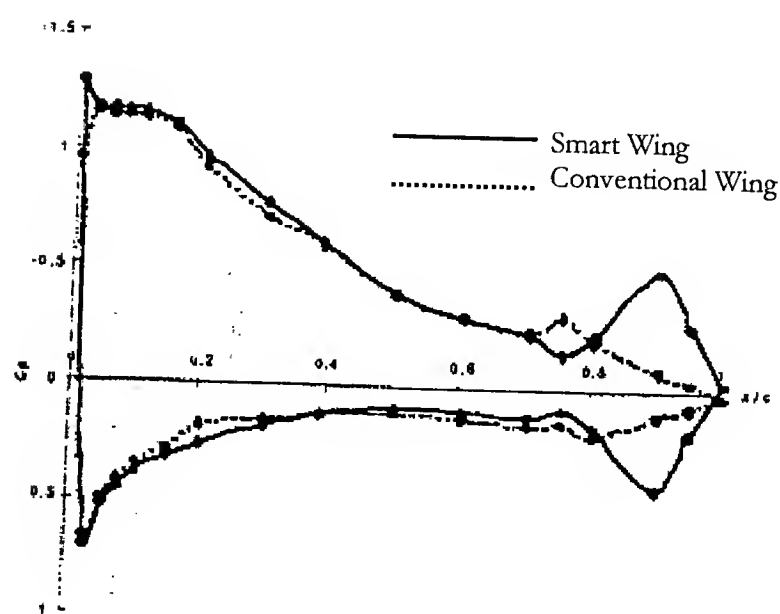


Figure 4: Cp Pressure Distribution for Smart Wing and Conventional Surface

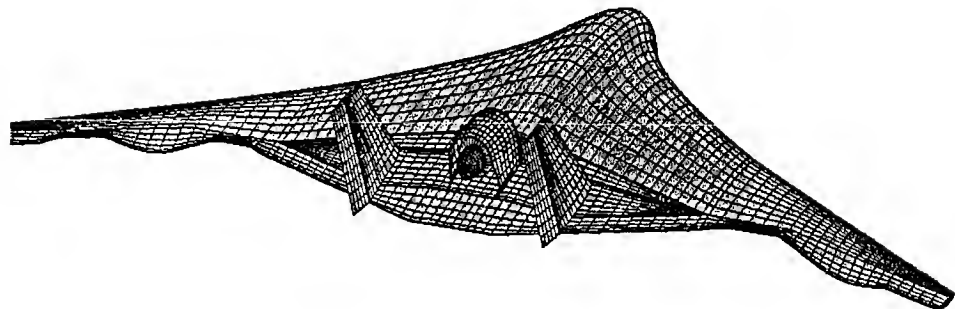


Figure 5: Theoretical Effector Array

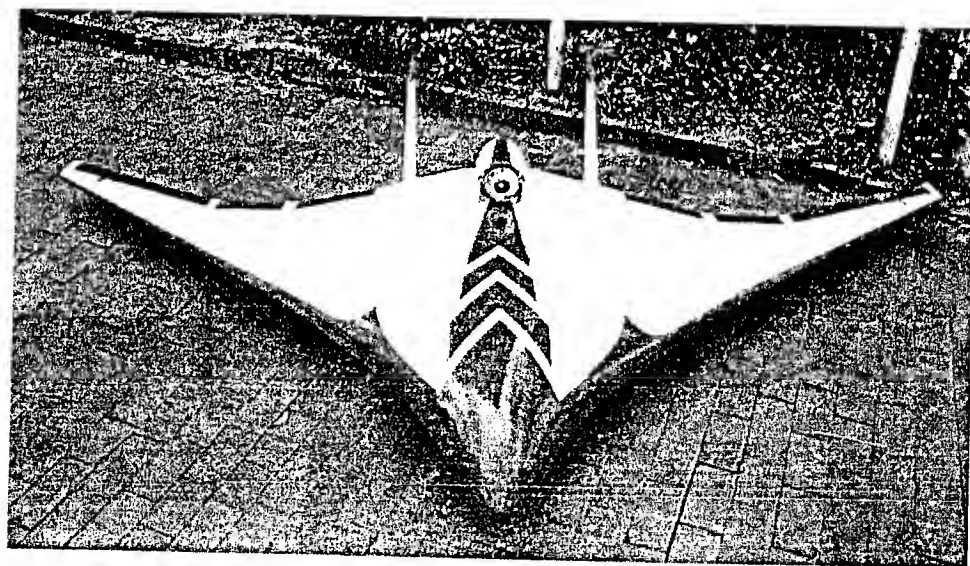


Figure 6: UAV BWB DELTA

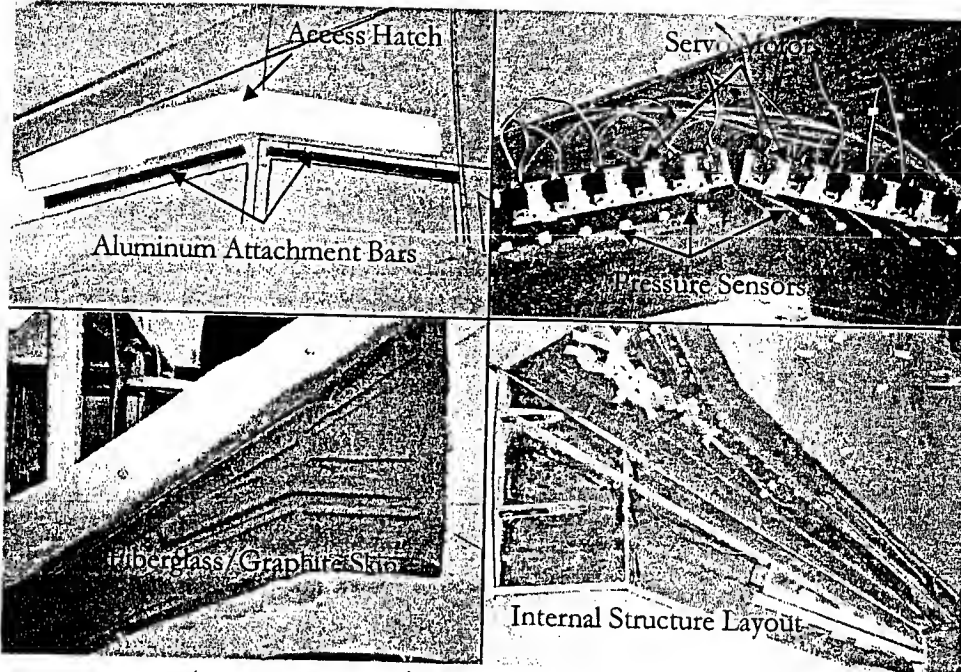


Figure 7: Construction History of
Outboard Wing Panels

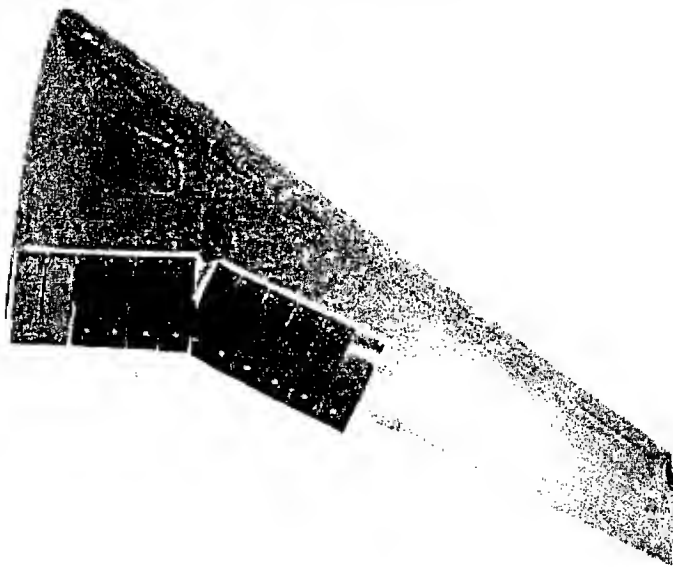


Figure 8: Starboard Wing with
Effectors Attached

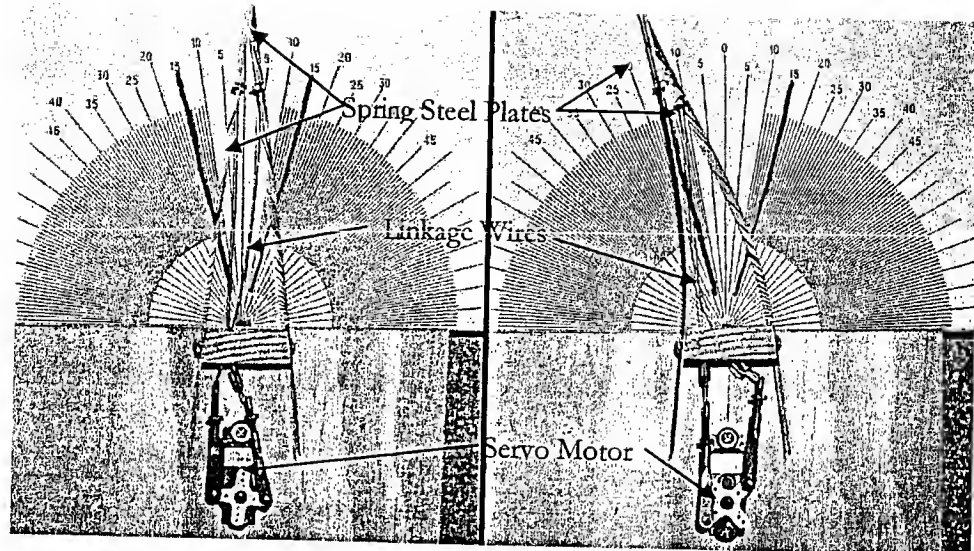


Figure 9: Actuator Design - Deflected (left) and Undeflected (right)

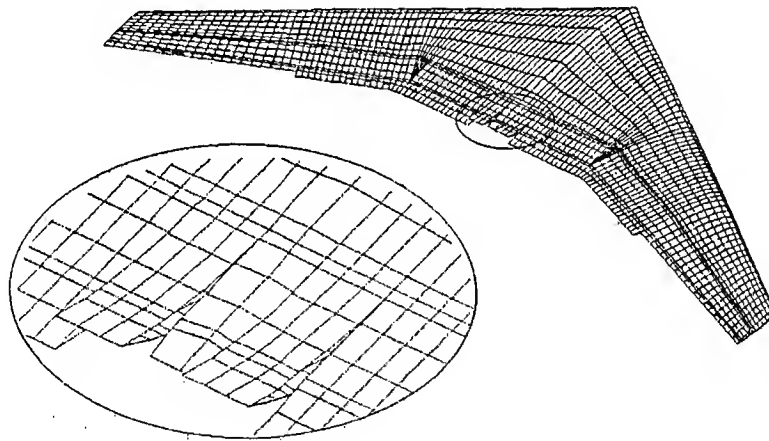


Figure 10: CMARC Model of Outboard Wing Panel with Effector Deflection

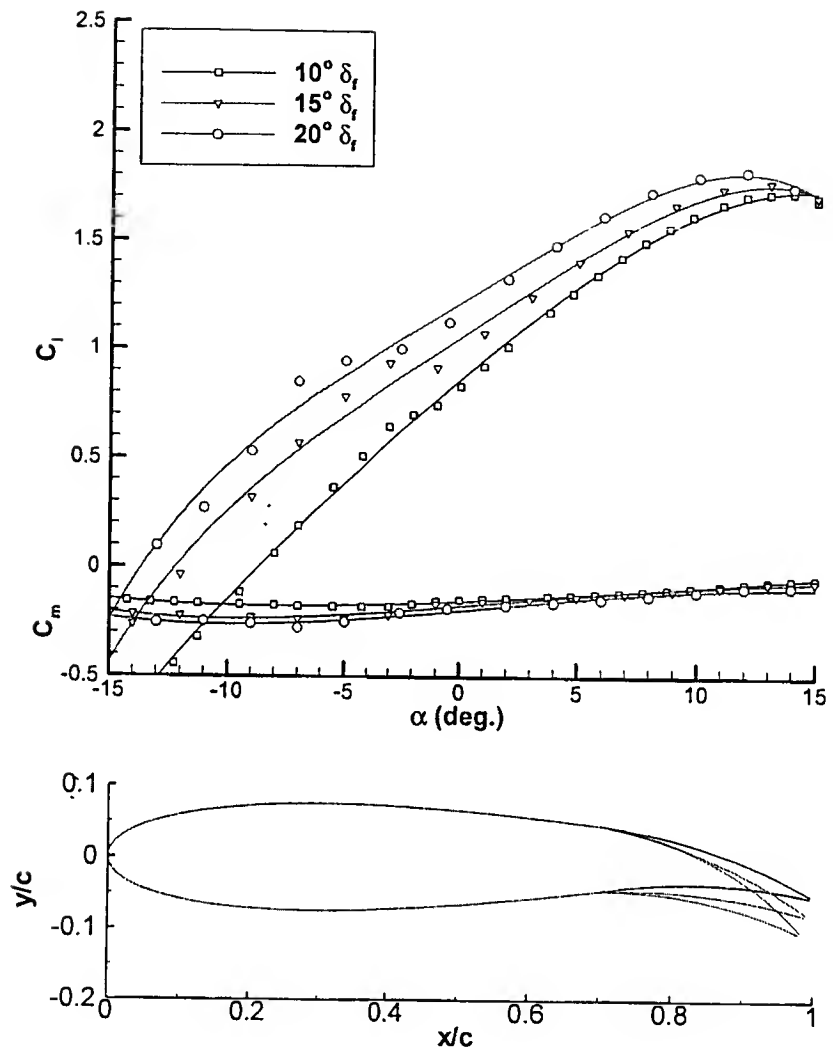


Figure 11: Effect of Flap Deflection
on Aerodynamic Performance

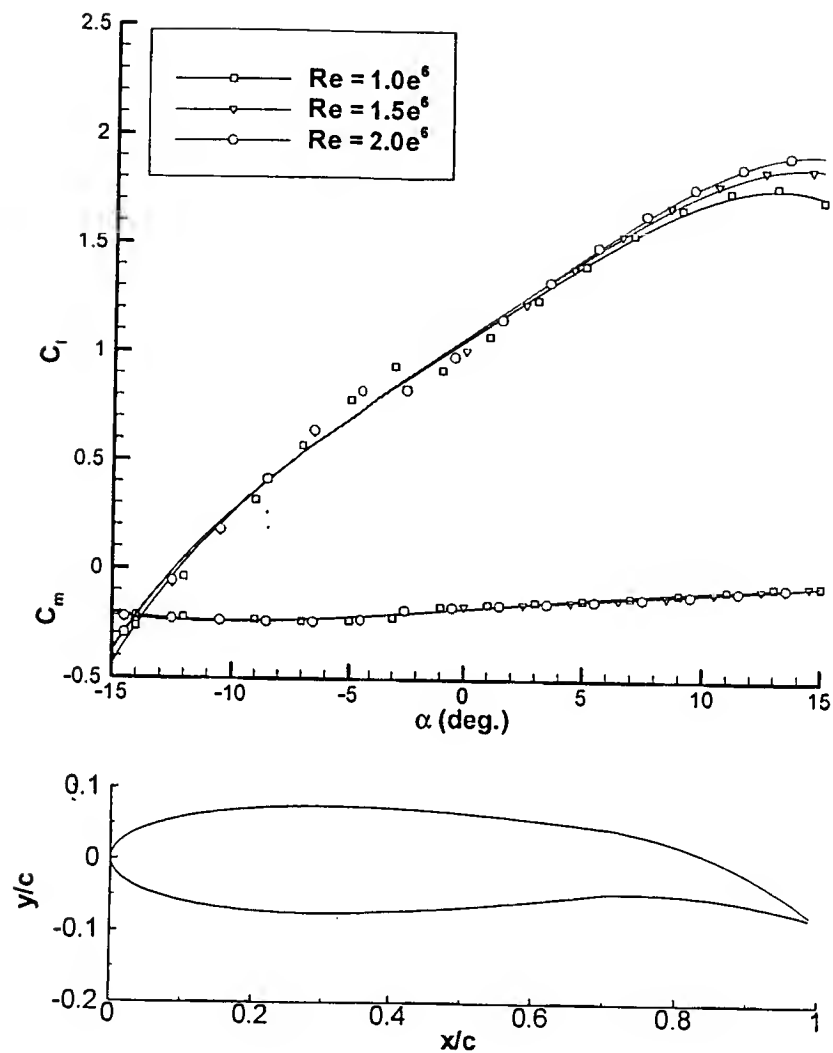


Figure 12: Effect of Reynolds
Numbers on Aerodynamic
Performance

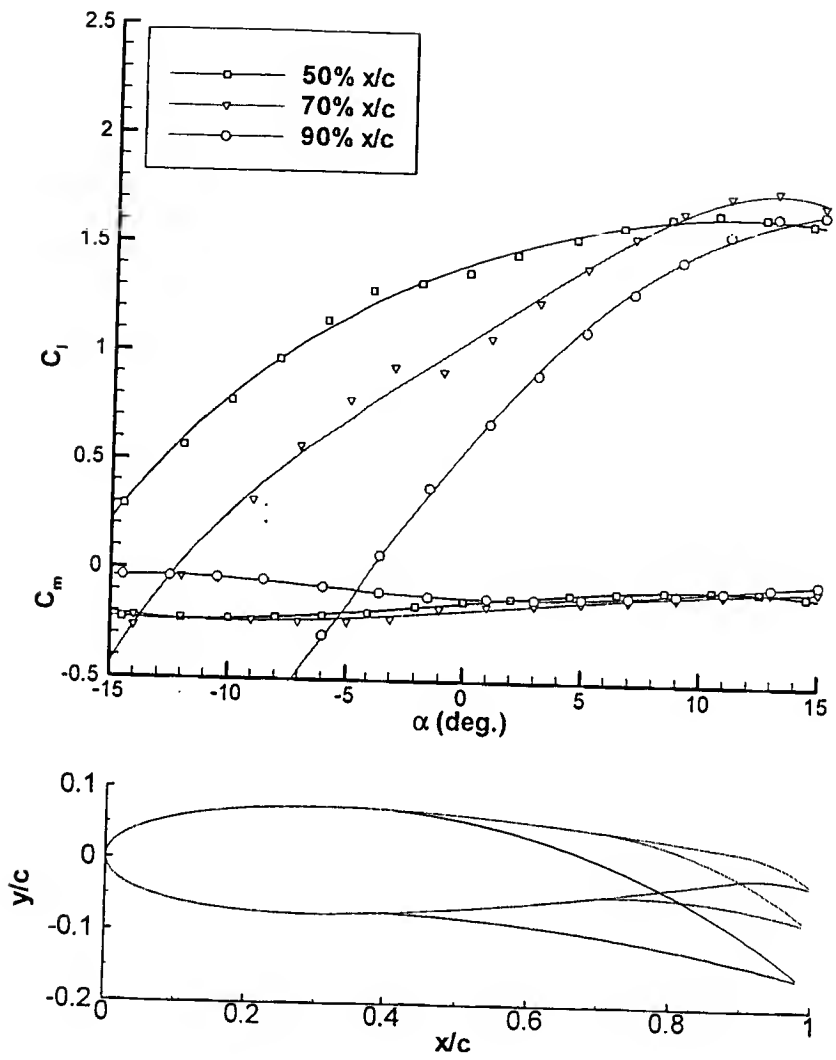


Figure 13: Effect of Hinge Location
on Aerodynamic Performance

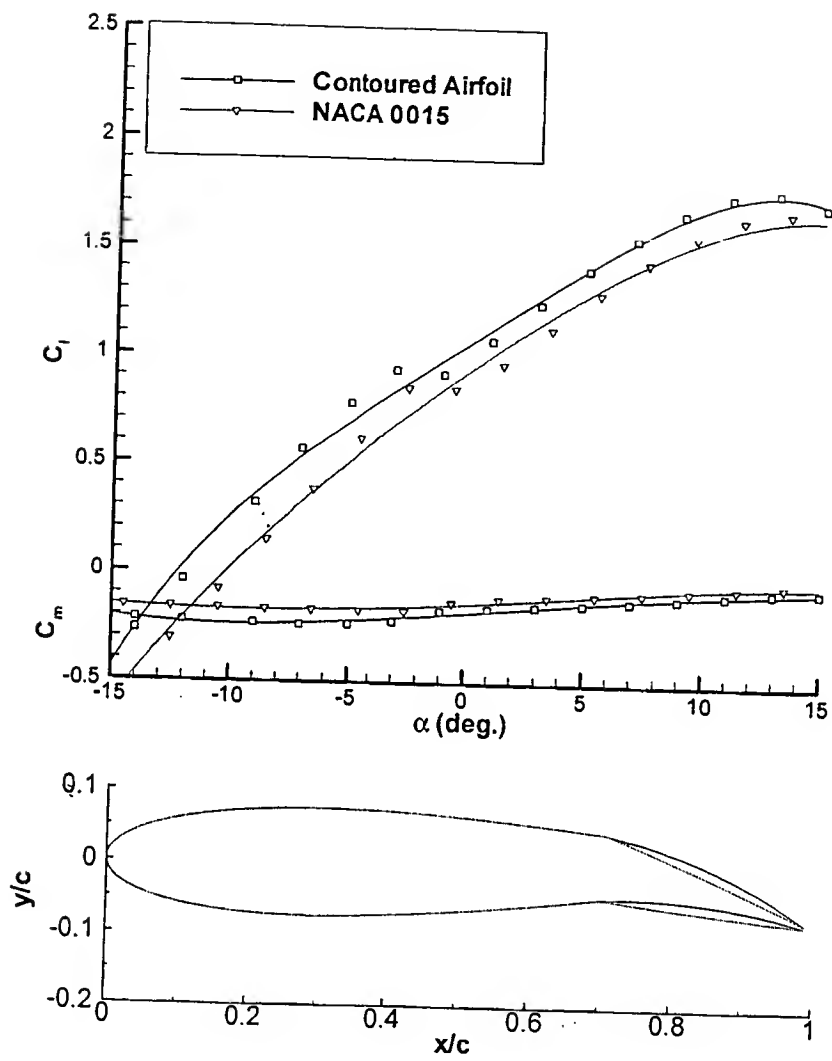


Figure 14: XFOIL Analysis of
Conventional and Contoured Surfaces

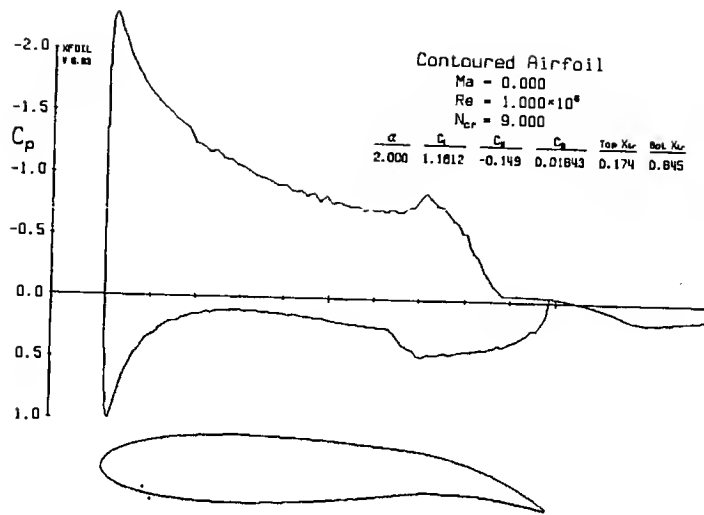


Figure 15: XFOIL Plot of Coefficient of Pressure vs. x/c for Contoured Airfoil

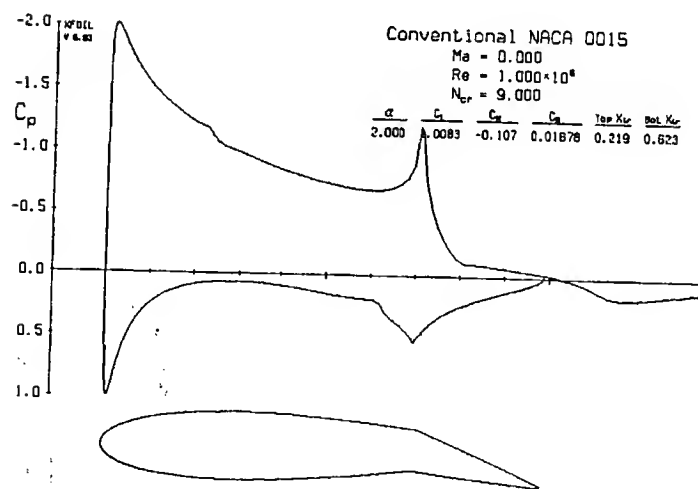


Figure 16: XFOIL Plot of Coefficient of Pressure vs. x/c for Conventional Airfoil

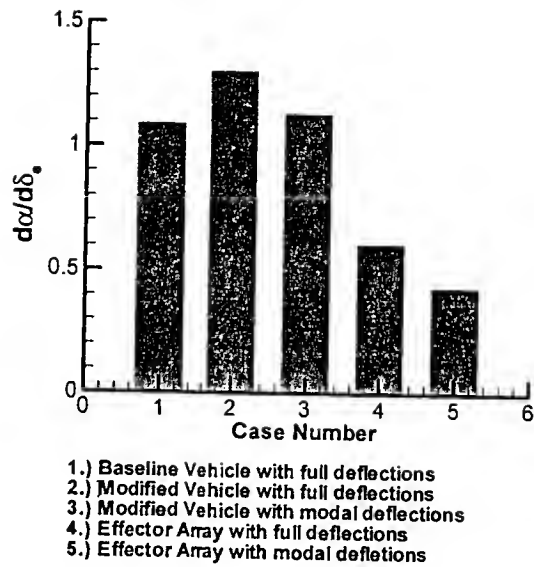


Figure 17: Elevator Control Powers

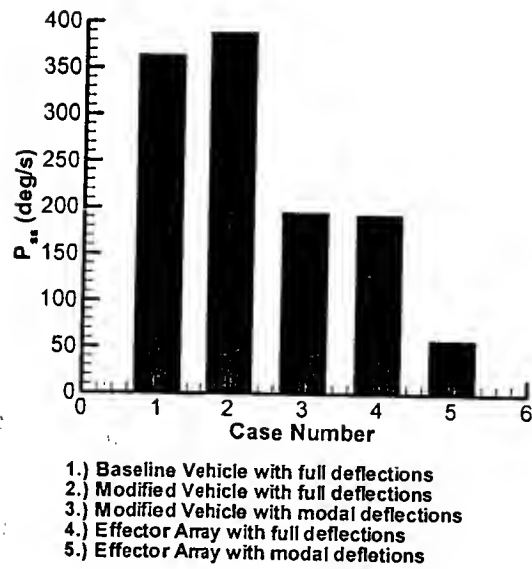


Figure 18: Steady State Roll Rates

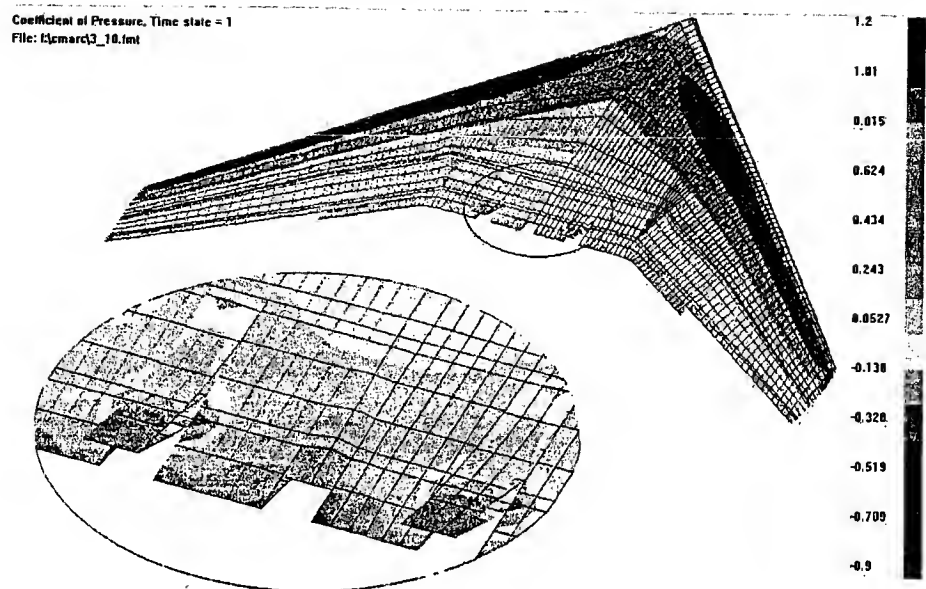


Figure 19: Pressure Distribution from CMARC with an inset of a deflected effector

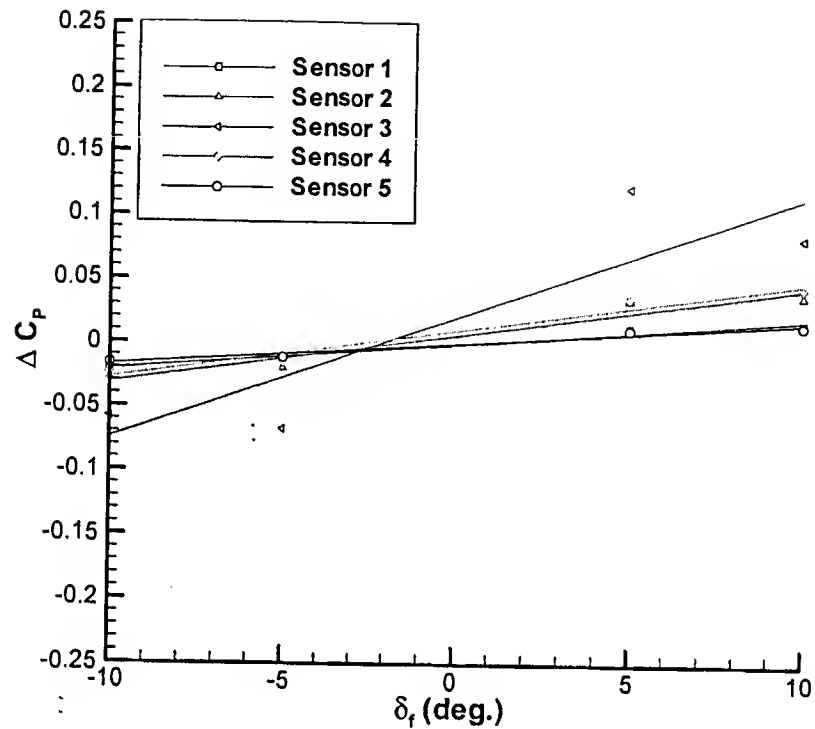


Figure 20: CMARC Pressure Response for Inboard Effector Movement (#3)

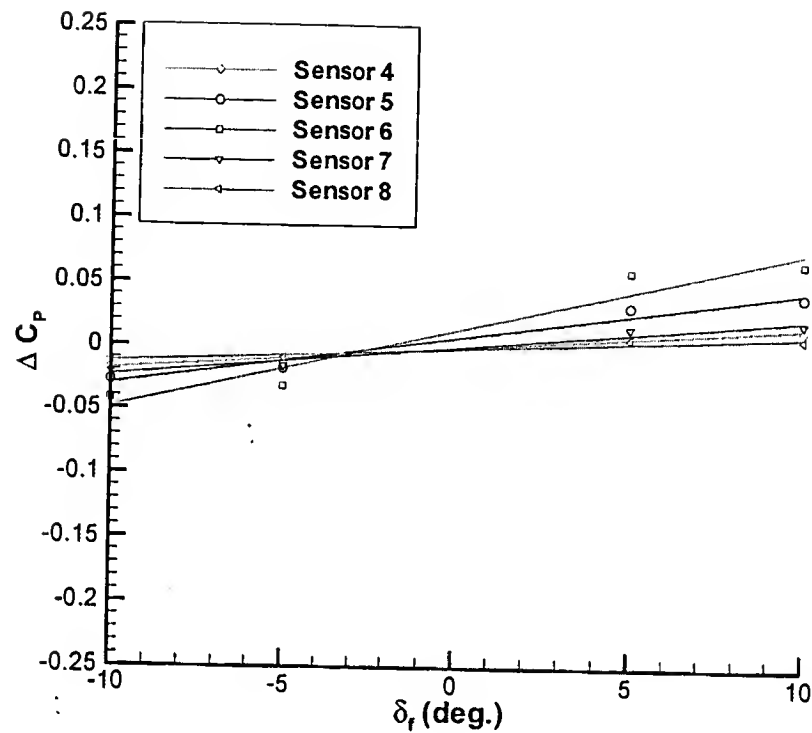


Figure 21: CMARC Pressure
Response for Inboard Effector
Movement (#6)

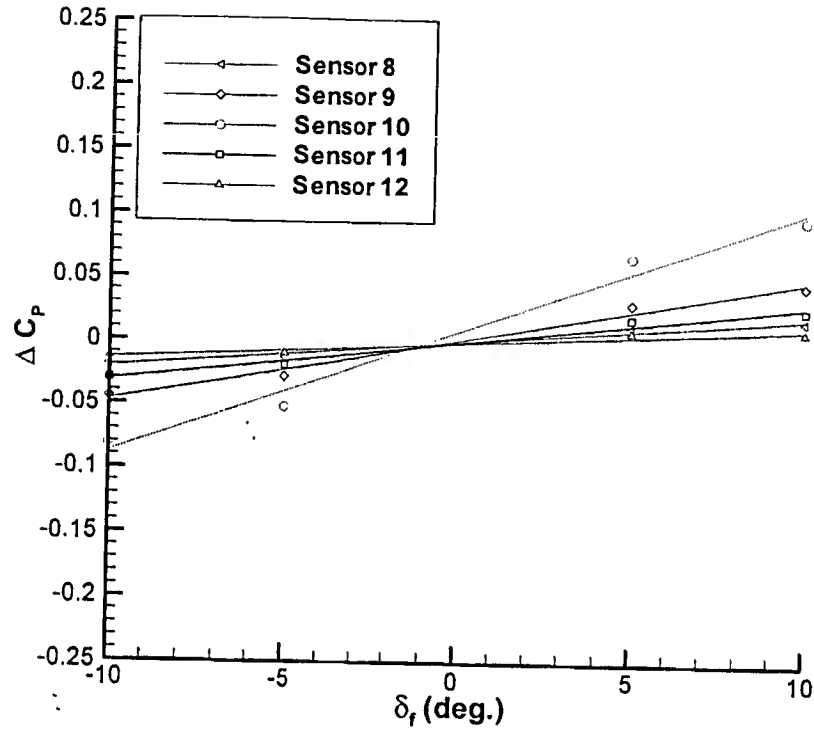


Figure 22: CMARC Pressure Response for Inboard Effector Movement (#10)

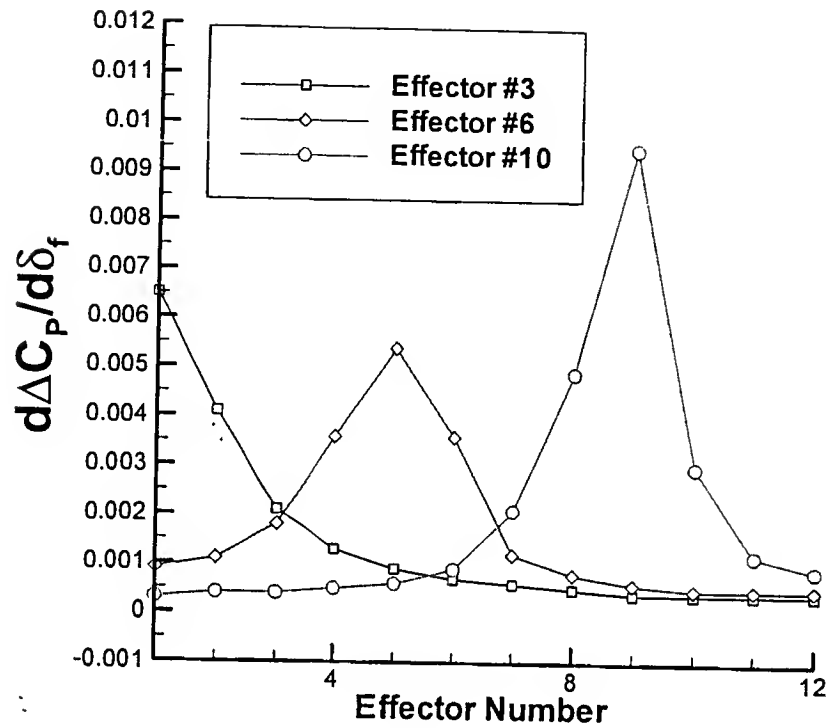


Figure 23: CMARC Sensitivity
Coefficients

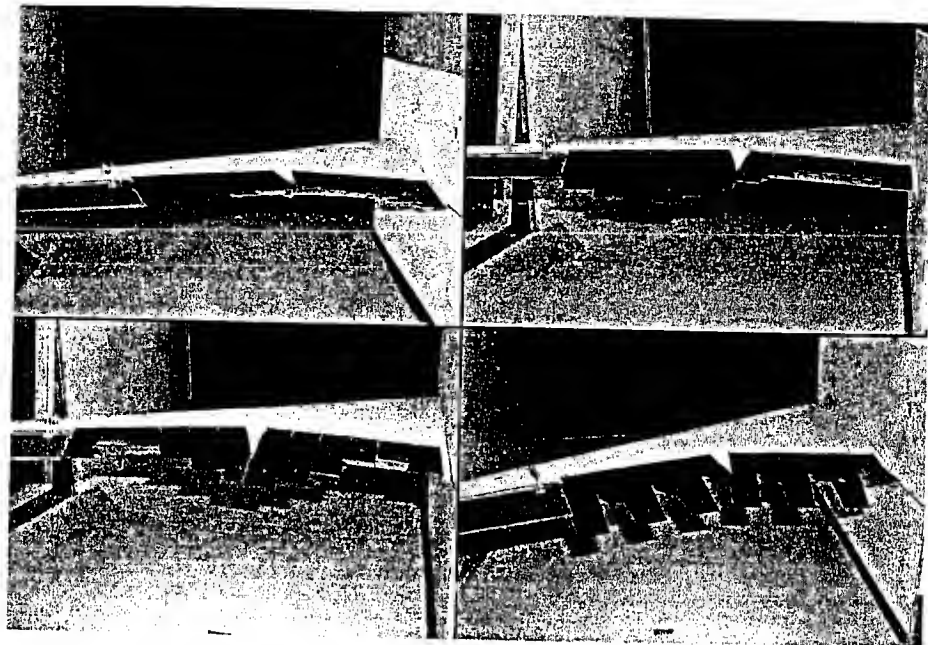


Figure 24: Port Wing in Wind Tunnel
with Various Effector Arrangements

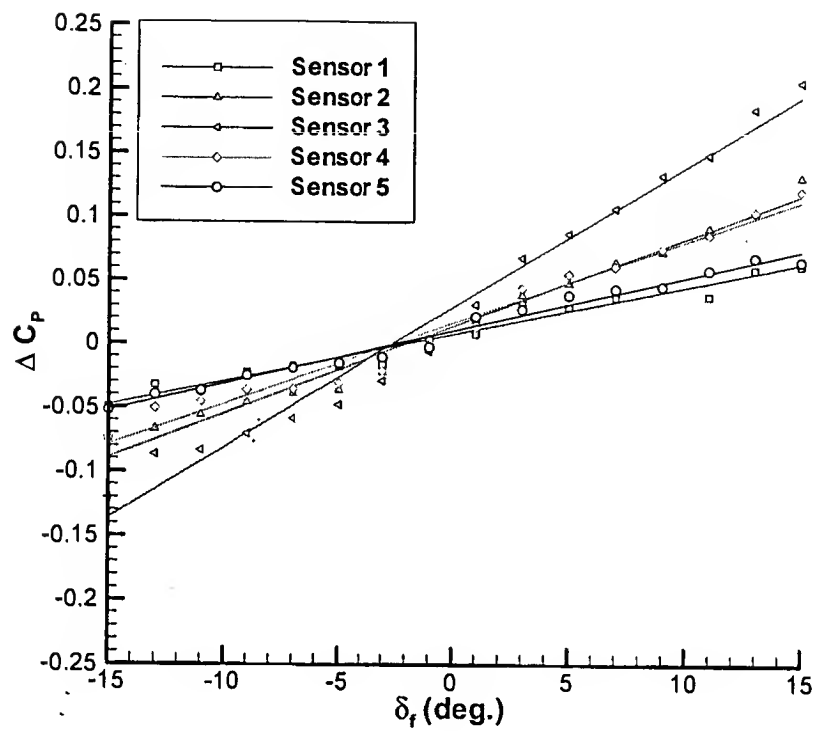


Figure 25: Pressure Response for
Inboard Effector Movement (#3)

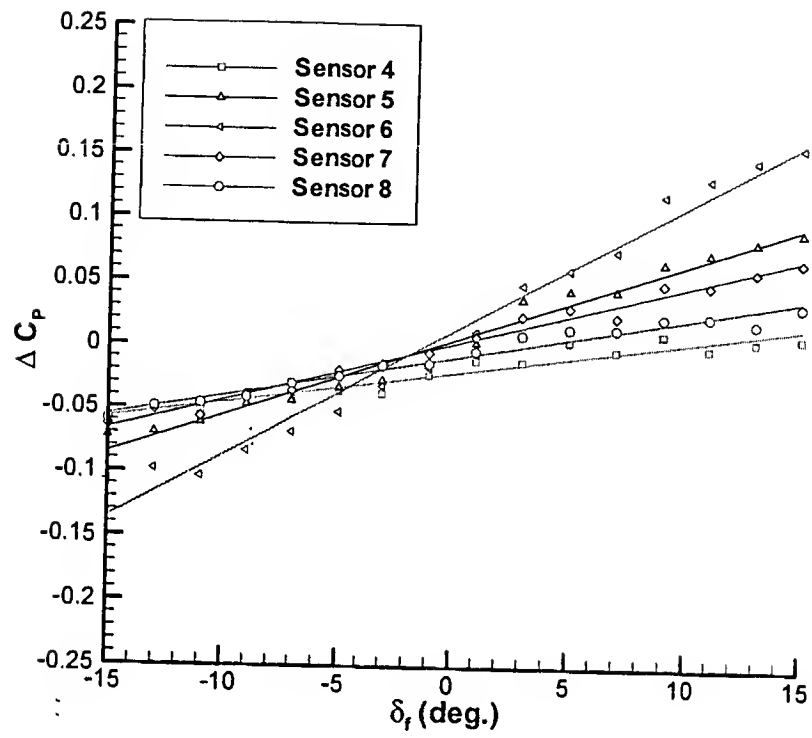


Figure 26: Pressure Response for Mid-Span Effector Movement (#6)

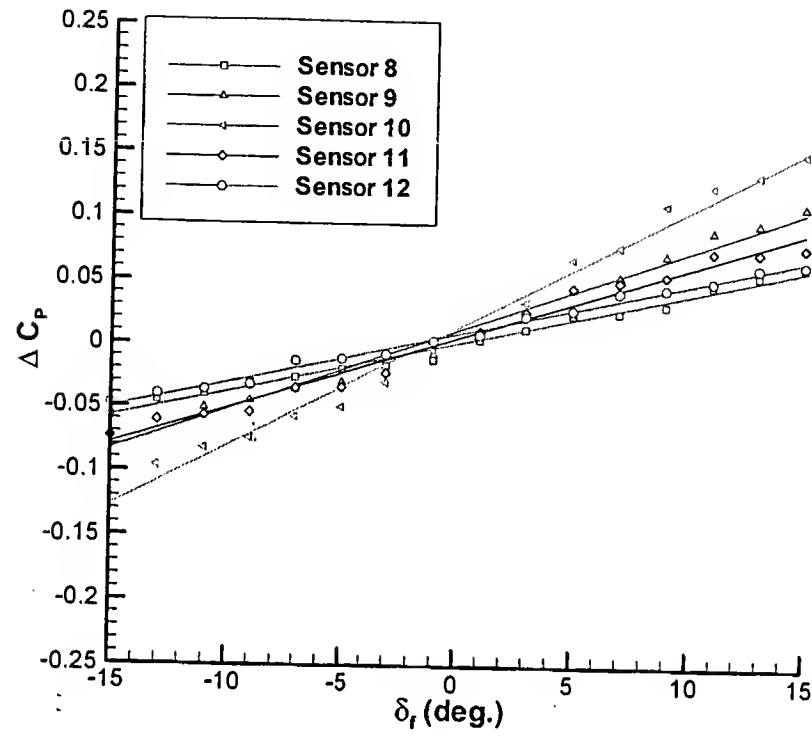


Figure 27: Pressure Response for
Outboard Effector Movement (#10)

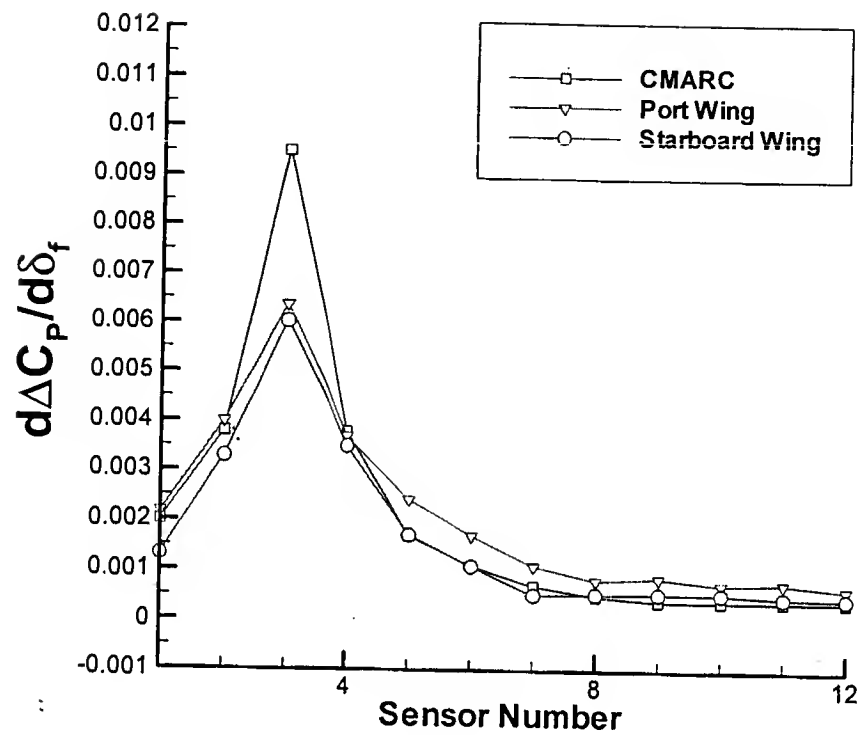


Figure 28: CMARC, Port, and
Starboard Sensitivity Coefficients for
Inboard Effector (#3)

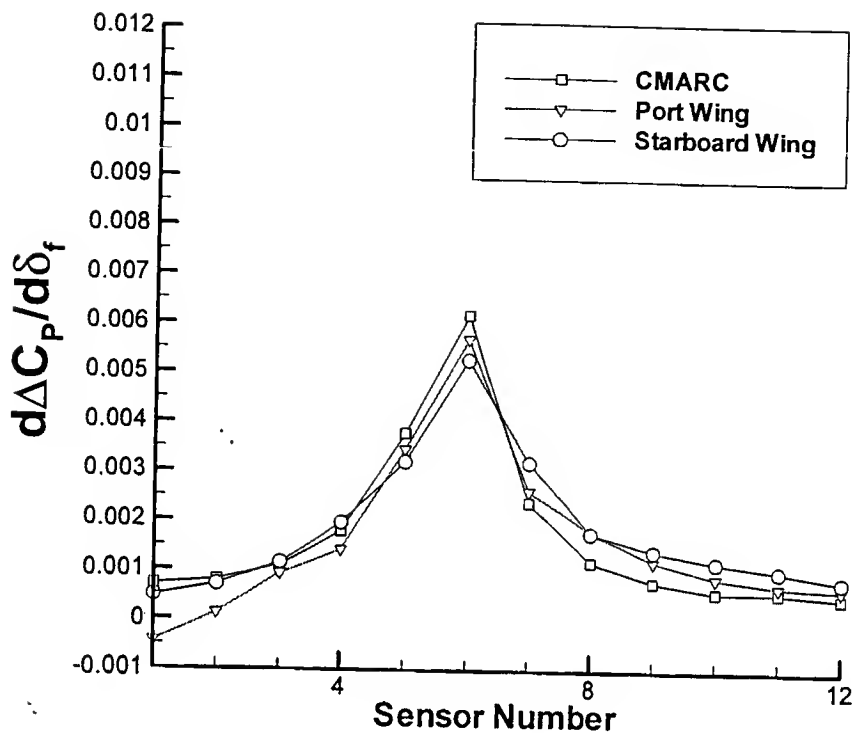


Figure 29: CMARC, Port, and
Starboard Sensitivity Coefficients for
Mid-Span Effector (#6)

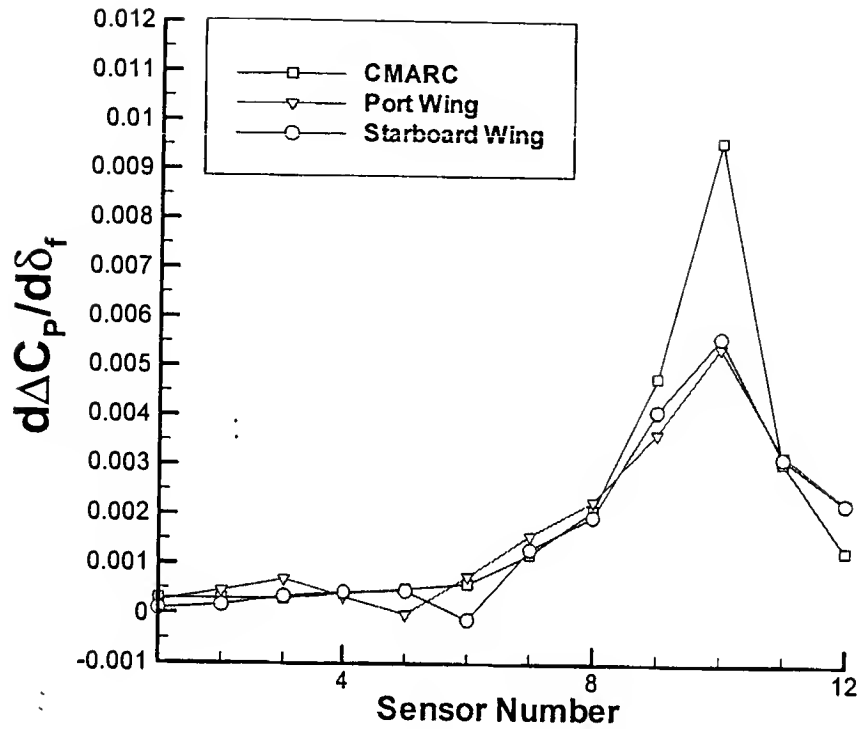


Figure 30: CMARC, Port, and
Starboard Sensitivity Coefficients for
Outboard Effector (#10)

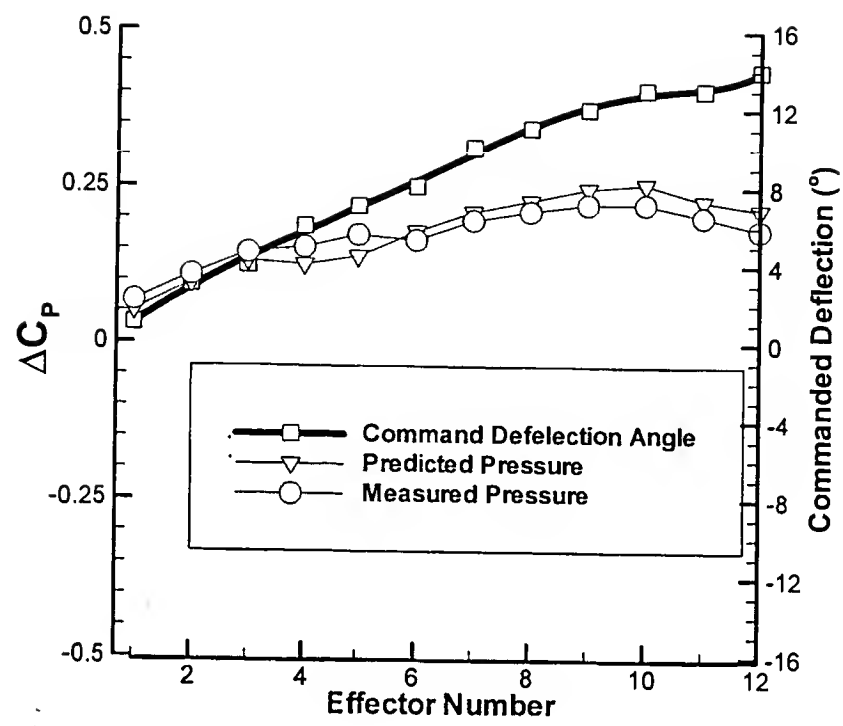


Figure 31: Measured and Predicted Pressure Response for Sine Wave ($A = 15^\circ$, $\omega = 0.1$)

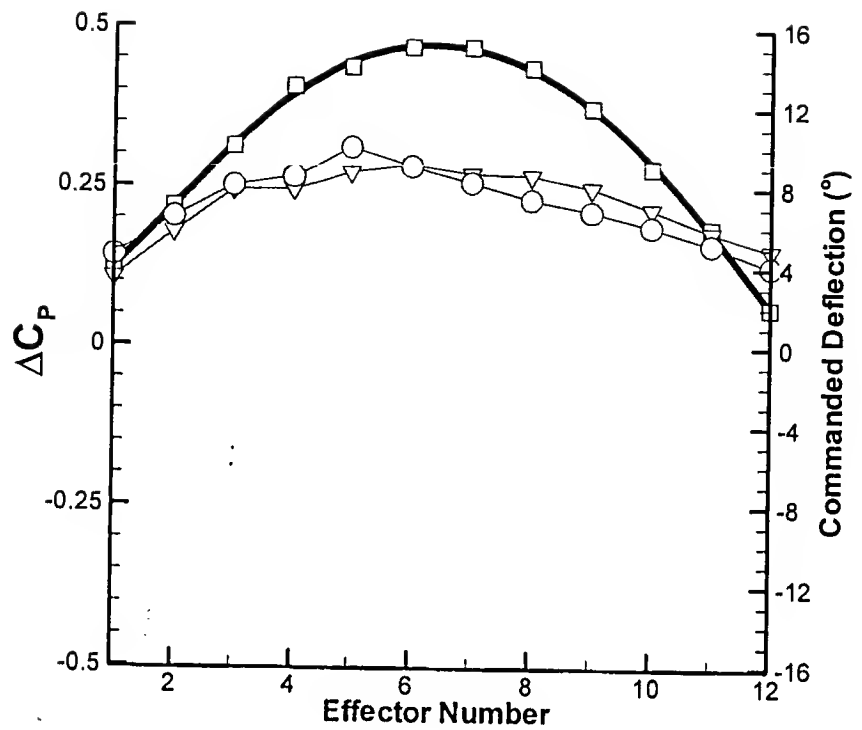


Figure 32: Measured and Predicted Pressure Response for Sine Wave ($A = 15^{\circ}$, $\omega = 0.25$)

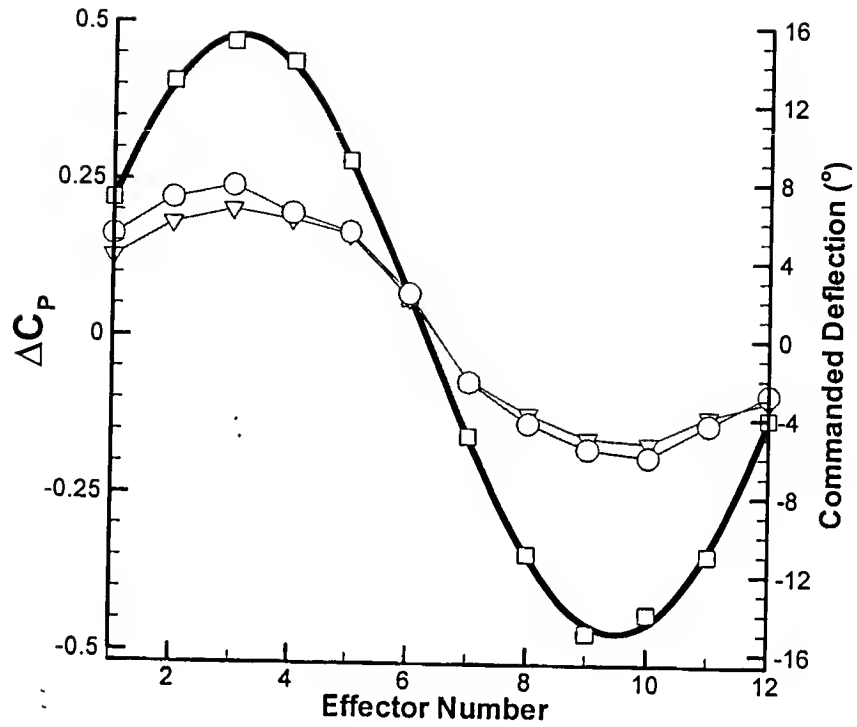


Figure 33: Measured and Predicted Pressure Response for Sine Wave ($A = 15^\circ$, $\omega = 0.5$)

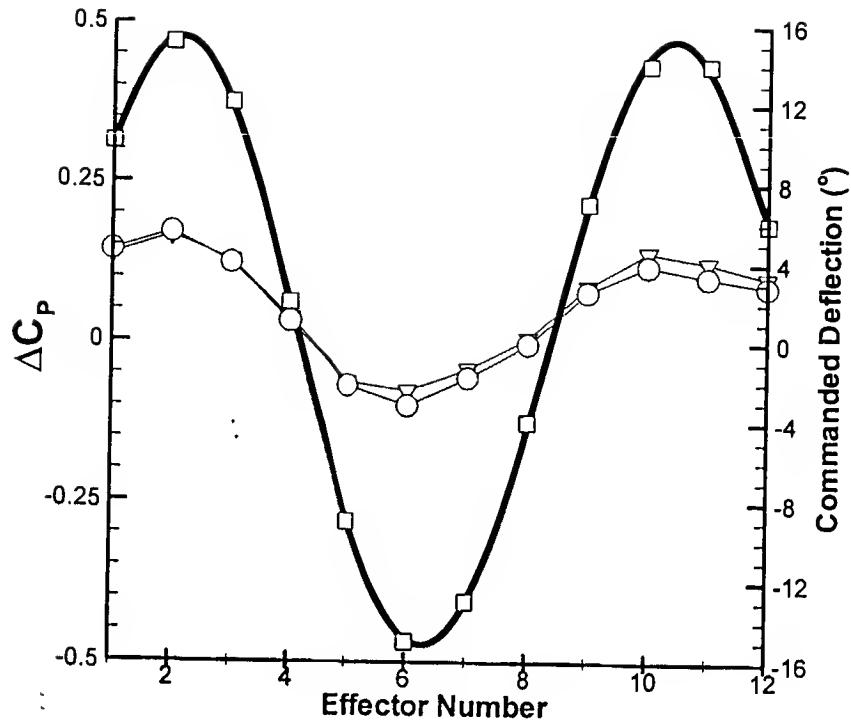


Figure 34: Measured and Predicted Pressure Response for Sine Wave ($A = 15^\circ$, $\omega = 0.75$)

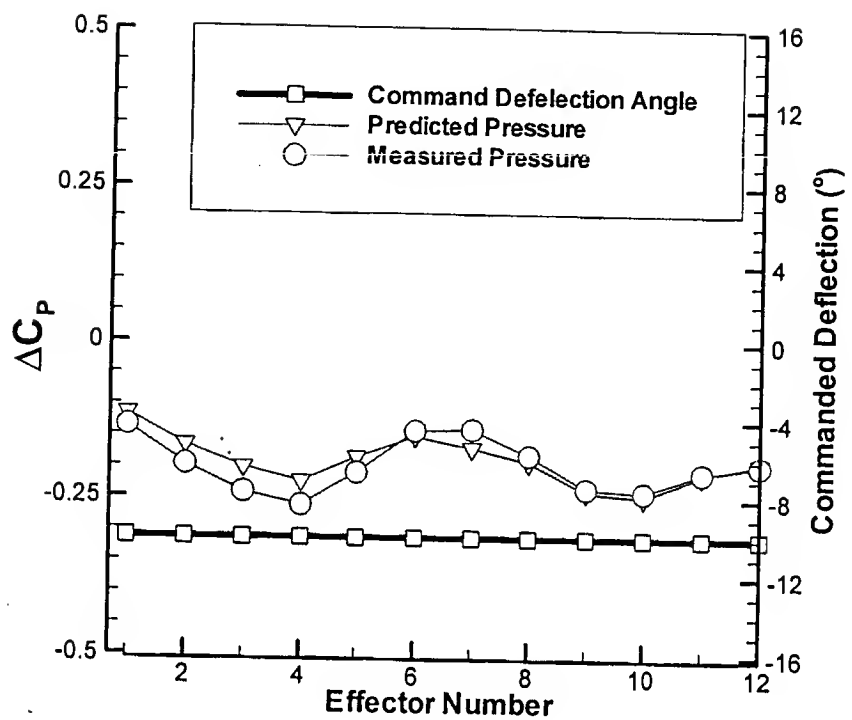


Figure 35: Measured and Predicted Pressure Response for Constant Deflection ($A = -10^{\circ}$)

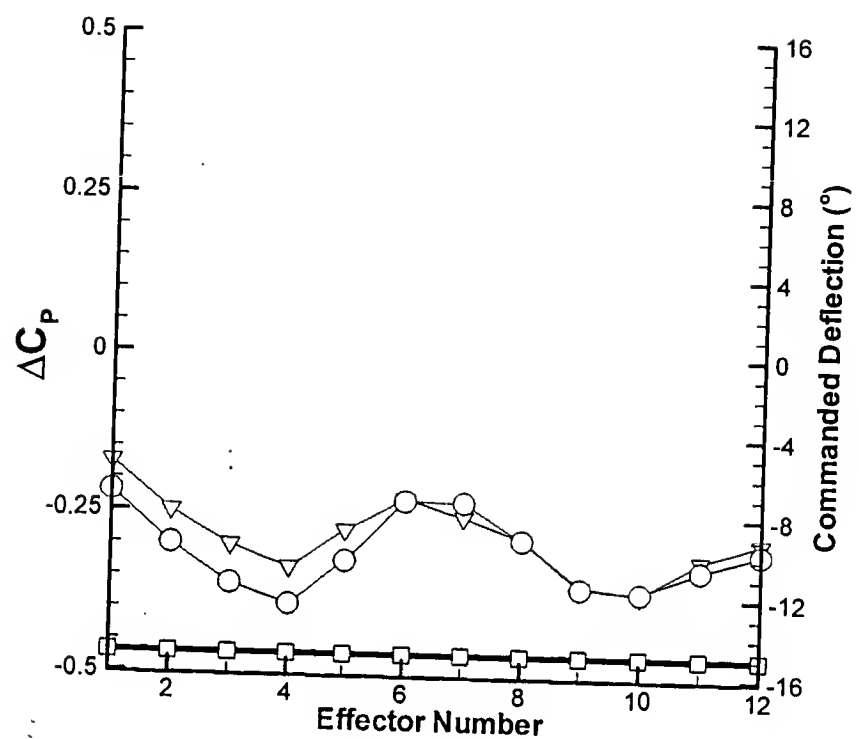


Figure 36: Measured and Predicted Pressure Response for Constant Deflection ($A = -15^{\circ}$)

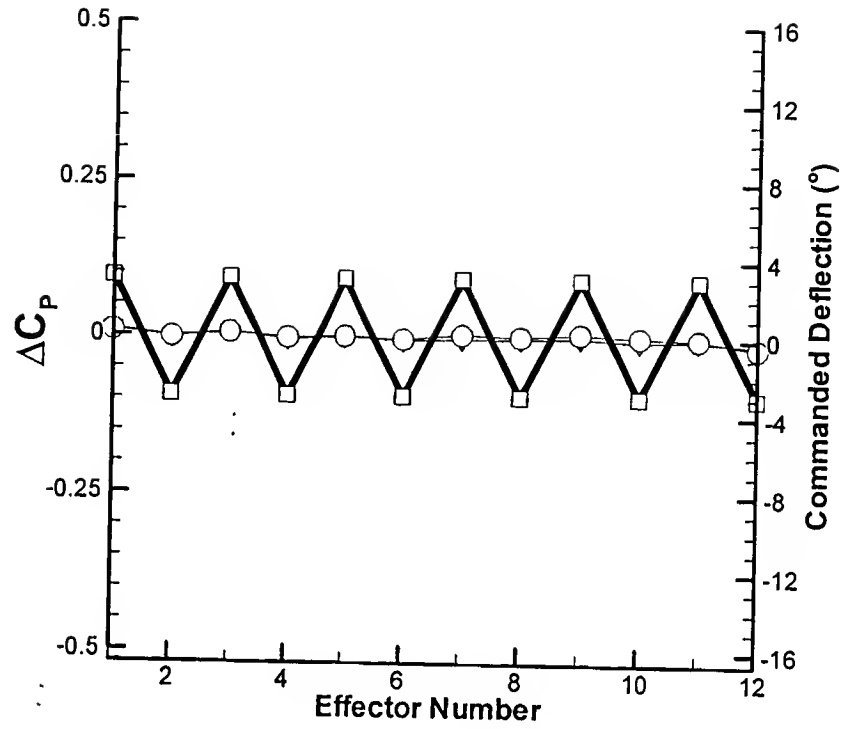


Figure 37: Measured and Predicted Pressure Response for One-Up-One-Down Deflection ($A = 4^{\circ}$)

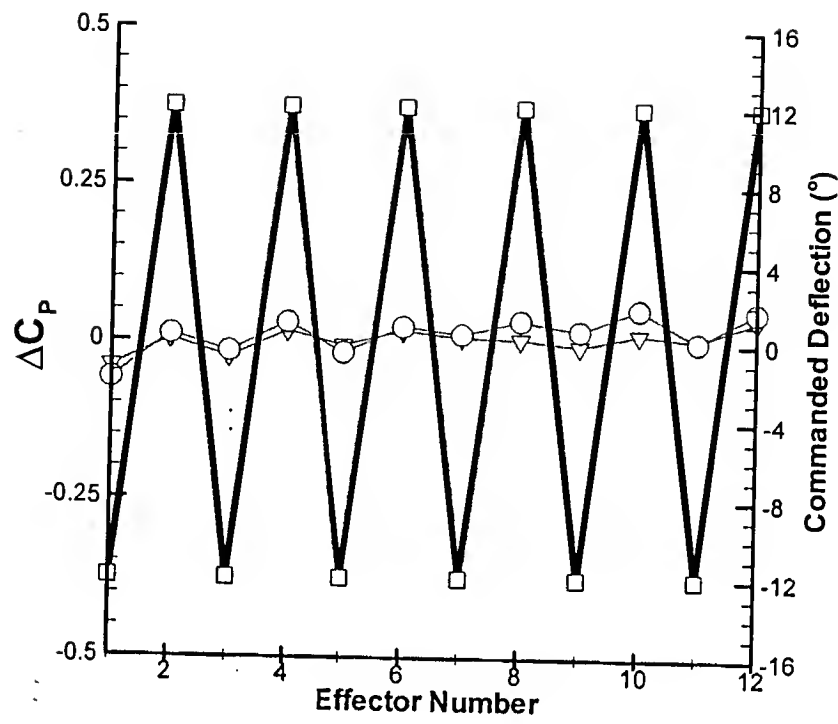


Figure 38: Measured and Predicted Pressure Response for One-Up-One-Down Deflection ($A = 12^{\circ}$)

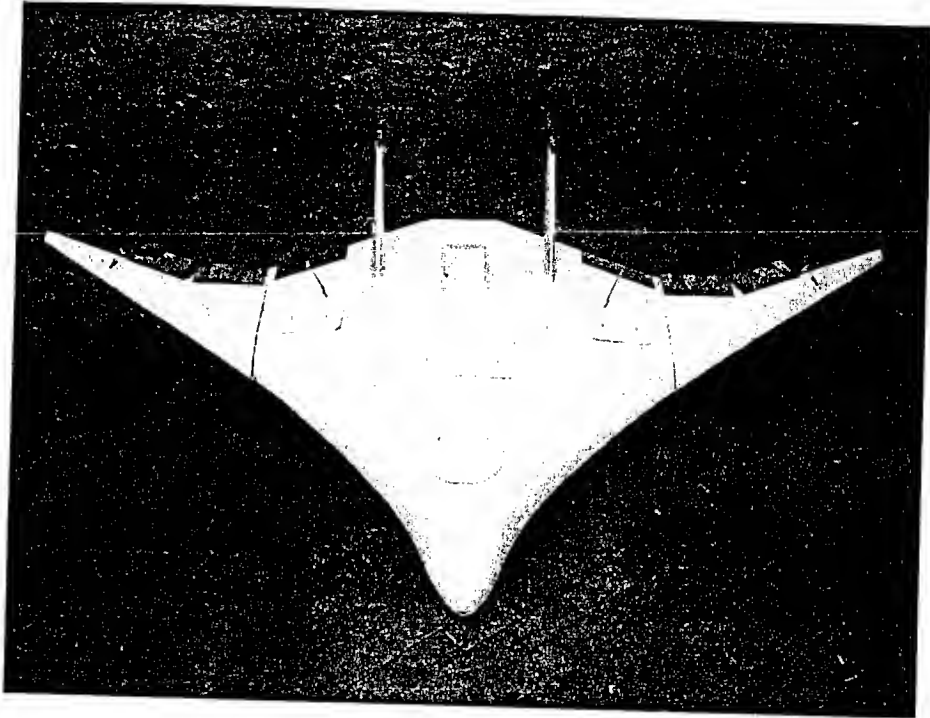


Figure 39: BWB DELTA with
Distributed Effector Wings

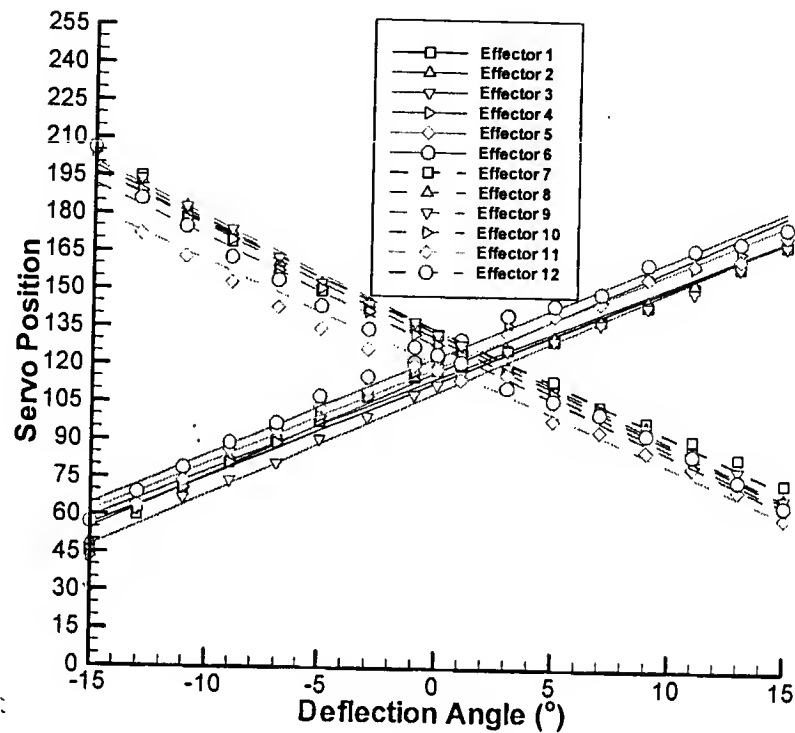


Figure 40: Calibrations for Port Wing

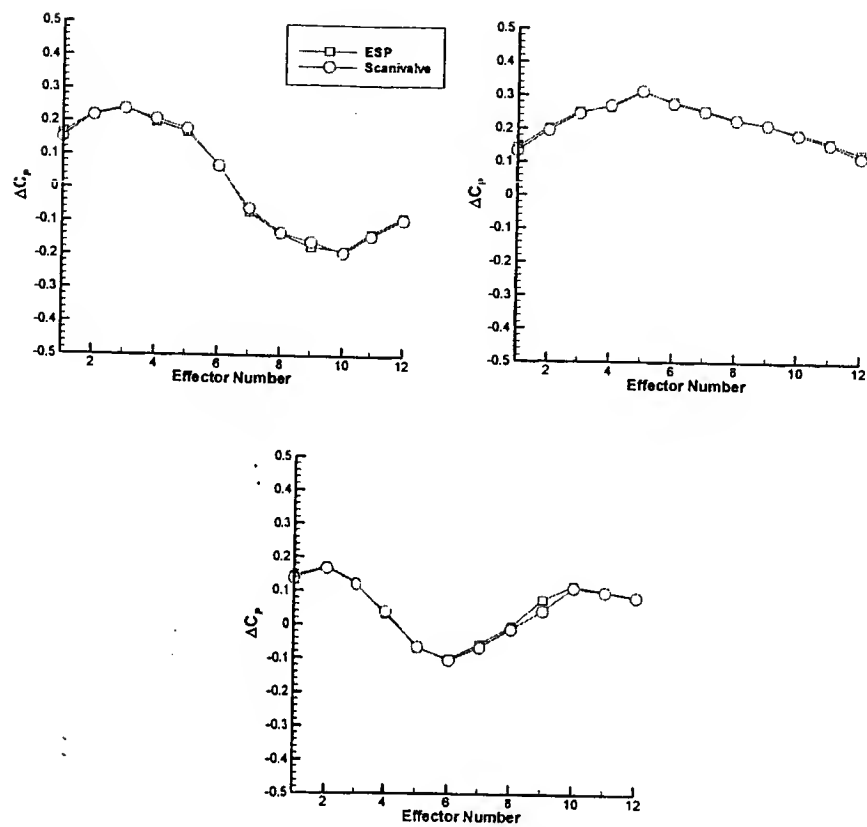


Figure 41: Comparison of ESP vs.
Scanivalve

7. BIBLIOGRAPHY

¹ Wlezien, R. W., Horner, G. C., McGowan, A. R., Padula, S. L., Scott, M. A., Silcox, R. J., Simpson, J. O., "The Aircraft Morphing Program," AIAA Paper 98-1927, April 1998.

² McGowan, A. R., Horta, L. G., Harrison, J. S., Raney, D. L., "Research Activities within NASA's Morphing Program," NATO RTO Meeting - Applied Vehicle Technology Panel, Ottawa, October 1999.

³ Ed. Weatherington, D., "Unmanned Aerial Vehicles Roadmap," Office of the Secretary of Defense, December 2002.

⁴ Bone, E., Bolkcom, C., "Unmanned Aerial Vehicles: Background and Issues for Congress," *Congressional Research Service Report*, Library of Congress, April 2003.

⁵ Sullivan, M., Clark, J., Lea, M., Keener, K., Masters, T., Chaplain, C., Chin, L., Swierczek, B., Rambus, M., "Matching Resources with Requirements is the Key to Unmanned Combat Air Vehicle Program's Success," U.S. General Accounting Office, June 2003.

⁶ Blakeslee, R. J., Mach, D. M., Desch, M. D., Goldberg, R. A., Farrell, W. M., Houser, J. G., "The ALTUS Cumulus Electrification Study (ACES): A UAV-Based Science Demonstration," 1st Technical Conference and Workshop on Unmanned Aerospace Vehicles, Systems, Technologies, and Operations, AIAA-2002-3405, May 2002.

⁷ Leung, J. G., Higgins, R. G., Dunagan, S. E., Arevesen, J. C., "Remote Command-and-Control of Imaging Payloads Using Commercial Off-the-Shelf Technology," 1st International Geoscience and Remote Sensing Symposium, June 2002.

⁸ Herwitz, S. R., Johnson, L. F., Arvesen, J. C., Leung, J. G., Higgins, R. G., Dunagan, S. E., "Precision Agriculture as a Commercial Application for Solar-Powered Unmanned Aerial Vehicles," 1st AIAA UAV Conference, AIAA Paper No. 2002-3404, May 2002.

⁹ Youngblood, J. W., Talay, T. A., Pegg, R. J., "Design of Long-Endurance Unmanned Airplanes Incorporating Solar and Fuel Cell Propulsion," AIAA/SAE/ASME 20th Joint Propulsion Conference, Paper No. 84-1430, June 1984.

¹⁰ Teets, E. H., Jr., Donohue, C. J., Underwood, K., Bauer, J. E., "Atmospheric Considerations for Uninhabited Aerial Vehicle (UAV) Flight Test Planning, NASA TM-1998-206541.

¹¹ Calise, A. J., Johnson, E. N., Johnson, M. D., Corban, J. E., "Applications of Adaptive Neural-Network Control to Unmanned Aerial Vehicles," AIAA/ICAS International Air and Space Symposium and Exposition: The Next 100 Years, Dayton OH, July 2003.

¹² Beard, R. W., McLain, T. W., Goodrich, M., "Coordinated Target Assignment and Intercept for Unmanned Air Vehicles," Proceedings of the 2002 IEEE International Conference on Robotics and Automation, May 2002.

¹³ Raney, D. L., Montgomery, R. C., Green, L. L., Park, M. A., "Flight Control Using Distributed Shape-Change Effector Arrays," AIAA Paper 2000-1560, April 2000.

¹⁴ Gad-el-Hak, M., "Flow Control: Passive, Active and Reactive Flow Management," Cambridge University Press, Cambridge United Kingdom, 2000.

¹⁵ Fontenrose, P. L.; Hall Jr., C. E., "Development and Flight Testing of Quantitative Feedback Theory Pitch Rate Stability Augmentation System" Journal of Guidance, Control and Dynamics, Vol. 19, September-October 1996, pp. 1109-1115.

¹⁶ Heinzen, S. N., Hall Jr., C. E., Chokani, N., "In-Flight Application of Active Separation Control Using Pulsed Jet Blowing" AIAA Paper 2002-0416, January 2002.

¹⁷ Krozel, J., Peters, M., "Decentralized Control Techniques for Distributed Air/Ground Traffic Separation," NASA TR 99RTO36-03, June 2000.

¹⁸ Stipanovic, D. M., Inalhan, G., Teo, R., Tomlin, C. J., "Decentralized Overlapping Control of a Formation of Unmanned Aerial Vehicles," Proc. Of the 41st IEEE Conference on Decision and Control, December 2002.

¹⁹ Barnieh, B., Paganini, F., Dahleh, M. A., "Distributed Control of Spatially Invariant Systems," IEEE Transactions on Automatic Control, Vol. 47, No.7, July 2002.

²⁰ Kroo, I., "Aerodynamic Concepts for Future Aircraft," AIAA Paper 99-3524, July 1999.

²¹ D'Andrea, R., "A Linear Matrix Inequality Approach to Decentralized Control of Distributed Parameter Systems," Proc. IEEE Conference on Decision and Control, pp. 1056-1071, 1997.

²² Kudva, J. N., Appa, K., Van Way, C. B., Lockyer, A. J., "Adaptive Smart Wing Design for Military Aircraft" Requirements and Payoffs, Paper No. 2716-10, SPIE North American Conference on "Smart Structures and Materials." San Diego, CA, February, 1996.

²³ Kudva, J. N., Appa, K., Martin, C.A., Jardine, A. P., Carpenter, B. F., "Overview of recent progress on the DARPA/USAF Wright Laboratory "Smart Materials and Structures Smart Wing" program" SPIE Vol. 3044, No. 3044-01, March 1997.

²⁴ Scherer, L. B., Martin, C. A., Appa, K., Kudva, J. N., "Smart Wing Wind Tunnel Test Results", Paper No. 3044-05, SPIE Symposium on Smart Materials and Structures, March 4 1997.

²⁵ Hoadley, A., Pederson, E., "Prediction of Airfoil Stall in Icing Conditions Using Wing Surface Pressures," AIAA Paper 2001-0422, January 2001.

²⁶ Liebeck, R. H., Page, M.A. "Evolution of the Revolutionary Blended-Wing-Body", NASA Center for Aerospace Information. 1996

²⁷ "UAV Thunderstruck: Fall Report," NC State University Senior Aircraft Design Class: Fall Report, December 2001.

²⁸ "UAV Thunderstruck: Spring Report" NC State University Senior Aircraft Design Class: Spring Report, May 2002.

²⁹ Drela, M., "XFOIL: An Analysis and Design System for Low Reynolds Number Airfoils," Conference on Low Reynolds Number Airfoil Aerodynamics, University of Notre Dame, June 1989.

³⁰ Ashby, D. L., Dudley, M. R., Iguchi, S. K., Browne, L., Katz, J., "Potential Flow Theory and Operation Guide for the Panel Code PMARC," NASA TM-102851, January 1991.

³¹ Hall, C.E. Private Communication, September 2000.

³² Sloan, A. R., Raney, D. L., Private Communication, August 2002.



AIAA 2004-5114

**Wind Tunnel Test of an RPV with
Shape-Change Control Effector and
Sensor Arrays**

David L. Raney and Randolph H. Cabell
NASA Langley Research Center
Hampton, VA 23681

Adam R. Sloan
Stanford University
Stanford, CA 94305

William G. Barnwell and S. Todd Lion
North Carolina State University
Raleigh, NC 27695

Bret A. Hautamaki
University of Michigan
Ann Arbor, MI 48104

AIAA Guidance, Navigation & Control Conference
16-19 August 2004
Providence, Rhode Island

Wind Tunnel Test of an RPV with Shape-Change Control Effector and Sensor Arrays

David L. Raney* and Randolph H. Cabell†

NASA Langley Research Center
Hampton, VA 23681

Adam R. Sloan‡

Stanford University
Stanford, CA 94305

William G. Barnwell§ and S. Todd Lion§

North Carolina State University
Raleigh, NC 27695

Bret A. Hautamaki§

University of Michigan
Ann Arbor, MI 48104

ABSTRACT

A variety of novel control effector concepts have recently emerged that may enable new approaches to flight control. In particular, the potential exists to shift the composition of the typical aircraft control effector suite from a small number of high authority, specialized devices (rudder, aileron, elevator, flaps), toward larger numbers of smaller, less specialized, distributed device arrays. The concept envisions effector and sensor networks composed of relatively small high-bandwidth devices able to simultaneously perform a variety of control functions using feedback from disparate data sources. To investigate this concept, a remotely piloted flight vehicle has been equipped with an array of 24 trailing edge shape-change effectors and associated pressure measurements. The vehicle, called the Multifunctional Effector and Sensor Array (MESA) testbed, was recently tested in NASA Langley's 12-ft Low Speed wind tunnel to characterize its stability properties, control authorities, and distributed pressure sensitivities for use in a dynamic simulation prior to flight testing. Another objective was to implement and evaluate a scheme for actively controlling the spanwise pressure distribution using the shape-change array. This report describes the MESA testbed, design of the pressure distribution controller, and results of the wind tunnel test.

INTRODUCTION

Recent discoveries in material science and fluidics have been used to create a variety of novel effector devices that may enable new approaches to aerospace vehicle flight control. Potential exists to shift the composition of future aircraft control effector suites from a relatively small number of high authority, specialized devices (rudder, aileron, elevator, flaps), toward increasingly larger numbers of smaller, less specialized, distributed effector and sensor device arrays.¹ Such effector arrays might operate in a decentralized fashion on local data from a distributed pressure sensor or accelerometer network to perform highly distributed tasks such as load alleviation, flutter suppression, separation control, or pressure regulation, while simultaneously performing more centralized stability augmentation and maneuver control tasks using feedback from a conventional inertial measurement unit and air data sensor suite. Future aerospace vehicles might use large networks of sensor and effector devices in this capacity, thereby augmenting or replacing conventional control surfaces.

The presumed benefits of such a shift toward distributed effector systems are speculative and come at some cost, particularly in the form of increased system complexity. In addition to the aforementioned distributed control objectives, potential benefits include reduced fuel consumption, enhanced maneuverability, reconfigurability, health monitoring, failure tolerance and mission adaptability. Whether distributed systems will be able to buy their way onto future flight vehicles is likely to depend upon a great number of mission-specific factors and trade offs. But their development and demonstration at the fundamental research level will expand the design space and present options that may enable new missions and new capabilities, or enhance existing functions.

Although several research efforts at universities, government labs and industry are underway to develop and characterize novel effector devices including synthetic jets, shape-change blisters, and micro flaps, relatively few activities address the incorporation of large groups of such devices into aerospace vehicle flight control systems. This research seeks to develop flight

* Research scientist, Dynamics and Control Branch, Senior Member AIAA.

† Research scientist, Structural Acoustics Branch, Senior Member AIAA.

‡ Graduate Student, Mechanical and Aerospace Engineering Department, Member AIAA.

§ Undergraduate, Mechanical and Aerospace Engineering Department, Member AIAA.

control concepts for aerospace vehicles that incorporate measurements from distributed sensor arrays and issue commands to large numbers of distributed effectors to simultaneously perform multiple control functions. Control algorithms are developed and evaluated using a computer simulation model and wind tunnel testing of a small remotely piloted aircraft.

BACKGROUND

Prior work by Park and Green focused on optimizing the placement of distributed shape-change "bump effector" devices over the surface an advanced aircraft configuration for maneuver control purposes by applying automatic differentiation software to a potential flow analysis model.² They applied these bump devices to Lockheed Martin's Innovative Control Effector (ICE) configuration in a conceptual design. A follow-on investigation by Padula and Rogers examined the use of genetic algorithms for determining placement of the shape-change devices.³ These efforts yielded a suite of surface bump control effectors for the ICE configuration. A related investigation by Raney and Montgomery developed a flight dynamic simulation and control design for the vehicle using this bump effector suite.⁴ The study found that the effector suite offered promise for seamless aircraft flight control in a low-rate maneuver mode that might be useful for stealth purposes, but that the authority of the surface bump devices was not sufficient to replace the conventional effector suite for this vehicle.

An unrelated investigation by Bieniawski, Kroo, and Lee developed a testbed that used distributed micro-trailing edge effectors (MITEs) together with distributed accelerometers in a flutter suppression control system.^{5,6} Wind tunnel tests demonstrated successful flutter suppression using a novel control design that was generated by a "reinforcement learning" policy search technique. The investigation demonstrated the potential benefits of control through the use of a large number of small, mechanically simple, distributed effector devices, and developed a unique approach to control synthesis that was specifically tailored for distributed effector and sensor arrays.

A series of investigations that were funded under the DARPA/AFRL/NASA/Northrop Grumman Smart Wing Program have demonstrated the potential of distributed actuation systems to create gap-less, hinge-less continuous mold line control surfaces for adaptive wing designs.^{7,8} In particular, an investigation by Wang, et al addressed the design of distributed actuation systems to generate continuous shape-change deflections of the trailing edge of an airfoil.⁹ A number of material and actuation system concepts were examined, including shape-memory alloys (SMAs), piezo stacks, and ultrasonic motors. The pros and cons of each system were examined and a final design was generated that

used ten distributed high-bandwidth ultrasonic motors to warp a seamless airfoil trailing edge into a variety of continuous geometries with the potential to produce maneuver control moments. In this case, the distributed shape-change effector system provides the airfoil with greater adaptability and functionality than could be achieved by a single large aileron effector occupying the same area.

The present investigation focuses on the use of a small remotely piloted vehicle as a testbed for the development of flight control algorithms using distributed effector and sensor arrays. The testbed is equipped with a total of 24 trailing edge shape-change effector devices and associated pressure measurements. The flight vehicle, called the Multifunctional Effector and Sensor Array (MESA) testbed, was built by NC State University with support from NASA's Aircraft Morphing Program. The vehicle has been tested in Langley's 12-ft Low Speed Tunnel to characterize its basic stability properties, control authorities, and distributed pressure responses to effector deflections for use in a dynamic simulation model prior to flight testing. An additional objective of the wind tunnel test was to implement and evaluate a scheme for regulating the spanwise pressure distribution on the testbed using the distributed sensor and effector array. The ability of the system to achieve and regulate a range of commanded spanwise pressure distributions in the presence of turbulence, flight condition perturbations, and device failures was examined.

This report describes the MESA remotely piloted vehicle (RPV), the design of the spanwise pressure distribution controller for use with the model's trailing edge effector and sensor array, and the results of both phases of the wind-tunnel test, consisting of open-loop characterization of the flight vehicle and closed-loop evaluation of the pressure distribution control design.

EXPERIMENTAL RPV MODEL

The MESA RPV was created by modifying a flight vehicle that had been originally designed, constructed, and flight-tested by a team of aerospace engineering seniors at NC State University during the 2001-2002 term. The original vehicle, named *Thunderstruck*, was similar in planform and appearance to the NASA-Boeing BWB design, although its two large vertical stabilizers were a notable departure. The configuration is shown in Figure 1, along with a view of the final prototype during its graduation flight. The vehicle used a symmetric NACA 0015 airfoil and had a wingspan of 9.4 feet, root chord of 4.9 feet, and takeoff weight of 39 pounds. The vehicle was designed to cruise at 80 miles per hour with a predicted stall speed of 30 miles per hour. An AMT Mercury Turbojet engine provided 14.82 pounds of available thrust. The aircraft was capable of carrying five pounds of payload.

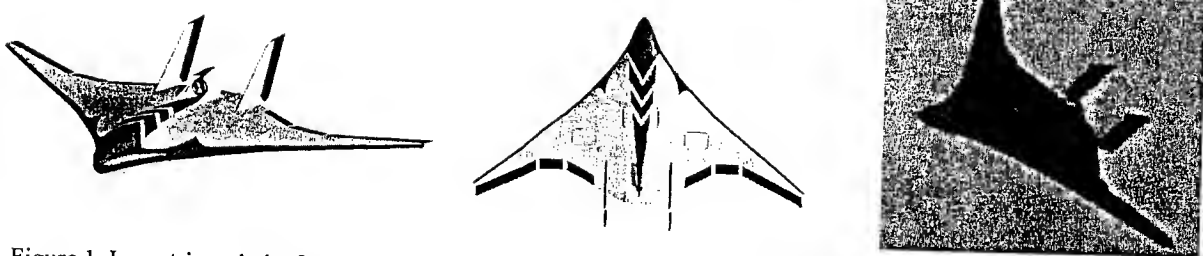


Figure 1. Isometric and planform views of *Thunderstruck*, with a photo of the vehicle during its graduation flight.

For the purposes of this investigation, *Thunderstruck* was transformed into the MESA RPV testbed under a cooperative agreement with NC State. New wings were designed and fabricated, each of which included a distributed array of 12 shape-change trailing edge effector devices and 12 distributed pressure measurements. The design of the shape-change devices composing the trailing edge array required several iterations.

Shape-Change Effector Array

Initially, the hope was to create a completely seamless shape-change trailing edge array such as the one designed in [9], but the weight and complexity of the resulting design was not suitable for this flight vehicle. Instead, it was decided to create a discretized approximation of a continuous mold line fully morphable trailing edge array by dividing the wing trailing edge into twelve small hingeless shape-change control surfaces able to bend in the vertical plane. Each device consists of two thin spring steel skin sections that are split at the trailing edge of the wing. The spring steel plates, having a thickness of 0.007", are warped by a lightweight hobby-class Hobbico CS-5 servomotor through a pull-pull wire linkage; the opposing surface restores the actuated surface to its neutral position. Each effector segment measures 1.5" wide x 4" long, and is capable of deflecting through a range of ± 15 degrees. This design allowed the array to be constructed of lightweight, inexpensive, commonly available and reliable supplies. Figure 2 shows a side view of the prototype effector design in the undeflected and fully deflected positions.¹⁰

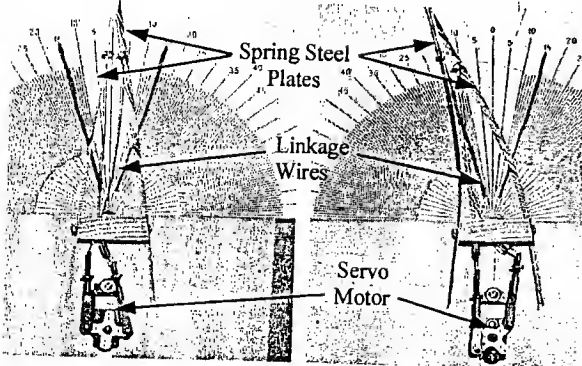


Figure 2. Side view of shape-change effector prototype.

The placement and number of effector devices that were incorporated into the MESA testbed was influenced by several factors. Due to accessibility issues within the existing aircraft fuselage, it was decided that the shape-change array should be confined to the removable wing sections. Wing thickness and chord limited the outboard placement of the devices. Refraining from extending the array into the outboard-most wing area also left space for a conventional aileron that could be used in conjunction with the remaining conventional surfaces to trim and control the testbed during takeoff, landing, and other non-research functions. Potential flow analysis generated linear aerodynamic force and moment estimates that were used in flight dynamic simulation studies to identify an installation region that would provide control authorities comparable to the conventional effector suite. These considerations lead to the final design decision to include twelve devices on each wing. The modified wing panels increased the RPV weight by 3 lb.

The MESA RPV is shown in Figure 3. In addition to the shape-change effector suite, the conventional aileron, elevon and rudder control effectors are apparent in the figure. Shown in Figure 4 is a panel model of the vehicle that was used in the potential flow analysis to generate preliminary estimates of stability and control characteristics for the flight dynamic simulation model. The potential flow results will be compared with wind tunnel measurements later in this report. Table 1 summarizes the flight vehicle characteristics. Further detail regarding design, fabrication, and preliminary testing of the shape-change effector array is provided in [10].

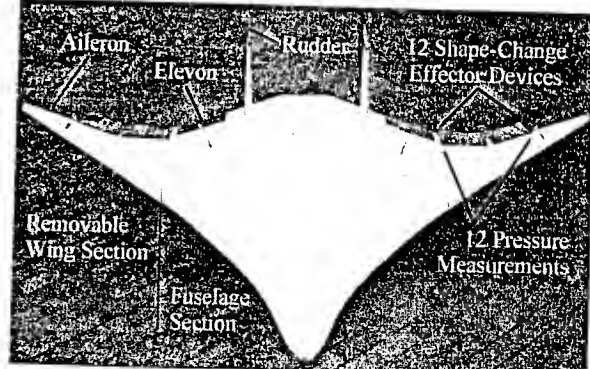


Figure 3. MESA RPV with modified wing panels.

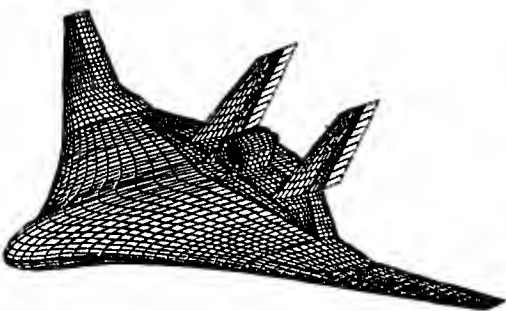


Figure 4. Potential flow panel model used to develop preliminary stability and control estimates.

| Parameter | Value |
|--------------------------------|--------|
| Takeoff Weight, lb | 42 |
| Wing Area, ft ² | 17.77 |
| Span, ft | 9.38 |
| Mean Chord, ft | 2.86 |
| V _{cruise} , ft/s | 117 |
| V _{stall} , ft/s | 44 |
| Inertias, slug ft ³ | |
| I _{xx} | 0.0808 |
| I _{yy} | 1.6362 |
| I _{zz} | 2.3832 |
| I _{xz} | 0.0900 |

Table 1. MESA flight vehicle characteristics

Effector Deployment Modes and Shapes

The effector array could be operated in either open-loop or closed-loop command modes. The open-loop mode allowed commands to be generated using one of three settings. The first setting permitted independent deflections of individual effector segments. The second setting permitted the selection of one of six static trailing edge shapes, in which each effector took part in approximating a portion of the shape. A total of six shapes were implemented consisting of a constant offset of the trailing edge, a linearly sloped offset, half sine wave, whole sine wave, a 1.5-cycle sine wave, and finally an alternating plus/minus deflection. Photos of the left wing of the model with effector segments deployed in trailing edge shapes 1, 2, 3, and 6 are shown in Figure 5. The third open-loop setting permitted the array to be driven dynamically with an arbitrary deflection time history.

The closed-loop command mode drove the effector positions with a real-time hardware-in-the-loop feedback control system designed to achieve a commanded pressure distribution at the spanwise taps. The feedback control algorithm will be presented later in this report.

Distributed Pressure Measurements

Pressure measurement taps were placed upstream of each effector to investigate the potential to control the spanwise pressure distribution with the shape-change array. Locations of the taps were determined using a

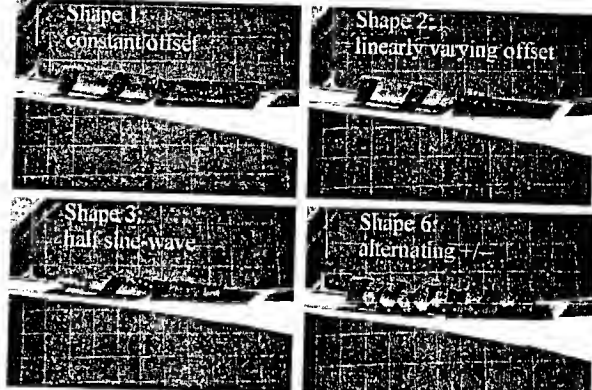


Figure 5. Effector array segments deployed in trailing edge shapes 1, 2, 3 and 6.

potential flow prediction for the region of maximum pressure sensitivity to control surface deflection. Surface pressure taps were positioned 4.05" upstream of the trailing edge of each effector segment, for a total of 24 pressure taps, 12 per wing. The taps were equally spaced in the spanwise direction at intervals of 1.5" with the first tap located 0.75" from the root chord of the removable wing section shown in Figure 3. The taps measured 0.040" in diameter and were connected to a Pressure Systems Inc. Electronic Scanning Pressure (ESP) module through 0.040" diameter nylon tubing.

The ESP module was placed inside the model to minimize the pressure measurement lag associated with tubing length. The ESP had a range of ± 10 H₂O, and was capable of electronically multiplexing up to 32 independent pressure measurements. The ESP was located inside a thermostatically controlled heater box within the model to eliminate the influence of temperature fluctuations on the pressure transducers. Measurements from the 24 pressure taps on the model were electronically scanned and multiplexed by the ESP module at a time interval of 1.5 ms, so the measurement at each tap was updated every 36 ms.

Control Interface

The distributed pressure measurement and effector array control interface was designed and implemented using dSpace™ hardware-in-the-loop computer components and software together with Matlab's Simulink™ programming environment and Real-Time Workshop™ code generation package. The real time control process was implemented with a step size of 0.75 ms.

The experimental setup included the ability to control all moveable surfaces of the model remotely using the dSpace real-time interface. The dSpace system included a dedicated Power PC 750MHz processor, 16-bit A-to-D and D-to-A boards, four digital I/O serial connections and a software interface designed to permit

real-time hardware-in-the-loop execution of control algorithms. The dSpace system was located in the wind tunnel control room. The system not only provided the ability to control the model effectors with open-loop commands, but also to drive them with closed-loop signals from the pressure distribution controller. To achieve this capability it was necessary to implement the data acquisition software that drove the ESP module within the dSpace real-time control algorithm. Four BASIC-X™ servo serial boards were used to translate position commands from the dSpacc system into pulse train signals for the effector servos. Each board could drive up to eight servos. The boards were located within the model and were remotely commanded via the dSpace serial connections using RS232 protocol.

FACILITY AND TEST CONDITIONS

The model was tested in NASA Langley's 12-ft Low Speed Tunnel, operated by the Vehicle Dynamics Branch of the Airborne Systems Competency. The 12-Foot Low-Speed Tunnel is an atmospheric pressure, open circuit tunnel enclosed in a 60-foot diameter sphere. The test section is octagonal, having a width and height of 12 feet and a length of 15 feet with each octagonal side measuring 5 feet. The maximum operating dynamic pressure is $q = 7 \text{ psf}$ ($V = 77 \text{ ft/sec}$ at standard sea level), for a Reynolds number of approximately $490,000 \text{ ft}^3$.

In this experiment, the model was tested over a range of angle of attack (AOA) from -2 to 20 degrees and sideslip from -6 to 6 degrees, and at dynamic pressure of 5 psf, corresponding to tunnel speed of 45 mph. The model's nominal flight speed is 80 mph, and this testing was conducted at approximately half that speed due to limitations associated with heating of the tunnel drive system. The model was mounted on a sting that exited through the lower surface of the fuselage. The mounting system included an internal 6-component strain gauge balance to provide force and moment data. Figure 6 shows the aircraft mounted in the test section.

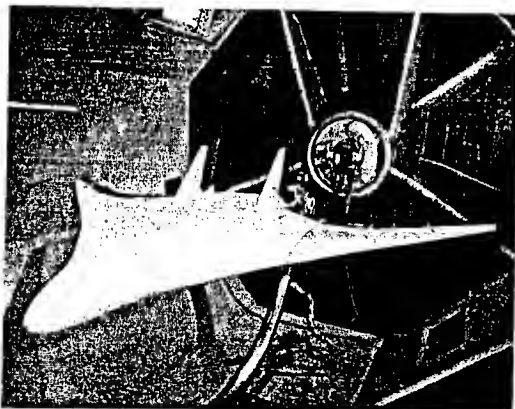


Figure 6. MESA RPV mounted in the NASA Langley 12-Foot Wind Tunnel.

FORCE AND MOMENT RESULTS

Force and moment data obtained from the test were compared with potential flow predictions that had been generated prior to the test. The potential flow analysis was performed using the PMARC code¹¹ with the panel model shown in Figure 4. Potential flow predictions for coefficient of lift and pitching moment vs. angle of attack are compared with wind tunnel data in Figure 7. Moments are referenced to the aircraft center of gravity located 26 inches aft of the nose.

The gradual stall break shown in the upper plot of Figure 7 is typical of blended wing-body configurations. Linear aerodynamic predictions based on potential flow analysis assume inviscid, irrotational, unseparated flow, and so become increasingly unreliable as the vehicle approaches stall. The vehicle trims in 80 mph cruise at approximately 4 degrees AOA, but trims on approach and landing at approximately 9 to 10 degrees. The wind tunnel results indicate a serious reduction in static pitch stability at or near the approach condition.

Potential flow predictions for coefficients of yaw and roll vs. sideslip at the trim angle of attack of 4 degrees are shown in Figure 8. Both of these coefficients exhibit stable trends with sideslip angle. The potential flow analysis appears to provide reasonable predictions for the lateral/directional stability coefficients at the cruise condition, and these characteristics are very similar at the landing condition.

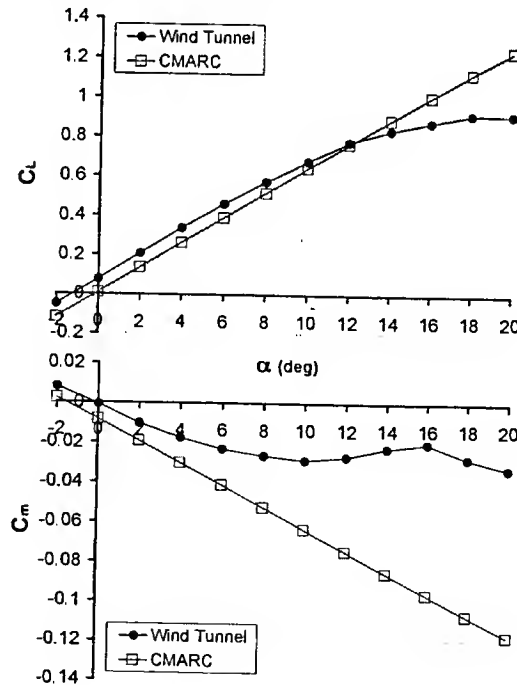


Figure 7. Comparison of wind tunnel data with PMARC predictions for lift (top) and pitching moment (bottom).

Control Authorities – Conventional Effectors

The conventional effectors were tested over their full range of motion in 2-degree increments at AOAs of 0, 4, 8, and 12 deg. Deflection limits for the elevon, aileron, and rudder surfaces are ± 20 , ± 15 , and ± 14 deg, respectively. Positive deflections are defined as trailing edge down for symmetric elevons, right trailing edge up for ailerons, and trailing edge right for rudders.

Control moment vs. surface deflection angle are shown in Figure 9 for an AOA of 4 deg. Primary authorities for pitch due to symmetric elevon, roll due to aileron, and yaw due to rudder are shown at the top of the figure. Secondary (adverse and perverse) moment effects are shown in the plot at the bottom. The plots suggest that the conventional effector suite will provide adequate control authority. Pitch and roll moments due to rudder deflections are not negligible, and will be taken into account in the flight control system design. These data along with additional measurements that were collected during the wind tunnel test have been used in a dynamic simulation to verify that conventional effector suite will provide adequate control authority for typical flight maneuvers. The conventional effectors will be used during non-research portions of flight and as a backup to the shape-change effector array if needed.

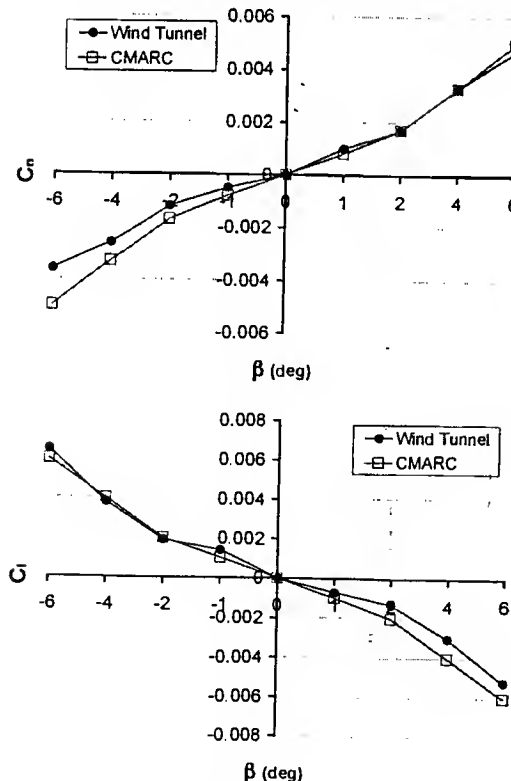


Figure 8. Comparison of wind tunnel data with PMARC predictions for yawing moment (top) and rolling moment (bottom) vs. sideslip, AOA = 4 deg.

Control Authorities – Individual Devices

Control effector deflection sweeps were performed for each of the 24 devices that composed the trailing edge shape-change effector array. Angle of attack and control deflection increments were necessarily coarse to limit the size of the test matrix. Each device was tested over its full deflection range of -15 to +15 degrees in 5-degree increments at four angles of attack (0, 4, 8, and 12 degrees). Remote control of all effector settings through the dSpace console in the tunnel control room permitted automation of the test procedure, which greatly improved the ability to rapidly cover a large test matrix.

Figure 10 shows the pitch, roll, and yaw authority for effector number six, as numbered from inboard to outboard, on the right wing at an angle of attack of 4 degrees. The positive sense of deflection for all the effector array devices is defined as trailing edge up. The behavior is fairly linear and typical of that observed for all the trailing edge devices. Potential flow predictions of control moments produced by deflection of the individual devices were also developed, and these were over-predicted by roughly a factor of 2.

Linear fits to the wind tunnel moment data were used to generate control authority derivatives for each of

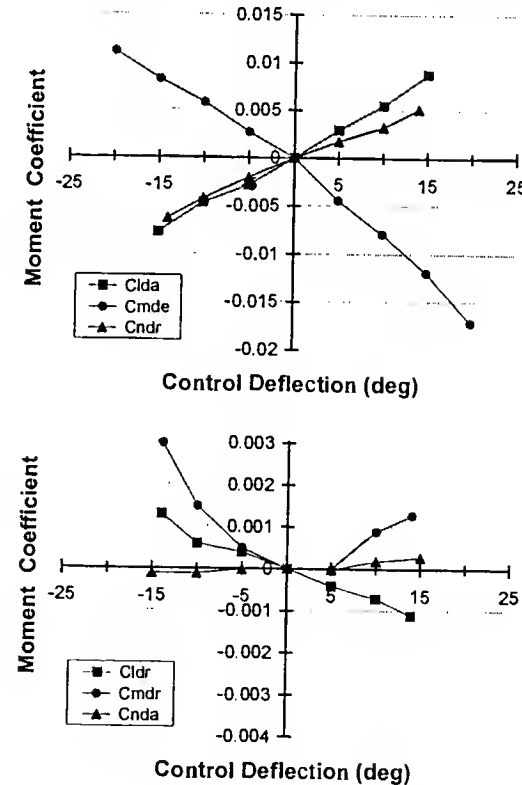


Figure 9. Control moment vs. surface deflection for conventional elevon, aileron and rudder effectors, AOA = 4 deg.

the 24 shape-change effectors. These are presented in Figure 11, where the effector segments are numbered in ascending order from inboard to outboard, with negative numbers corresponding to the left wing array and positive corresponding to the right wing. Hence, effector segment number -12 designates the outboard-most left wing effector, and +12 designates the outboard-most right wing effector.

Deflection of a single effector device clearly produces useful control moments, but the result is small enough that groups of effectors will be required to generate sufficient moments for typical flight maneuvers. The individual devices were particularly ineffective at generating yawing moment, as indicated by Figures 10 and 11. The low yaw authority of the individual effector segments raises the question of deploying the array in collective fashion intended to generate drag on one wing, and thus yawing moment. Such a configuration was among the six predefined deployment shapes that were evaluated during the next portion of the wind tunnel test.

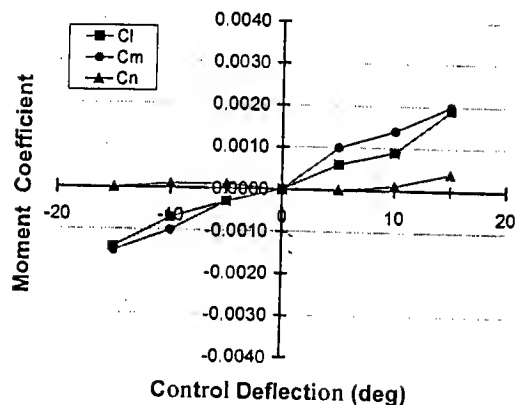


Figure 10. Control moment vs. surface deflection for shape-change effector number 6 on the right wing, AOA = 4 deg.

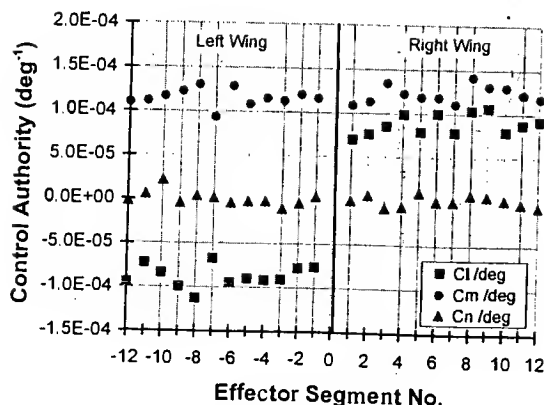


Figure 11. Linearized control authorities for each shape-change device in the trailing edge effector arrays

Control Authorities – Trailing edge Array Shapes

Control moments were measured for the effector array devices deployed collectively to produce trailing edge shapes, as shown in Figure 5. The shapes could be applied to each wing individually or together in a symmetric or anti-symmetric fashion, and with varying scale factor. A scale factor of 15 corresponded to full deflection of the shape, a condition in which one or more of the individual devices had reached saturation. Figure 12 shows a plot of effector deflection vs. segment number for the six trailing edge shapes applied to the right wing with a scale factor of +15. The shapes were tested using scale factors ranging from -15 to +15 in increments of 5.

Figure 13 shows a plot of control moment vs. deflection scale factor for the six trailing edge shapes applied to the right wing only. Not surprisingly, shape 1, which simply sets all devices to a constant deflection, produces the largest pitch and roll moments. But if an objective is to mimic a continuous mold-line effector, then shape 3 appears to generate relatively large moments while satisfying this requirement. Shapes 4 and 6 are capable of generating yaw moment while generating only minimal pitch and roll.

Figures 11 and 13 represent differing approaches to characterizing the authority of the effector array, and their comparison raises important issues regarding methods of control allocation and mixing for effector arrays composed of large numbers of relatively low-authority devices. One issue is whether allocation should be based on individual device authorities, or rather upon authorities of basis functions representing collective deployment configurations. Both approaches have pros and cons. As devices composing the array become smaller and more numerous, the dimension of the control matrix goes up while individual authority goes down, increasing the potential for ill-conditioned matrices.

Also, in some cases, the devices will only be effective when deployed collectively in a particular combination, and this effect may be missed by an individual device-wise characterization. A good example is the generation of yawing moment. When the yawing moment of the crow mix configuration (shape 6) was predicted by using superposition of the individual linearized device authorities, the result was less than 60% of the measured authority for that configuration. Presumably, device interactions were important in this configuration, and these effects were not captured by the individual linearized authorities.

A basis function approach appears to provide a means of reducing the high dimensional low authority challenge, but is also likely to lead to difficulty in deriving full authority from the array when a basis function is commanded to saturation. Furthermore, how should such bases be identified? In the MESA experiment the

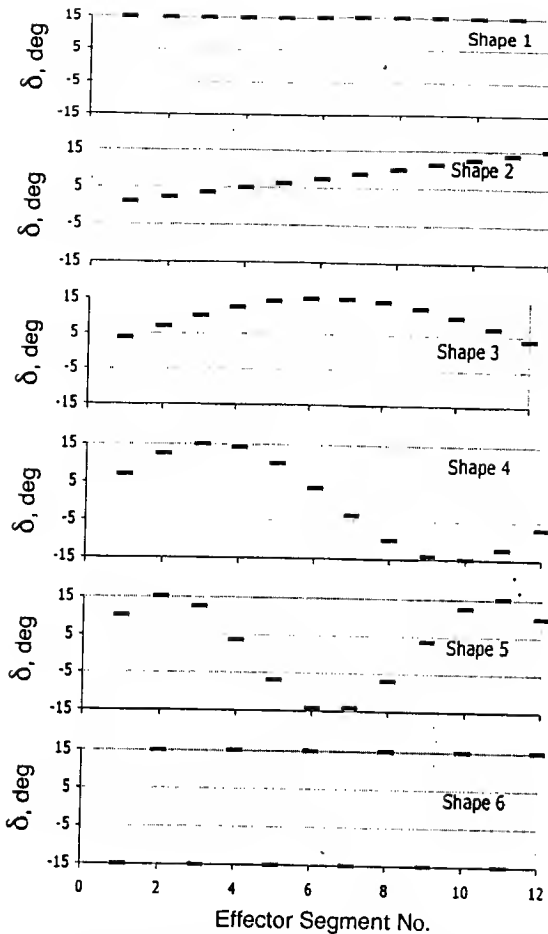


Figure 12. Effector deflection vs. segment number for the six trailing edge shapes applied to the right wing with a scale factor of +15.

crow mix configuration was selected for shape 6 as a likely yaw generator based upon conjecture. But perhaps alternating in groups of two might have been even more effective.

Hence, there is a need for methodologies to provide thorough and efficient characterization of high dimensional arrays. Whether experimentally or analytically evaluated, the test matrix must explore combinations of device deflections to identify significant nonlinearity and interactions, and the combinatorial possibilities increase rapidly with the number of elements in the array. If the control effector suite of future flight vehicles is truly progressing toward large networks of distributed devices, issues such as allocation, efficient testing, and characterization of high dimensional effector arrays will become increasingly significant. Potential solutions may arise from a blending of information technology concepts with flight control. Decentralized approaches may be envisioned that draw upon principles from collaborative robotics, network theory or cellular automata.

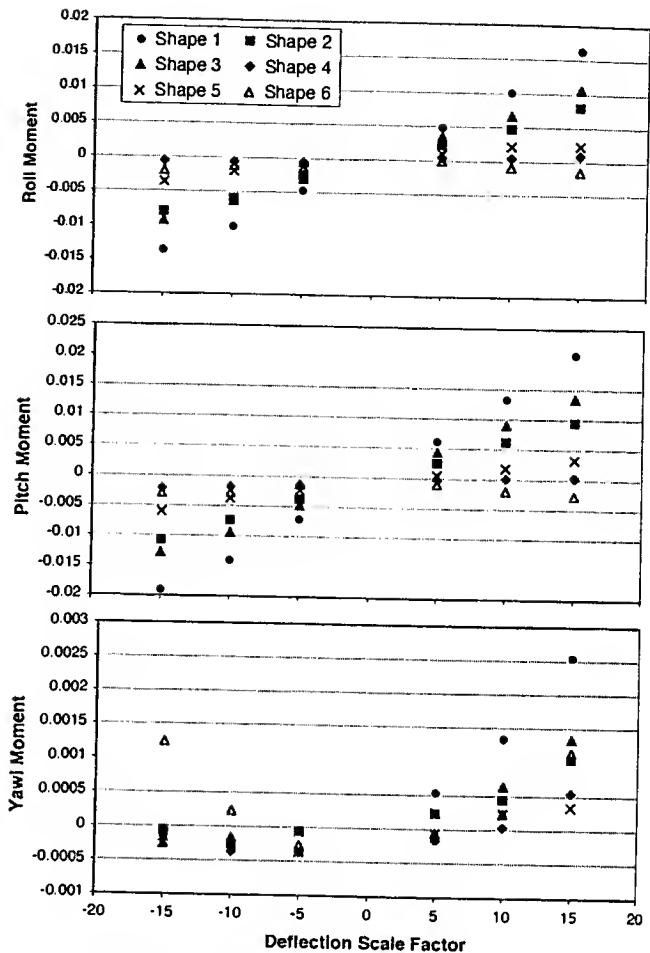


Figure 13. Control moment vs. deflection scale factor for the six trailing edge shapes applied to the right wing, AOA = 4 degrees.

PRESSURE MEASUREMENT AND CONTROL

Variations in the spanwise pressure distribution were measured in response to deflections of the individual trailing edge effectors. The influence of an effector deflection was greatest at the closest pressure measurement, and diminished as distance to the measurement location increased. This trend is clearly visible in the plot of spanwise pressure measurements in response to deflections of +15 and -15 degrees for shape-change effector segment number 4 on the right wing, shown in Figure 14. This plot provides an indication of the degree to which maximum deflection of a single device is able to influence the spanwise pressure distribution.

Pressure measurements such as those shown in Figure 14 were collected for each of the 24 shape-change effectors at settings of -15, -10, -5, 5, 10, and 15 degrees for angles of attack of 0, 4, 8 and 12 degrees. The measurements were then used to generate pressure sensitivity matrices for the effector and sensor array using a least-

squares fit to the pressure variation in response to effector deflection at each sensor location. This process resulted in a separate 12x12 pressure sensitivity matrix for the right and left wings at each angle of attack.

The pressure sensitivity matrices tended to be diagonally dominant since each device influenced its own pressure measurement most strongly, with diminishing influence on adjacent measurements. A representative sensitivity matrix for the right wing at 4 degrees angle of attack is shown in Figure 15 as a colormap of the sensitivities. The pressure sensitivity matrices were used in the formulation of a feedback control system that was designed to achieve and regulate a commanded spanwise pressure distribution at each of the 24 sensor locations.

Pressure Distribution Control Design

The MESA testbed was developed to explore the use of *multifunctional* effector and sensor arrays. A fundamental aspect of the research is to investigate control concepts that exploit the ability of these arrays to simultaneously perform a variety of tasks such as flight

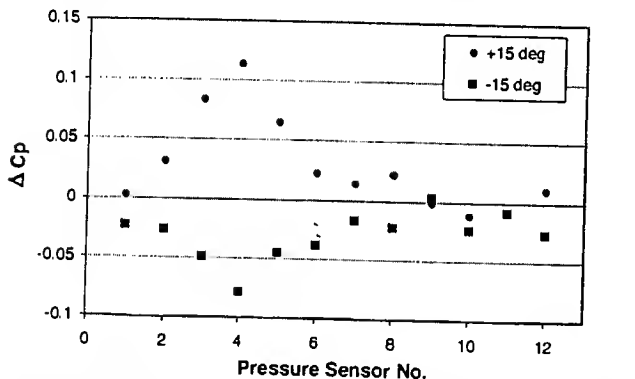


Figure 14. Pressure variations in response to deflections of effector segment 4 on the right wing, AOA = 4 deg.

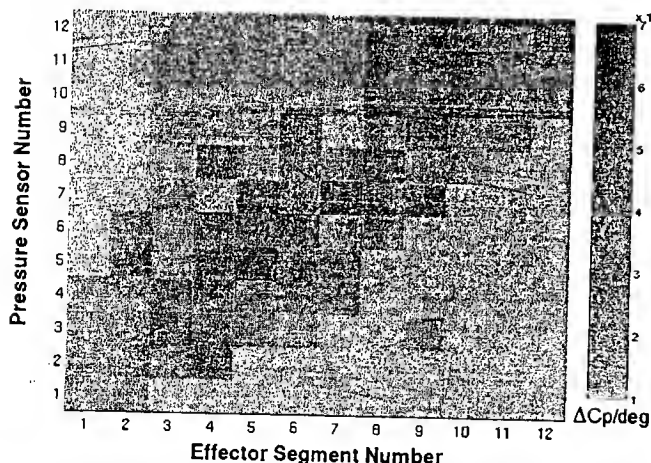


Figure 15. Colormap of pressure sensitivity matrix for right wing effector and sensor array at 4 degrees AOA.

control, mission-adaptive performance enhancement, health monitoring, distributed load alleviation, or distributed flutter suppression.

The ability to sense and modify the spanwise pressure distribution acting on the wing would presumably have application to distributed load alleviation and mission-adaptive performance enhancement functions by providing the capacity to tailor the spanwise lift distribution. Such tasks might be assigned a lower priority and performed concurrently with the task of generating moments for flight control purposes. To further examine this possibility a pressure distribution control system that uses the effector and sensor array was developed. The system uses a time domain implementation of the least mean squares (LMS) algorithm^{12,13} to achieve and regulate a commanded spanwise pressure distribution consisting of specified conditions at each of the 24 pressure measurement locations.

For the controller synthesis, let the ($n \times 1$) vector of pressure coefficient variations be given by,

$$\mathbf{C}_p = \mathbf{H}\mathbf{d} \quad (1)$$

where \mathbf{d} is the ($n \times 1$) vector of effector displacements, and \mathbf{H} is the ($n \times n$) sensitivity matrix relating effector displacements to pressure variation. The error vector of differences between the measured and desired pressure coefficient vectors is denoted,

$$\mathbf{e} = \mathbf{C}_{p\text{desired}} - \mathbf{C}_{p\text{measured}} \quad (2)$$

where $\mathbf{C}_{p\text{measured}} = \mathbf{C}_p$ in the case of zero measurement error (no external perturbations, no measurement noise). The nominal control objective is to minimize the error in Eq. 2 subject to constraints on the maximum effector displacement. This is achieved by minimizing the objective function, J :

$$J = E\{\mathbf{e}^T(n)\mathbf{e}(n)\} \quad \text{subject to} \quad c_i(\mathbf{d}) < 0, \quad i = 1, \dots, n \quad (3)$$

where $E\{\cdot\}$ is the expectation operator, and c_i is the i^{th} convex constraint on the effector displacement vector, \mathbf{d} . The control objective function may be rewritten to include the constraints as penalties:

$$J = E\{\mathbf{e}^T(n)\mathbf{e}(n)\} + \sigma \sum_i^n [c_i(\mathbf{d})]_z^2 \quad (4)$$

where σ determines the relative importance of the constraints in the objective function. The constraint penalty term, $[c_i(\mathbf{d})]_z$, in Eq. 4 is defined by,

$$[c_i(\mathbf{d})]_z = \max[c_i(\mathbf{d}), 0] = \begin{cases} 0 & c_i(\mathbf{d}) \leq 0 \\ c_i(\mathbf{d}) & \text{otherwise} \end{cases} \quad (5)$$

The LMS algorithm is a stochastic gradient descent procedure for solving a least squares problem, such as

Eq. 4. At the k^{th} time step, new values for the displacements are computed according to,

$$\mathbf{d}(k+1) = \mathbf{d}(k) - \mu \frac{\partial J}{\partial \mathbf{d}} \quad (6)$$

where μ determines the rate of adaptation. The LMS algorithm uses an instantaneous estimate of the gradient. This estimate is given by:

$$\frac{\partial J}{\partial \mathbf{d}} = 2 \left(-\mathbf{H}^T \mathbf{e} + \sigma \sum_i [c_i(\mathbf{d})]_z \frac{\partial c_i}{\partial \mathbf{d}} \right) \quad (7)$$

Let the i^{th} constraint be defined such that the absolute value of the deflection of the i^{th} effector must be less than a maximum deflection, d_{\max} . Thus,

$$c_i = |d_i| - d_{\max} \quad (8)$$

Therefore,

$$\frac{\partial c_i}{\partial d_j} = \begin{cases} \text{sign}(d_i) & \text{for } i = j \\ 0 & \text{otherwise} \end{cases} \quad : \quad (9)$$

With the preceding definitions, the update for the i^{th} effector displacement is,

$$d_i(k+1) = d_i(k) - \mu [-\mathbf{H}(:,i)^T \mathbf{e}(k) + \sigma [c_i]_z \text{sign}(d_i)] \quad (10)$$

where $\mathbf{H}(:,i)^T$ denotes the transpose of the i^{th} column of \mathbf{H} . After initial simulations of the algorithm a further constraint was added that enforced smoothness of the effector deployment distribution by penalizing large displacements relative to adjacent effectors. The array was thus made to approximate a seamless continuously deformable shape-change trailing edge effector. The update expression was implemented in C-code for real-time control of the model hardware during the wind tunnel test. The shape change deflection angle limit, d_{\max} was set to 15 degrees. The parameters μ and σ were assigned values of 1.0 and 0.1, respectively.

Pressure Distribution Control Test Results

The controller was evaluated during the closed-loop portion of the wind tunnel test. A series of pressure distribution commands was created based on known achievable distributions that had been measured during the previous portion of the test. Figure 16 shows an example time history of the commanded and measured pressure coefficients at a single pressure tap as the controller attempted to track a series of step commands. Figure 17 shows a time history colormap of commanded pressure coefficients (top) and measured pressure coefficients (bottom) at all 24 sensor locations from the run shown in Figure 16. Figure 18 shows a 3-d plot of control effector deflections from the same time history.

The LMS controller is clearly effective in commanding the shape changes required to achieve the

desired spanwise pressure distribution at the trailing edge sensor array. The relatively long rise time of the closed loop system shown in Figure 16 represents a trade-off between speed of convergence and measurement noise rejection. This trade is controlled by the adaptation rate parameter, μ . For this experiment, the parameter was assigned a value of 1.0, resulting in a rise time of approximately 5 seconds, which is sufficient for a flap-like cruise performance optimization function. Future experiments will vary the adaptation parameter to investigate the potential for faster convergence.

The results suggest the potential to employ a similar approach to command larger scale shape changes of a continuously deformable aircraft structure, such as envisioned by the Aircraft Morphing Program, to generate a desired global pressure distribution for mission-adaptive performance optimization or distributed load alleviation purposes. Yet to be addressed is the prioritization and blending of these functions with the multi-axis moment generating functions required for stabilization and maneuver control if the same *multifunctional* array is used for both purposes.

CONCLUDING REMARKS

This report has described a project that seeks to investigate controls challenges associated with novel effector and sensor concepts within NASA's Aircraft Morphing Program. In particular, the potential exists to shift the composition of an aircraft's control effector suite from a small number of high authority, specialized devices (rudder, aileron, elevator, flaps), toward arrays composed of larger numbers of smaller, less specialized, distributed effector and sensor devices able to simultaneously perform a variety of control functions using feedback from disparate data sources. To investigate this concept, a remotely piloted flight vehicle has been equipped with an array of 24 trailing edge shape-change effectors and associated pressure measurements to create a representative testbed that embodies the fundamental controls challenges.

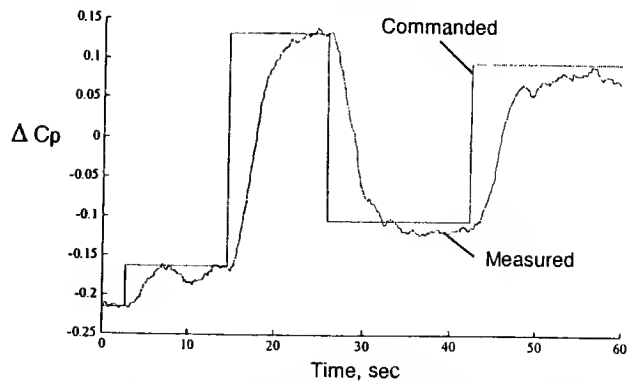


Figure 16. Time history of commanded and measured pressures at a single sensor location, AOA = 4 degrees.

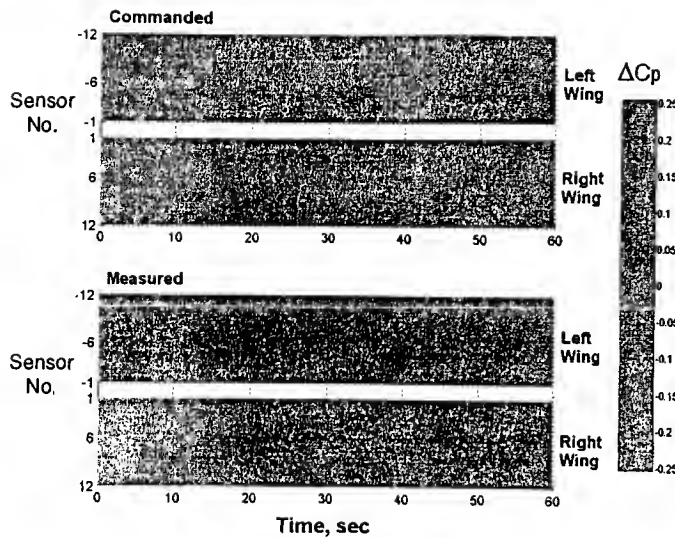


Figure 17. Example time history of commanded and measured pressures at all 24 sensor locations.

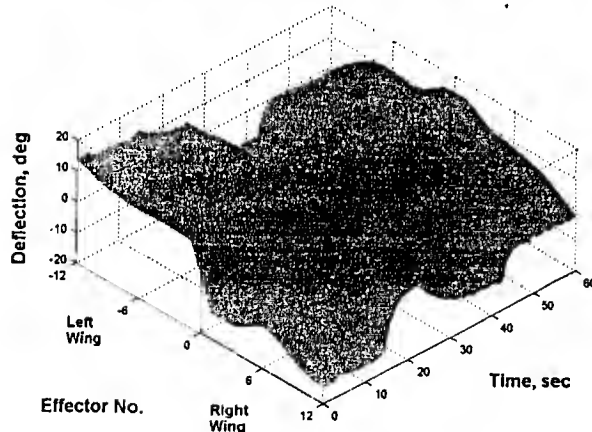


Figure 18. Time history of shape-change effector deflections from pressure distribution controller.

The vehicle, called the Multifunctional Effector and Sensor Array (MESA) testbed, was tested in NASA Langley's 12-ft Low Speed wind tunnel to characterize its stability properties, control authorities, and distributed pressure sensitivities, and to evaluate the design of a spanwise pressure distribution controller that used the model's trailing edge effector and sensor arrays to achieve a commanded spanwise pressure distribution. The design of the pressure distribution controller was described and results from its implementation during the wind tunnel experiment were presented.

The results show that the multifunctional effector and sensor array has the potential to generate sufficient moments for multi-axis flight control purposes as well as to achieve and regulate the spanwise pressure distribution for possible mission adaptive performance optimization or active load alleviation purposes. The control

approach offers promise for application to larger scale continuously deformable shape-change configurations such as those envisioned in the Morphing Program. Challenges associated with control characterization and allocation for high dimensional effector arrays were noted and have yet to be addressed. Prioritization and blending of flight control and pressure regulation functions are also topics requiring additional research.

REFERENCES

- Kroo, I.: "Aerodynamic Concepts for Future Aircraft," AIAA Paper 99-3524, July 1999.
- Park, M.A.; Green, L.L.; Montgomery, R.C.; Raney, D.L.: "Determination of Stability and Control Derivatives Using Computational Fluid Dynamics and Automatic Differentiation", AIAA 99-3136, June 1999.
- Padula, S.L.; Rogers, J.L.; Raney, D.L.: "Multidisciplinary Techniques and Novel Aircraft Control Systems", AIAA paper 2000-4848, April 2000.
- Raney, D. L., Montgomery; R. C., Green, L.L.; Park, M. A.: "Flight Control using Distributed Shape-Change Effector Arrays," AIAA paper 2000-1560, April 2000.
- Bieniawski, S.; Kroo, Ilan M.: "Flutter Suppression Using Micro-Trailing Edge Effectors", AIAA paper 2003-1941.
- Lee, Hak-Tae; Kroo, Ilan M.; Bieniawski, S.: "Flutter Suppression for High Aspect Ratio Flexible Wings Using Microflaps", AIAA 2002-1717, 43rd AIAA Structures, Structural Dynamics and Materials Conf, April 2002.
- Florance, J.P.; Burner, A.W.; G.A.; Hunter, C.A; Graves, S.S.; Martin, C.A.: "Contributions of the NASA Langley Research Center to the DARPA/AFRL/NASA/Northrop Grumman Smart Wing Program", No. 2003-1961, AIAA Dynamics Specialists Conf, April 2003, Norfolk, VA
- Martin, C.A., et al.: "Design, Fabrication, and Testing of Scaled Wind Tunnel Model for Smart Wing Phase 2 Program", No. 4332-50, SPIE Symposium on Smart Structures and Materials, Newport Beach, CA, March 2001.
- Wang, D. P.; Bartley-Cho, J.D.; Martin, C. A.; Hallam, B. J.: "Development of High-Rate, Large Deflection, Hingeless Trailing Edge Control Surface for the Smart Wing Wind Tunnel Model", Vol. 4332, pp.401-418, SPIE Symposium on Smart Structures and Materials, Newport Beach, CA, 5-8 March 2001.
- Barnwell, William G.: "Distributed Actuation and Sensing on an Uninhabited Aerial Vehicle", Thesis for Master of Science in Aerospace Engineering at North Carolina State University, MAE Dept, August 2003.
- Ashby, D. L., Dudley, M. R., Iguchi, S. K., Browne, L., Katz, J., "Potential Flow Theory and Operation Guide for the Panel Code PMARC," NASA TM-102851, Jan 1991.
- Haykin, S.: *Adaptive Filter Theory*. Prentice Hall, 1991, Englewood Cliffs, NJ; ISBN 0-13-013236-5.
- Rafaeli, B.; Elliott, S. J.: "A Computationally Efficient Frequency-Domain LMS Algorithm with Constraints on the Adaptive Filter", IEEE Transactions on Signal Processing, Vol. 48, No. 6, June 2000, pp. 1649-1655.

**Update Report for
UAV Flight Control Using Distributed Actuation and Sensing**

**S. Todd Lion
Mechanical and Aerospace Engineering
North Carolina State University
Raleigh, NC**

5/8/2005

1. INTRODUCTION

Recent research in aerodynamics has shown that certain advantages can be created by replacing high authority, specialized control surfaces (rudder, aileron, elevator, flaps) with smaller, more adaptable, less specialized effector arrays¹. North Carolina State University and the National Aeronautics and Space Administration (NASA) recently joined on a project to incorporate a distributed actuation and sensing array on a blended-wing-body (BWB) uninhabited aerial vehicle (UAV). The model was designed and constructed at NC State and the wings underwent initial wind tunnel tests in the NC State subsonic wind tunnel². Each wing of the UAV is equipped with 12 small, independent effectors that act together to form a discretized approximation of a morphing wing. The flight vehicle, called the Multifunctional Effector and Sensor Array (MESA) testbed was then transported to the NASA Langley Research Center to undergo a series of tests in July, 2004, in the 12-foot subsonic wind tunnel. This report summarizes the model and test configuration and gives an overview of the effectiveness of the effector array for hopeful use in future flight testing.

2. EXPERIMENTAL SET-UP

2.1 Test Model

The MESA testbed was created from a BWB UAV designed and constructed at NC State University as a senior design project in aerospace engineering in 2001-2002. The aircraft, named *Thunderstruck* (Figure 1), shares its general planform shape with the NASA BWB design³. The aircraft⁴ is comprised of a NACA 0015 airfoil with a 58" root chord tapering to a 5-1/4" tip chord with a mean aerodynamic chord of 34.3". The UAV has a wing area of 17.77ft² over its 9.38' wingspan. The aircraft is powered by an Aviation Microjet Technology? AT180 mini-turbojet engine rated at 15-lbf static thrust. The aircraft has a dry weight of 30 lb. with capacity for a 15 lb. payload. The aircraft is dolly-launched and skid-landed, so no landing gear is required on the airframe.

Modifications specific to the MESA testbed² consisted of replacing the outboard wing sections with custom-built sections containing the effector array. The outer 31-1/4" of wing (21" root chord, 5-1/4" tip chord) were replaced with new sections capable of housing the effector and sensor array. A change in sweep occurs 9" from the root of the section. Twelve

effectors are located on each wing, with the first effector located at the root of the wing section and the twelfth effector located 18" from the root. Six effectors are located before the break in sweep angle. The outboard section of wing houses a conventional hinged control surface. The completed wing section can be seen in Figure 2. Each effector has dimensions of 0.007" (thickness), 1.5" (width), and 4" (length) and is created from two rectangular elements of spring steel, one each for the upper and lower surfaces. The attachment scheme of the spring steel allows the effectors to deflect in the fashion of a contoured, hingeless control surface. Each effector is actuated by a pull-pull mechanism driven by a Hobbico? CS-5 nano-servo, as shown in Figure 3. Each effector is capable of fully independent motion with deflections of $\pm 15^\circ$ at a maximum rate of no less than 2 Hz. Some examples of effector deflections are shown in Figure 4. The MESA testbed can be seen in Figure 5. Control surface configuration on this aircraft is as follows: elevons (most inboard), MESA array, and ailerons (most outboard), with conventional rudders on the vertical tails.

The modified wing sections also incorporate a single surface pressure tap, 0.040" in diameter, placed 4.05" from the trailing edge of each effector on the upper surface, giving a total of 24 sensors across the two wings. Each pressure tap is located 0.75" from the edge of its paired effector, immediately forward of the center of the effector. Nylon tubing, 0.040" diameter, connects the tabulations to the pressure monitoring system. The pressures were monitored by a Pressure Systems Inc.? ESP 32HD electronic scanning pressure module.

2.2 Data Collection Devices

The ESP module was placed inside the test model to minimize the length of the pressure tubing. The module was also placed inside a thermostatically controlled heater box located within the model to eliminate the influence of temperature variations in the tunnel on the pressure transducers. The ESP has a range of $\pm 10^\circ$ of water and is capable of electronically multiplexing up to 32 independent pressure measurements. Pressure measurements¹ from the 24 taps on the model were scanned and multiplexed by the ESP at a 1.5ms time interval, so the measurement at each tap was updated every 36ms.

The pressure measurement and effector control interface¹ was designed and implemented using dSpace™ hardware-in-the-loop computer components and software together with Matlab Simulink™ and Real-Time Workshop™. The dSpace interface allows for control of all moveable surfaces on the model with open-loop commands as well as closed-loop signals from the pressure or bank angle controller. Four BASIC-X™ servo serial boards were located within the model to translate the dSpace position commands to pulse train signals for the effector servos. Each board can control up to eight servos and was controlled remotely from the dSpace serial connections using the RS232 protocol.

2.3 MESA Installation

The MESA testbed was modified internally to add a mounting point for the static force balance. This added no protuberances or alterations to the exterior of the aircraft except for a small hole, approximately 2" x 2", in the bottom center of the fuselage through which the sting was mounted. The sting used was an internal 6-component strain gauge balance, which was mounted on a 12" standoff post. The moment center was set at 30.88" from the nose of the aircraft.

The second portion of the test required the installation of a free-to-roll (FTR) rig. The same general mounting scheme was used for the aircraft, and the only exterior modification that needed to be made was a widening of the hole in the base of the fuselage to allow for a $\pm 50^\circ$ roll of the aircraft. This sting collected no force or moment data. The angular position of the model was the only data able to be collected from the sting.

2.4 Wind Tunnel

The NASA Langley 12-Foot Subsonic Wind Tunnel, operated by the Vehicle Dynamics Branch of the Airborne Systems Competency, is an atmospheric pressure, open return tunnel with an octagonal test section measuring 12' across and 15' in length contained within a 60' diameter sphere. Each side of the test section octagon measures 5'. The maximum operating dynamic pressure (q) of the tunnel is 7psf, which equates to 77ft/s at standard sea level density and a Reynolds number of approximately 490,000ft⁻¹. All runs with the MESA testbed installed were at an operating q of 5psf, or 65ft/s at standard conditions. The aircraft's designed cruise speed is 117ft/s, but the velocity had to be lowered in the tunnel

due to rapid heating of the fan motor at higher speeds due to the model's high blockage of the test section. Figure 6 shows the MESA testbed mounted in the Langley 12-foot tunnel.

2.5 Test Schedule

The wind tunnel tests can be broken down into four subsections: baseline aircraft and conventional control surfaces, effector shapes, single effector sweeps, and free-to-roll tests.

2.5.1 Baseline Aircraft and Conventional Control Surfaces

Testing began with a series of sideslip (β) runs from -5° to $+5^\circ$ at zero angle of attack (a). Following this, the model was set to zero β and run through a range of a's from -2° to $+20^\circ$. The conventional control surfaces were tested next, all at zero β and an a range from -2° to $+12^\circ$. The ailerons were tested in both anti-symmetric and symmetric configurations with deflection angles (d) of -15° to $+15^\circ$. The elevons were tested in symmetric fashion over a d range of $\pm 20^\circ$, as were the rudders over a $\pm 14^\circ$ range.

2.5.2 Single Effector Sweeps

Each effector was run through an entire $\pm 15^\circ$ d sweep at each operating a of $+4^\circ$, $+6^\circ$, and $+8^\circ$. For these sweeps, only the desired effector was deflected; all other control surfaces were set to zero d.

2.5.3 Effector Shapes

Three elementary shapes (linear, sine wave, and zigzag) were used as the basis for the six effector configurations (shown in Figure 7). Shape 1 refers to a deflection of all 12 effectors by the same angle, resulting in a straight horizontal line at the trailing edge, simulating a conventional control surface. Shape 2 is another variant of the linear shape; the control surfaces attempt to form a linear variation between effector #1 and #12. Shapes 3, 4, and 5 all play on the sine wave shape. Shape 3 is a half of a sine wave, shape 4 is one complete wave, and shape 5 is a period and a half of a wave. Shape 6 couples each pair of effectors with opposite deflections of equal magnitude, resulting in a "one up, one down" zigzag configuration.

Each of these configurations was tested over a range of $+2^\circ$ to $+12^\circ$. Shapes 1, 2, and 3 were tested over d 's of $\pm 15^\circ$ at each a in both symmetric and anti-symmetric fashions. Shapes 4, 5, and 6 were only tested one side at a time (i.e. deflected right wing effectors, zero left wing effectors), as these were believed to be more inducing of drag, and therefore yawing moment, than any other force. Each configuration was tested as left wing only and right wing only over maximum d 's ranging within $\pm 15^\circ$ at each a .

2.5.4 Free-to-Roll

The final set of tests was performed with the FTR rig installed. Due to the limitations in this rig, no force or moment data could be collected. Runs instead focused on open-loop and closed-loop control of the bank angle of the aircraft. The passive response of the aircraft to initial roll angles was tested by setting a bank angle (F), locking the FTR rig into place, returning all control surfaces to trim, and unlocking the FTR rig. Closed-loop control was tested with both conventional control surfaces and the effector array. Desired outputs for the aircraft included F step functions and F sine waves. Pressure data time histories were recorded for select rolling experiments. It should be noted that the elevons were applied anti-symmetrically to trim the aircraft in roll, thereby leaving the ailerons at zero d except when commanded.

3. DATA ANALYSIS

3.1 Baseline Aircraft

Baseline tests with no control surface deflections over a and β sweeps are graphed in Figure 8. This figure shows very little dependence on sideslip angle for lift and pitching moments. The aircraft shows a gentle stall near an a of 19° . The slow stall is typical of BWB aircraft. The pitching moment curve shows a period of static instability between a 's of 10° and 16° . This unstable region has been previously noted during flight testing of the *Thunderstruck* UAV⁵. The aircraft trims for approach⁴ at approximately 8° - 10° , which is shown to have significantly reduced static stability.

3.2 Conventional Control Surfaces

The results of the anti-symmetric aileron sweeps are shown in Figure 9. Similar to the baseline runs, very little α dependence is seen in the roll authority of the ailerons. Likewise, symmetric rudders are plotted in Figure 10, and symmetric elevons in Figure 11. A slight amount of adverse roll is seen with the rudder deflections. The symmetric elevons show some variation in lift coefficient over the α range, but a large portion of this can be attributed to the small magnitudes of lift generated and limitations with the force balance. At high positive elevon deflections (trailing edge down), a dependence is again seen. The variation grows larger with increasing α ; this can easily be attributed to impinging stall or separation over the upper surface of the elevon at large deflections. Symmetric aileron deflections were also tested (Figure 12). The primary control authorities from these deflections are pitching moment and lift coefficients. The pitching moment shows little variation with α , but the lift coefficient shows a similar style as what was seen with the elevon deflections. Once again, this can most likely be attributed to the small magnitudes of lift. The outlying line on both curves is the case for $\alpha=4^\circ$. A summary of the control authority of these four scenarios at zero α can be found in Table 1.

3.3 Individual Effectors

Each effector was run through a range of deflections from -15° to $+15^\circ$ at α 's of 4° , 6° , and 8° . Figures 13 and 14 show the pitching moment response to each effector deflection at $\alpha=4^\circ$ for the right and left wings, respectively. All the effectors induce a similar response in aircraft pitching moment through their α range. Table 2 lists the control powers for lift, pitch, and yaw for each effector on the right wing. Consistency is lacking across the effectors in lift control power; this is once again likely due to the small magnitudes of lift and the limitations of the force balance. Pitching and roll control show much more consistency across the effectors. It is of interest to note that effector #7 consistently shows control values lower than all other effectors. This effector is the first surface after the change in sweep of the wing. A small section of the trailing edge of this effector had to be cut away to allow it to move past effector #6. Thus, the surface area of this effector is lessened, and it is only logical that the control powers would also be reduced. Table 3 lists the same control powers for the left wing, and similar observations can easily be made.

3.3 Effector Shapes

Effector array shape 1 simulates a conventional control surface, and it can be directly correlated to a set of elevons (symmetric deflection) or ailerons (anti-symmetric deflection). Figure 15 shows the lift and pitching moment coefficient response to a symmetric shape 1 deflection. The roll moment coefficient response to the anti-symmetric shape 1 deflection is shown in Figure 16. Figures 17 and 18 show the same attributes of the model to a shape 2 deflection, and Figures 19 and 20 show them for a shape 3 stimulus. Clearly, shape 1 is the most powerful of the three for commanding pitch or roll changes. However, it could also be beneficial to examine the drag production of each of these shapes. Intuitively, one would assume that shape 1 would produce the most drag of the three shapes due to its distinct tips at the edge of the array surface. Shape 2 only has one exposed tip to induce drag, and shape 3 has none. Indeed, Figures 21 through 24 show that shape 1 produces significantly more drag than either shape 2 or 3 in both symmetric and anti-symmetric configurations. Figures 25 and 26 compare shapes 2 and 3 and show very similar drag characteristics from both configurations.

Knowing that shapes 2 and 3 produce less drag than shape 1 but also have less authority, it is desired to discover which is more efficient. Figure 27 displays lift to drag ratio for the entire aircraft for shapes 1, 2, and 3 for an α of $+6^\circ$. All three configurations have very similar ratios over the negative deflection range. For high positive deflections, shape 1 has a considerable lower ratio than the others. This is most likely due to the high deflections in combination with the angle of attack of the aircraft creating some separation over the upper surface of the effectors. For shapes 2 and 3, a much smaller number of effectors are displaced to such a large angle, so the amount of separation should be much smaller. Figure 28 shows rolling moment to drag ratio. Surprisingly, shape 1 is the most efficient of the three, opposite of the expectations of the results. Figure 29 shows a similar trend for pitching moment to drag ratio. This could be due to the limitations imposed by the discretized approximation of a continuously morphing trailing edge. Each effector can create trailing tip vortices. Additionally, the sides of the effectors are hollow, allowing the possibility of air to become “trapped” within the effector and create drag from the inside surfaces of the effector.

Shapes 4, 5, and 6 were initially believed to be useful only for drag and yawing purposes. Figure 30 and 31 show the drag coefficients for these shapes at an α of $+6^\circ$. Note that each plot only displays one side of the aircraft; in order to obtain drag values that would be obtained for deflections applied to both sides of the aircraft, the values of these two figures should be summed. Referring back to the drag values shown for shapes 1, 2, and 3 in Figures 22 and 24, it is clear that shape 6 creates considerably higher drag than any other configuration. Figures 32 and 33 translate these single-sided drag forces into yawing moments. Shape 6 shows a significant moment was created, but it is not as high as the moments generated by the rudders (Figure 10). Perhaps a larger array or a similar array placed farther outboard on the wings could create a yawing moment high enough to be capable of entirely replacing the rudder. Lift, pitching moment, and rolling moment coefficients (Figures 34-37) are almost negligible for these configurations when compared to shapes 1, 2, and 3 (Figures 15-20). Barnwell² has previously shown the pressure distributions of these three shapes to be relatively flat, so it would logically follow that relatively no lift would be created.

4. PREDICTION SCHEMES

Using the control powers discovered from the single effector runs detailed in Tables 2 and 3, it is possible to predict the control authority of any shape the effector array can create. For any given effector and deflection, it is known how to find its resultant control authority:

$$C_L = C_{Ly} \cdot f \cdot \frac{?C_L}{?f}$$

Expanding this to n flaps:

$$C_{L,total} = \sum_{i=1}^n C_{Ly,i} \cdot f_{i,i}$$

Figures 38 and 39 show this technique applied to a shape 1 configuration for pitching and rolling moment and lift coefficients. It is clear that this method is reasonably accurate for this configuration. Figures 40 and 41 display a good deal of accuracy for a shape 2 configuration. An obvious source of error lies in the determination of the control power for the effectors. Each effector creates a very small change in aircraft aerodynamics, and small disturbances in the force balance and data collection systems could contribute significantly

to error in control authority. Even so, the method described above is shown to be very accurate for primary coefficient prediction.

5. CONCLUDING REMARKS

It has previously been shown¹ that closed-loop spanwise pressure regulation is possible and accurate, giving the effector array the possibility to be tailored for structural considerations or mission-specific optimizations. Additionally, the array adds a great deal of redundancy and is capable of compensating for the loss of power to an effector¹. With this new research, it is seen that the MESA platform is capable of sufficient control in all axes for aircraft flight. Given accurate testing of each individual effector, it is simple to generate an accurate prediction for multiple effector configurations.

6. TABLES

Table 1. Control powers for conventional control surfaces at zero angle of attack.

| | $C_{Ldf} * 10^4$ | $C_{mdf} * 10^4$ | $C_{ldf} * 10^4$ | $C_{ndf} * 10^4$ | $C_{ydf} * 10^4$ |
|-------------------------|------------------|------------------|------------------|------------------|------------------|
| Anti-Symmetric Ailerons | -1.423 | 1.377 | 7.044 | 0.00192 | 0.5418 |
| Rudders | 1.599 | -0.5097 | -0.9966 | 4.306 | -18.80 |
| Elevons | -29.95 | 7.845 | -0.2355 | -0.01735 | -0.3040 |
| Symmetric Ailerons | -19.28 | 9.591 | 1.229 | 0.1597 | -0.3975 |

Table 2. Lift, pitch, and roll control powers for right wing effectors at $\alpha = 4^\circ, 6^\circ$, and 8° .

| Effector Number | $\alpha = 4^\circ$ | | | $\alpha = 6^\circ$ | | | $\alpha = 8^\circ$ | | |
|-----------------|--------------------|------------------|------------------|--------------------|------------------|------------------|--------------------|------------------|------------------|
| | $C_{Ldf} * 10^4$ | $C_{mdf} * 10^4$ | $C_{ldf} * 10^4$ | $C_{Ldf} * 10^4$ | $C_{mdf} * 10^4$ | $C_{ldf} * 10^4$ | $C_{Ldf} * 10^4$ | $C_{mdf} * 10^4$ | $C_{ldf} * 10^4$ |
| 1 | -5.416 | 1.220 | 0.8950 | -5.450 | 1.435 | 0.7531 | -6.494 | 1.360 | 0.8043 |
| 2 | -4.425 | 1.092 | 0.9735 | -3.943 | 1.047 | 0.7667 | -3.546 | 1.089 | 0.7207 |
| 3 | -5.020 | 1.196 | 0.9896 | -4.409 | 1.146 | 0.8169 | -2.828 | 1.222 | 0.7861 |
| 4 | -3.883 | 1.304 | 0.8463 | -4.063 | 1.114 | 0.9491 | -6.440 | 1.201 | 0.9639 |
| 5 | -4.232 | 1.218 | 0.9740 | -5.079 | 1.275 | 0.8401 | -5.502 | 1.297 | 0.9227 |
| 6 | -3.449 | 1.320 | 1.069 | -4.386 | 1.440 | 1.092 | -1.827 | 1.110 | 0.8114 |
| 7 | -2.661 | 1.068 | 0.7600 | -2.269 | 1.003 | 0.8661 | -3.358 | 0.9067 | 0.6929 |
| 8 | -3.573 | 1.418 | 1.094 | -3.297 | 1.309 | 1.133 | -4.600 | 1.306 | 1.082 |
| 9 | -3.665 | 1.538 | 0.9499 | -2.133 | 1.349 | 0.9147 | -3.717 | 1.113 | 0.9275 |
| 10 | -2.711 | 1.296 | 1.126 | -4.343 | 1.174 | 1.013 | -4.415 | 1.152 | 0.7197 |
| 11 | -3.859 | 1.220 | 0.8807 | -3.221 | 1.286 | 0.9260 | -1.288 | 0.8181 | 0.6380 |
| 12 | -3.479 | 1.292 | 0.9356 | -2.795 | 1.091 | 0.8121 | -2.441 | 0.9957 | 0.7725 |

Table 3. Lift, pitch, and roll control powers for left wing effectors at $\alpha = 4^\circ$, 6° , and 8° .

| Effector Number | $\alpha = 4^\circ$ | | | $\alpha = 6^\circ$ | | | $\alpha = 8^\circ$ | | |
|--------------------|-----------------------|-----------------------|-----------------------|-----------------------|-----------------------|-----------------------|-----------------------|-----------------------|-----------------------|
| | $C_{Ldf} \times 10^4$ | $C_{mdf} \times 10^4$ | $C_{ldf} \times 10^4$ | $C_{Ldf} \times 10^4$ | $C_{mdf} \times 10^4$ | $C_{ldf} \times 10^4$ | $C_{Ldf} \times 10^4$ | $C_{mdf} \times 10^4$ | $C_{ldf} \times 10^4$ |
| 1 | -3.805 | 1.145 | -0.7703 | -5.587 | 1.219 | -0.6466 | -4.793 | 1.191 | -0.8078 |
| 2 | -5.285 | 1.159 | -0.7455 | -4.076 | 1.222 | -0.6429 | -4.133 | 1.249 | -0.7312 |
| 3 | -3.988 | 1.073 | -0.8779 | -2.742 | 1.169 | -0.8866 | -5.321 | 1.313 | -0.8897 |
| 4 | -5.147 | 1.361 | -0.9126 | -3.015 | 1.100 | -0.9136 | -4.772 | 1.277 | -0.8272 |
| 5 | -3.579 | 1.425 | -0.8842 | -5.692 | 1.294 | -0.8262 | -4.209 | 1.232 | -0.9663 |
| 6 | -5.428 | 1.242 | -0.7816 | -2.938 | 1.223 | -0.9099 | -6.856 | 1.293 | -0.7911 |
| 7 | -3.698 | 1.016 | -0.8047 | -3.369 | 1.136 | -0.7502 | -1.788 | 0.8133 | -0.6053 |
| 8 | -4.946 | 1.491 | -1.000 | -2.564 | 1.157 | -0.9833 | -2.950 | 1.148 | -0.8690 |
| 9 | -6.282 | 1.396 | -0.9063 | -3.567 | 1.243 | -0.9479 | -2.078 | 0.9065 | -0.7065 |
| 10 | -3.340 | 1.216 | -0.9281 | -2.692 | 1.225 | -0.9944 | -2.994 | 0.8476 | -0.7917 |
| 11 | -3.285 | 1.190 | -0.9173 | -4.363 | 1.119 | -0.8944 | -1.013 | 0.8564 | -0.7058 |
| 12 | -4.473 | 1.479 | -0.9436 | -3.439 | 1.233 | -0.8852 | -0.9439 | 1.024 | -0.8362 |

7. FIGURES

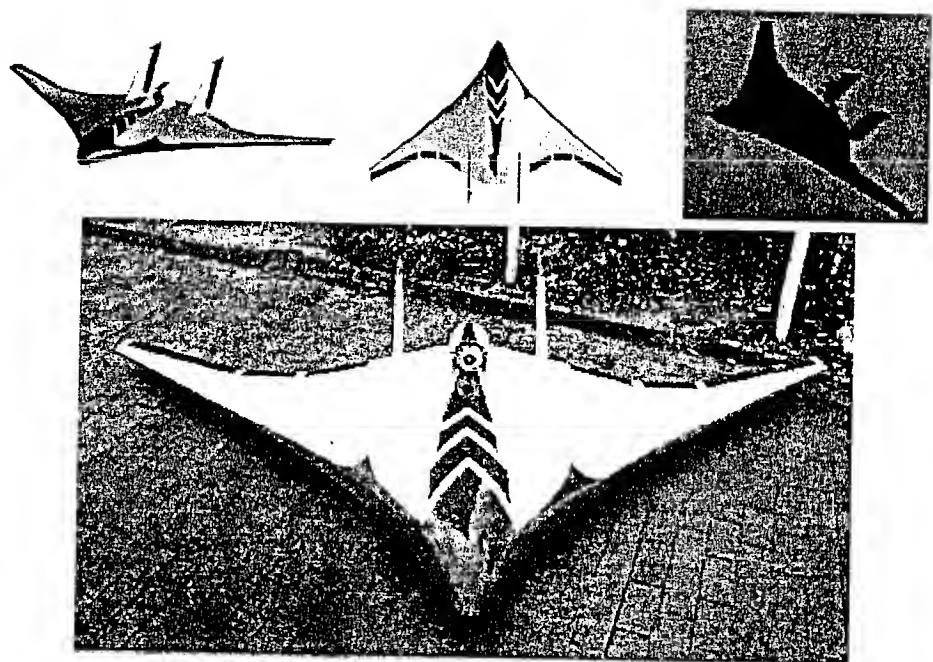


Figure 1. CAD models and photos of *Thunderstruck*.^{1,2}

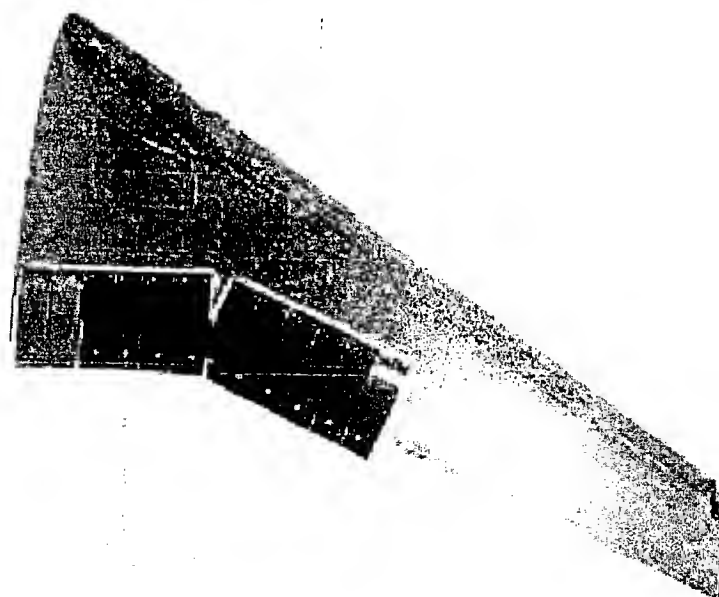


Figure 2. Completed effector and sensor array installed on starboard wing.²

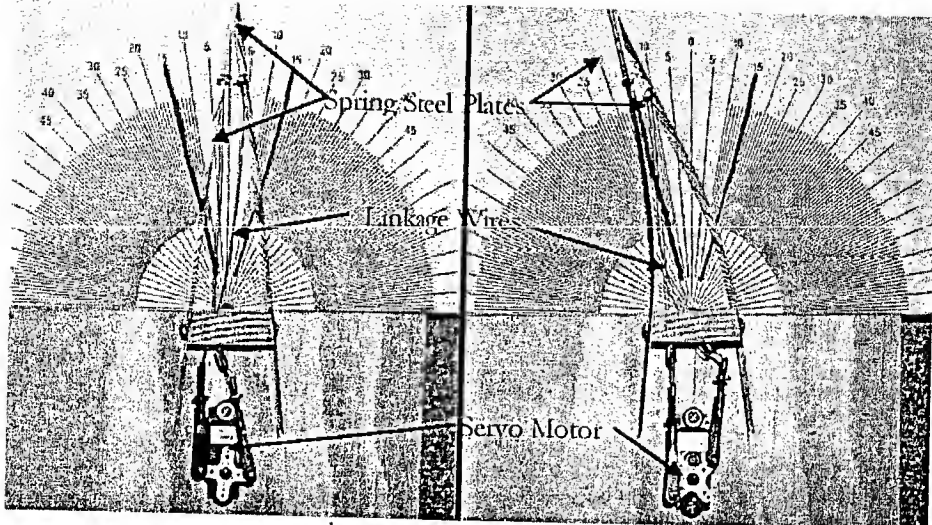


Figure 3. Prototype build of pull-pull servo linkages for effector.²

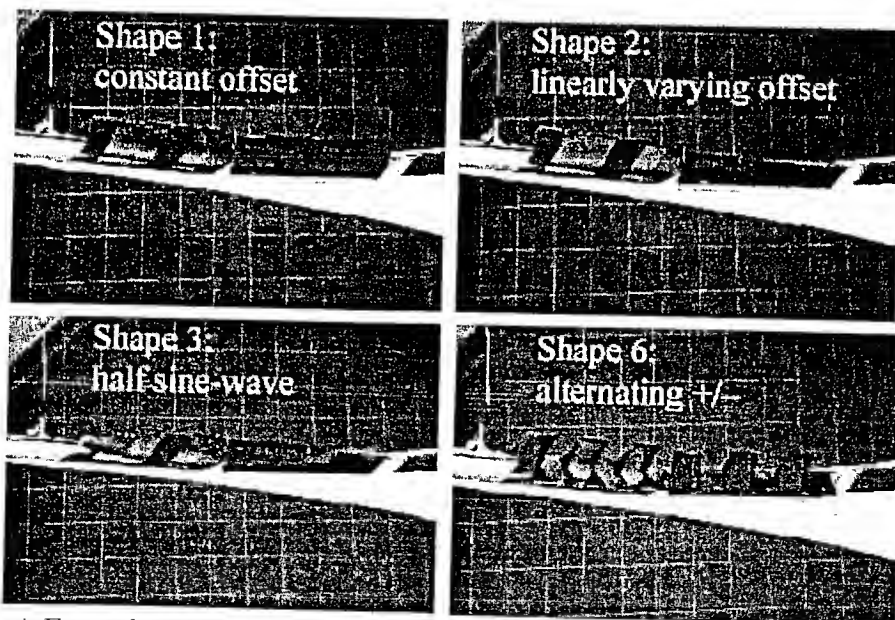


Figure 4. Examples of effector shape deflections for shapes 1, 2, 3, and 6 on port wing.¹

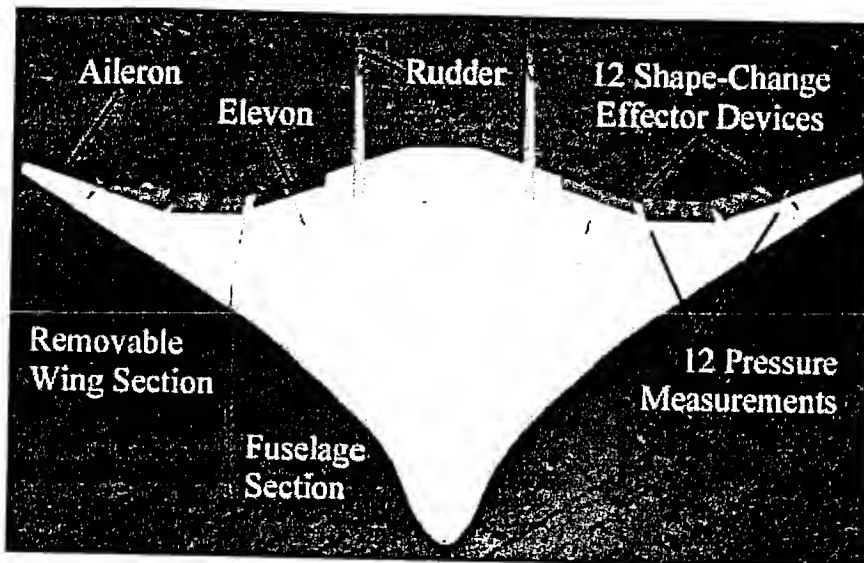


Figure 5. Complete MESA testbed with effector array installed.¹

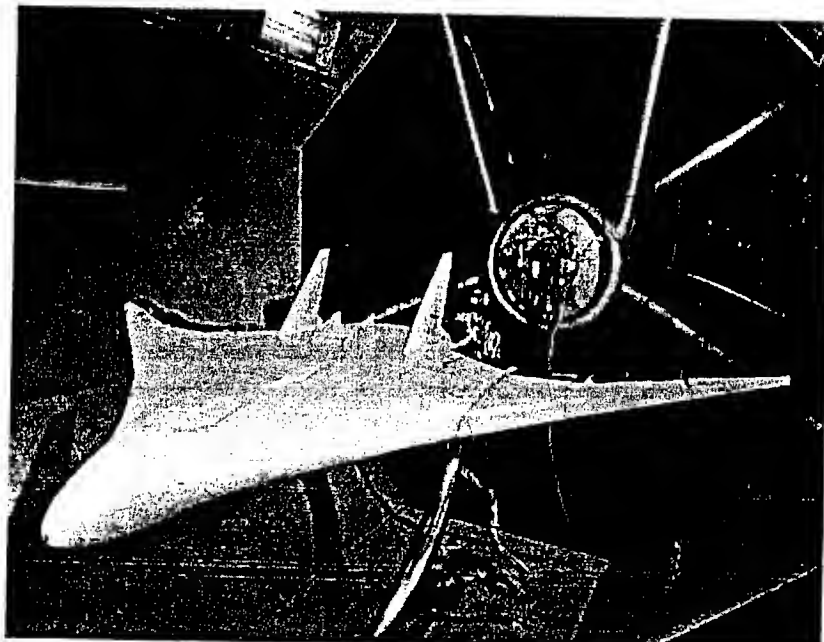


Figure 6. MESA testbed installed in the NASA Langley 12-Foot Wind Tunnel.

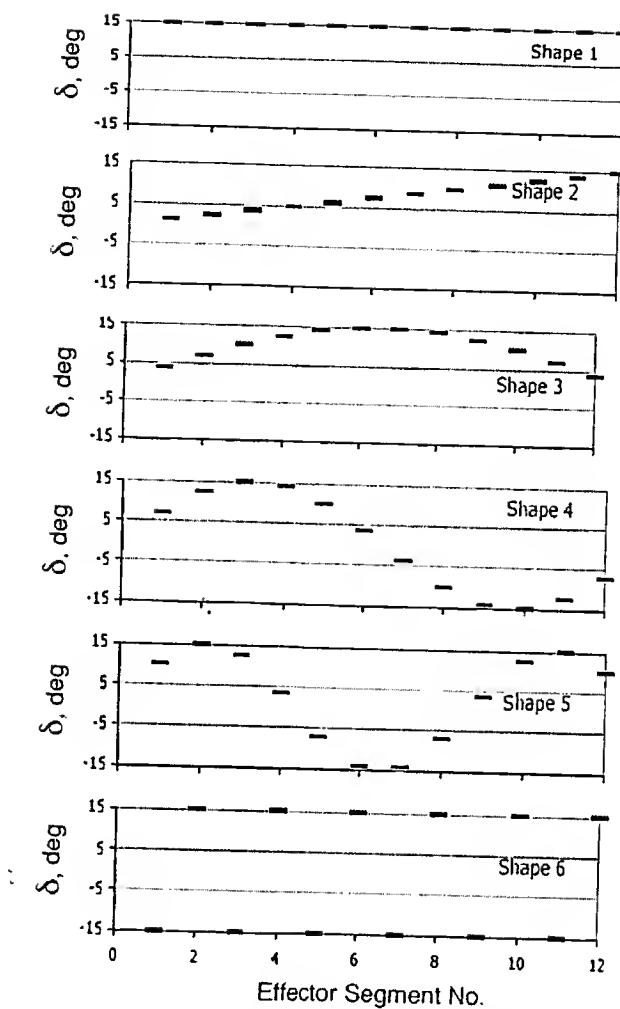


Figure 7. Effector deflection schemes for the 6 shapes with a scaling factor of 15° .¹

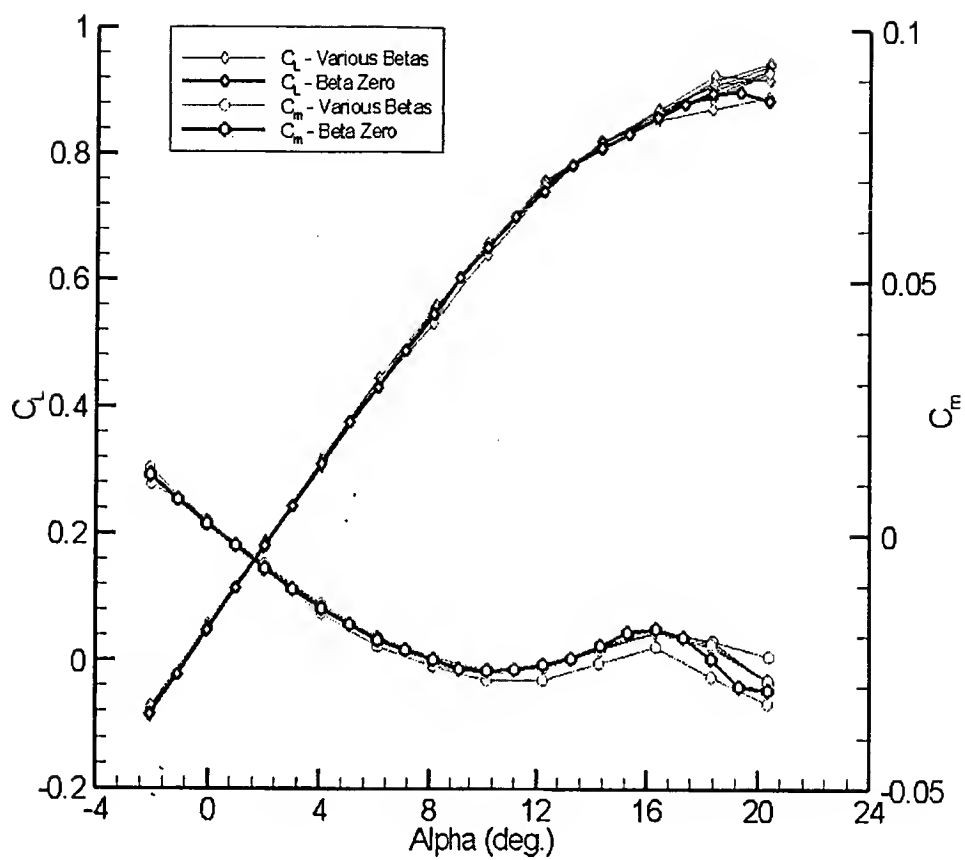


Figure 8. Lift and pitching moment coefficient curves for sideslip β 's ranging -5° to $+5^\circ$ with emphasis on 0° sideslip case.

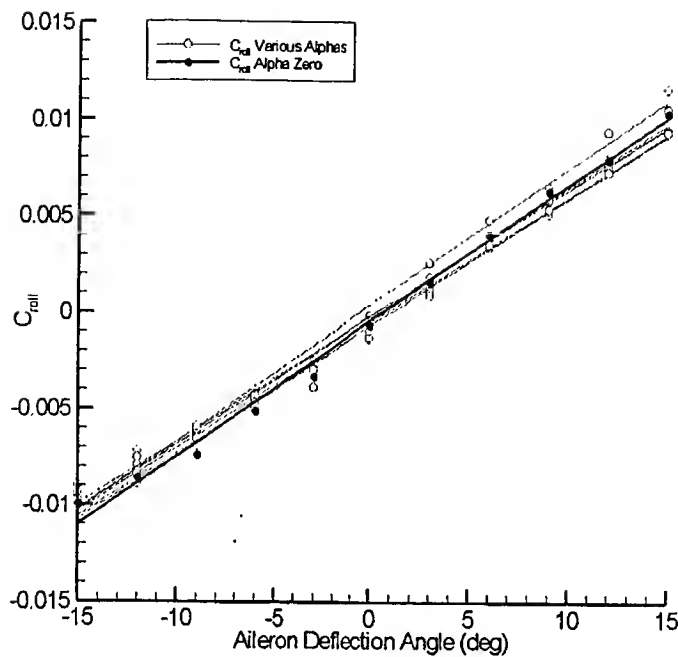


Figure 9. Rolling moment curve coefficient for anti-symmetric ailerons for a range of -2° to $+20^\circ$ with emphasis on 0° case.

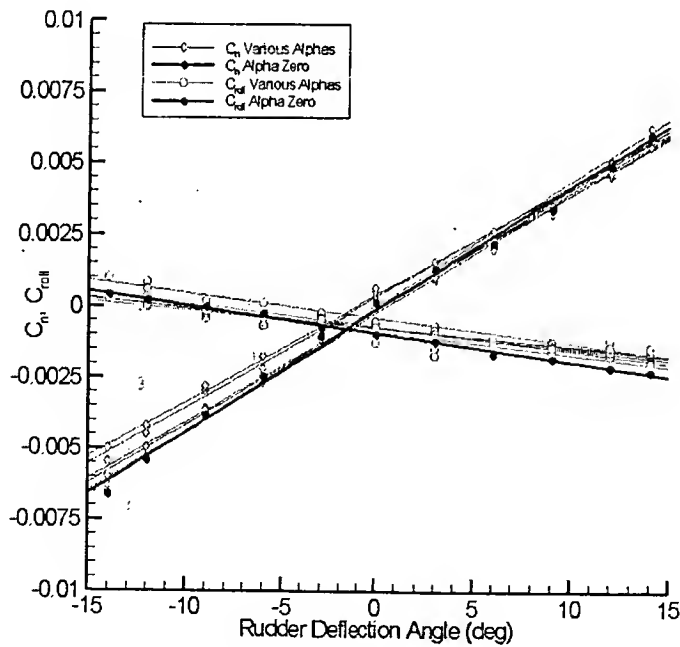


Figure 10. Yawing and rolling moment coefficient curves for rudders for a range of -2° to $+20^\circ$ with emphasis on 0° case.

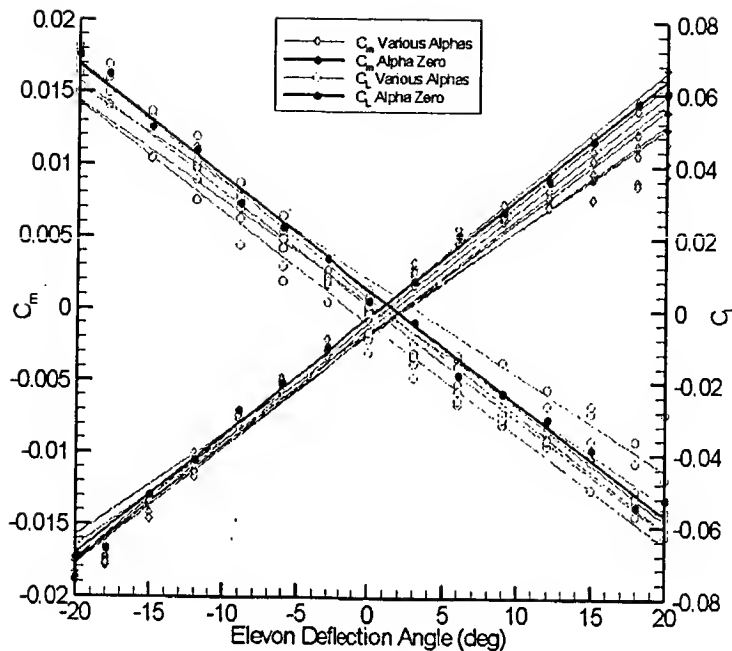


Figure 11. Pitching moment and lift coefficient curves for elevons for a range of -2° to $+20^\circ$ with emphasis on 0° case.

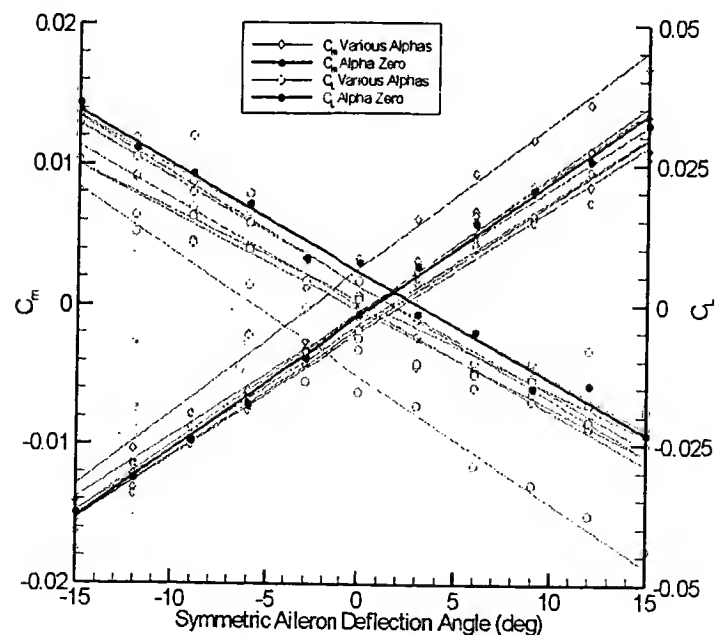


Figure 12. Pitching moment and lift coefficient curves for symmetric ailerons for a range of -2° to $+20^\circ$ with emphasis on 0° case.

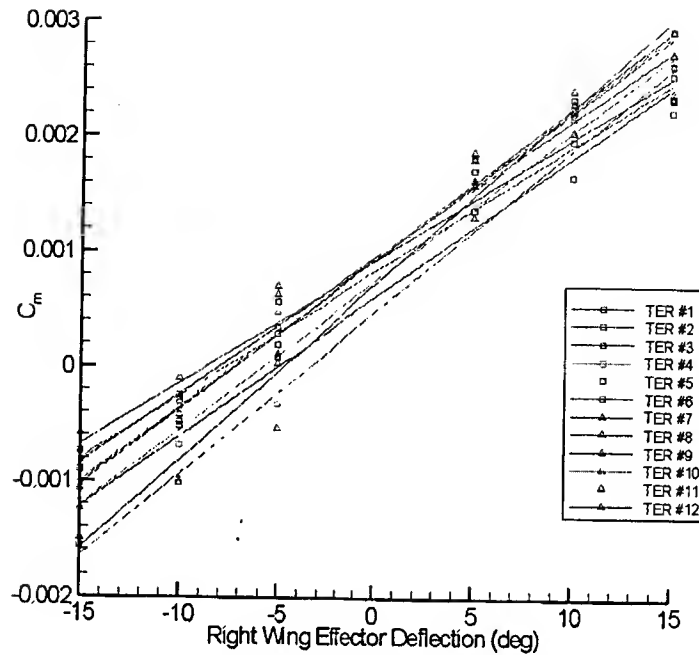


Figure 13. Pitching moment curve for right wing effectors at $\alpha=4^\circ$.

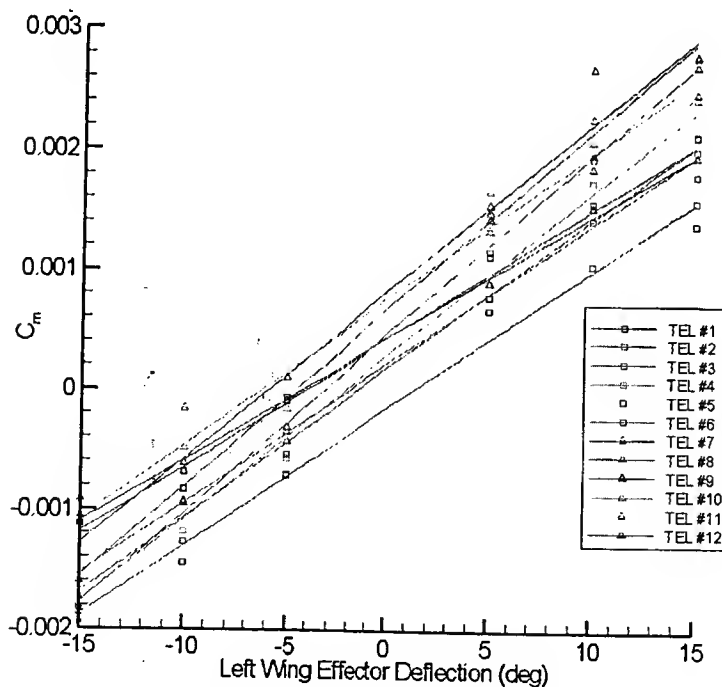


Figure 14. Pitching moment curve for left wing effectors at $\alpha=4^\circ$.

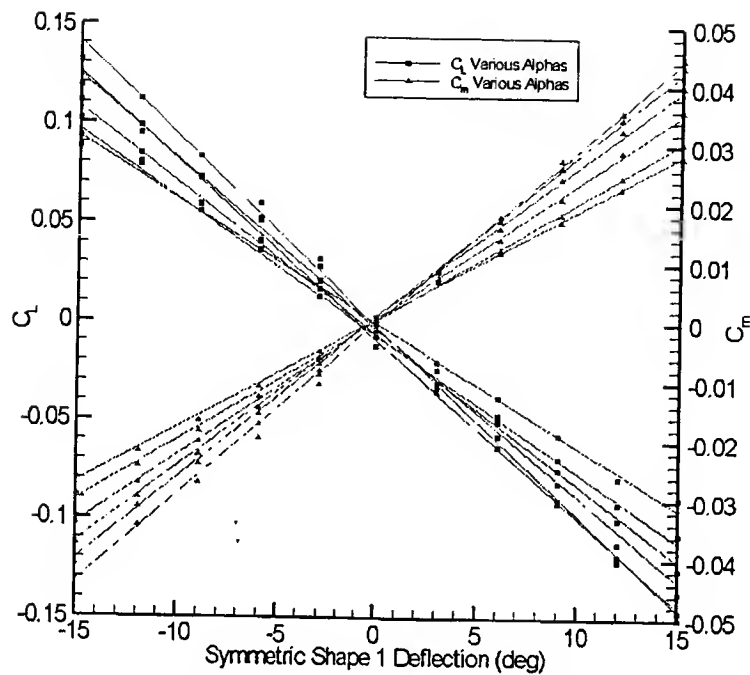


Figure 15. Lift and pitching moment curves for symmetric shape 1 deflections for a range of $+2^\circ$ to $+12^\circ$.

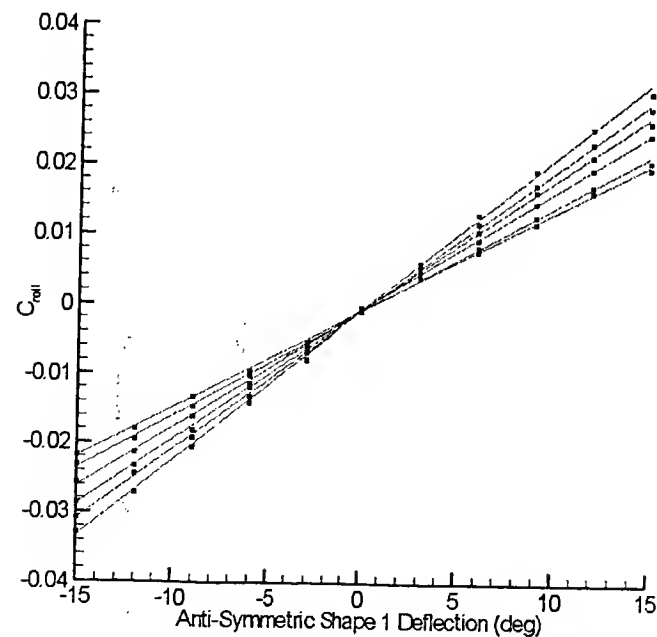


Figure 16. Rolling moment curves for anti-symmetric shape 1 deflections for a range of $+2^\circ$ to $+12^\circ$.

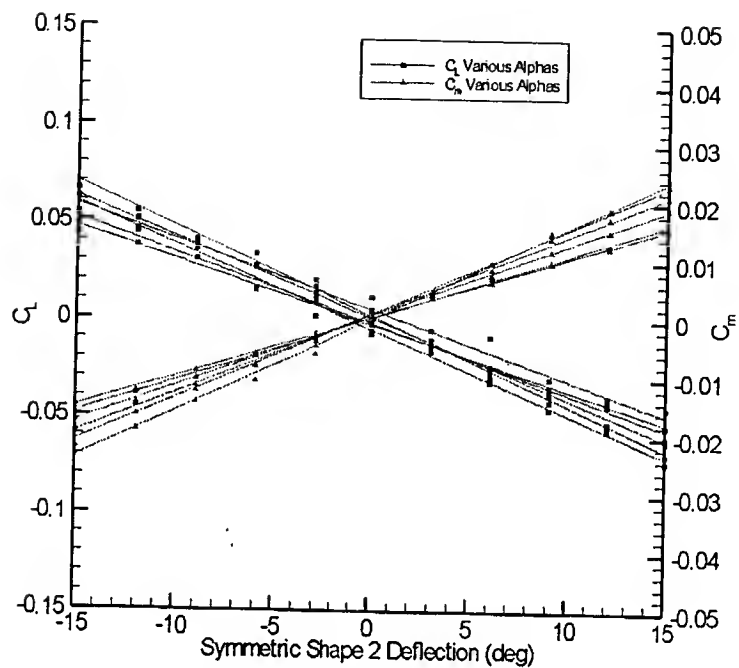


Figure 17. Lift and pitching moment curves for symmetric shape 2 deflections for a range of $+2^\circ$ to $+12^\circ$.

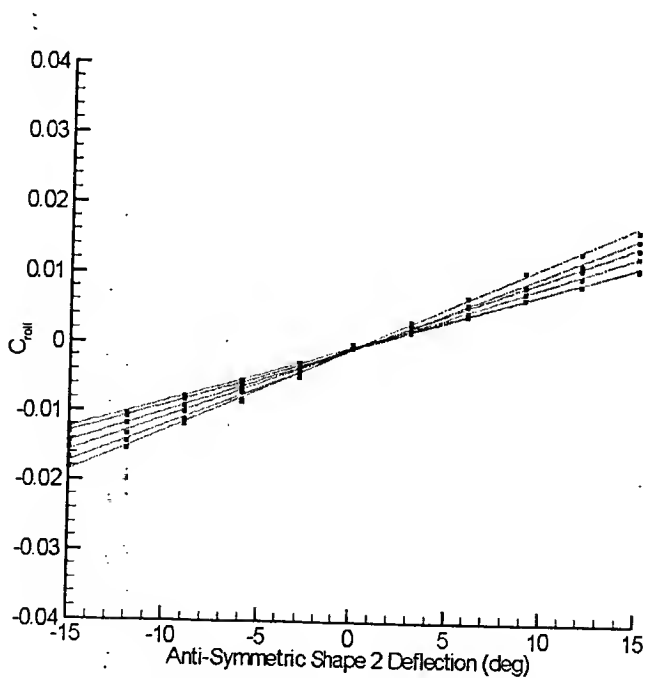


Figure 18. Rolling moment curves for anti-symmetric shape 2 deflections for a range of $+2^\circ$ to $+12^\circ$.

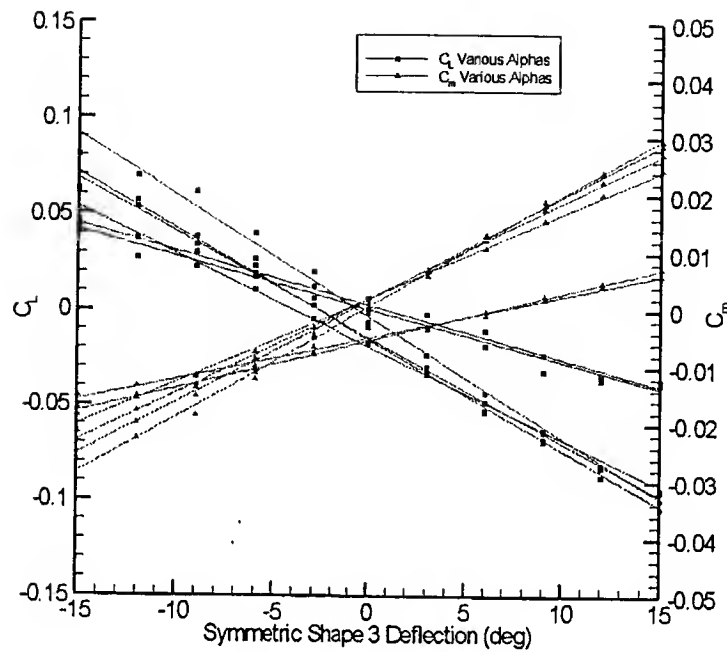


Figure 19. Lift and pitching moment curves for symmetric shape 3 deflections for a range of $+2^\circ$ to $+12^\circ$.

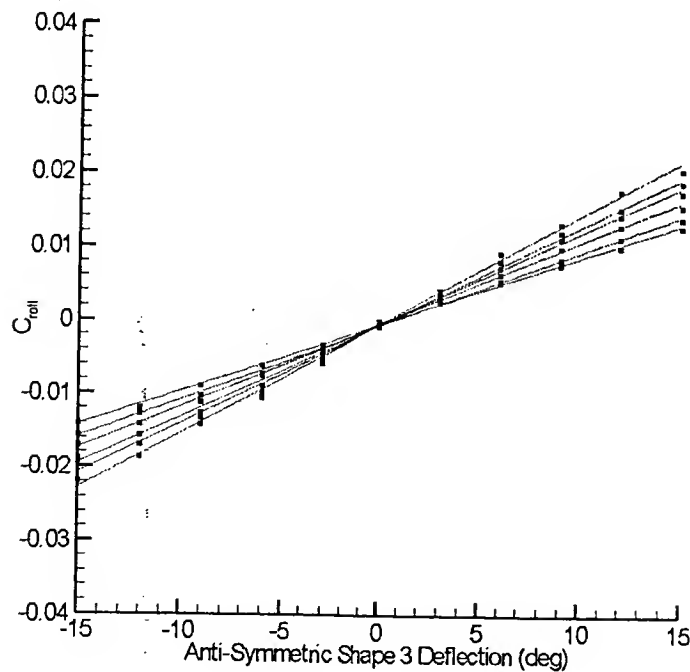


Figure 20. Rolling moment curves for anti-symmetric shape 3 deflections for a range of $+2^\circ$ to $+12^\circ$.

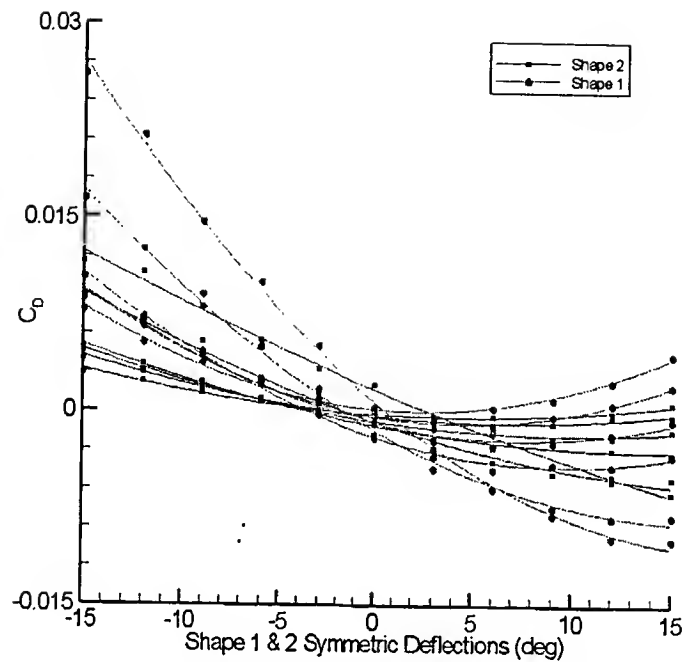


Figure 21. Drag coefficient comparison for symmetric shapes 1 and 2 deflections for a range of $+2^\circ$ to $+12^\circ$.

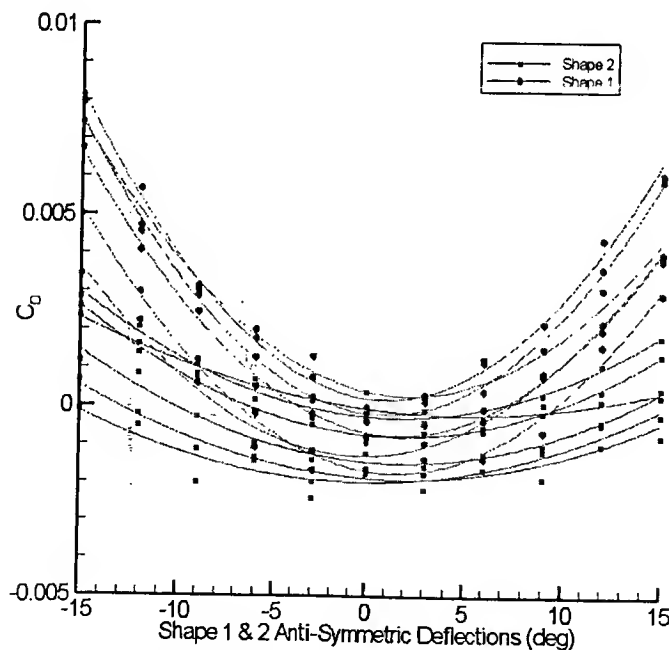


Figure 22. Drag coefficient comparison for anti-symmetric shapes 1 and 2 deflections for a range of $+2^\circ$ to $+12^\circ$.

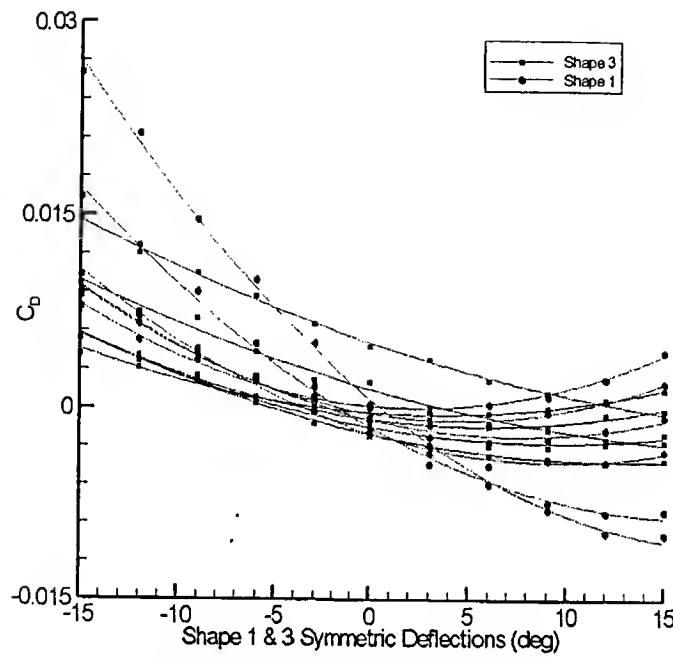


Figure 23. Drag coefficient comparison for symmetric shapes 1 and 3 deflections for a range of $+2^\circ$ to $+12^\circ$.

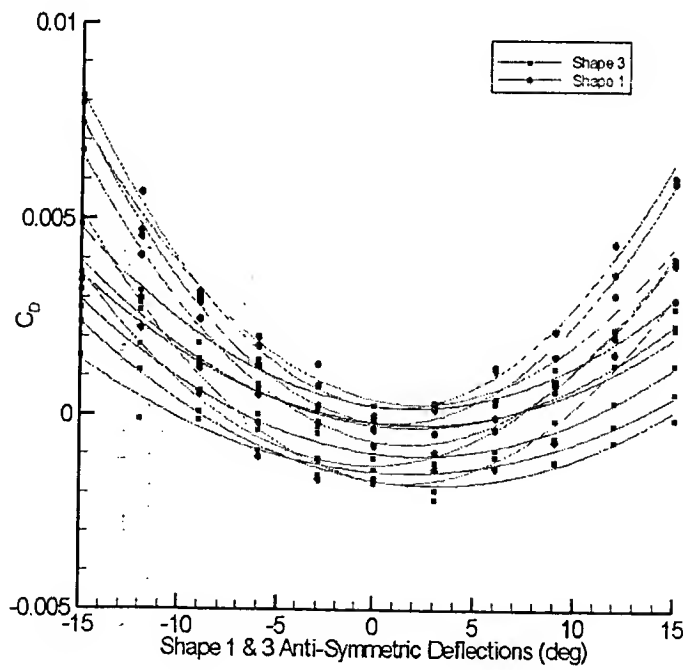


Figure 24. Drag coefficient comparison for anti-symmetric shapes 1 and 3 deflections for a range of $+2^\circ$ to $+12^\circ$.

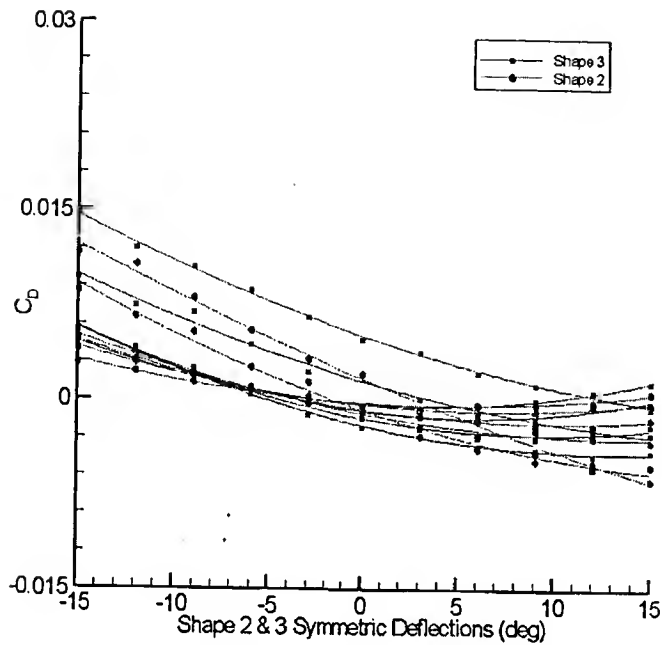


Figure 25. Drag coefficient comparison for symmetric shapes 2 and 3 deflections for a range of $+2^\circ$ to $+12^\circ$.

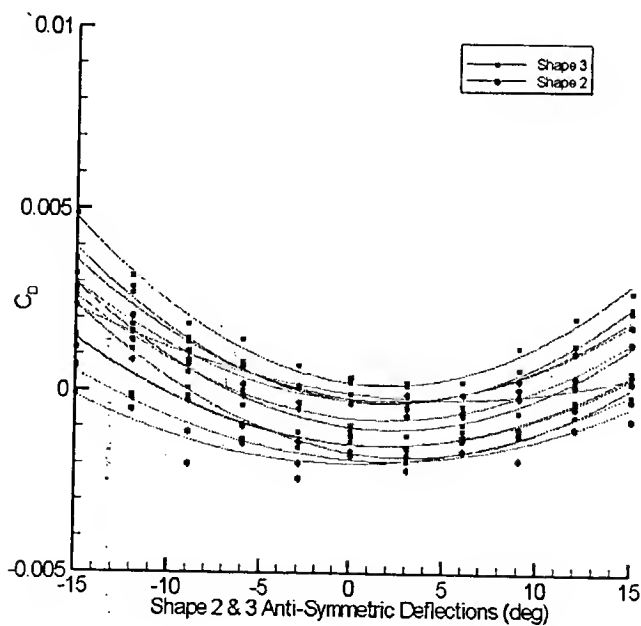


Figure 26. Drag coefficient comparison for anti-symmetric shapes 2 and 3 deflections for a range of $+2^\circ$ to $+12^\circ$.

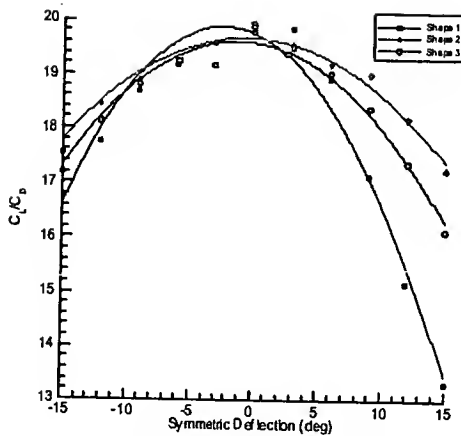


Figure 27. Lift to drag ratio for shapes 1, 2, and 3 at $a = +6^\circ$.

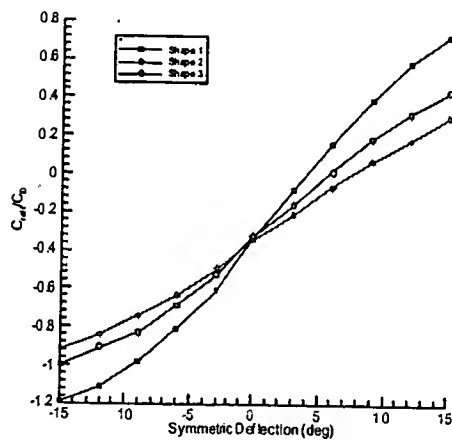


Figure 28. Rolling moment to drag ratio for shapes 1, 2, and 3 at $a = +6^\circ$.

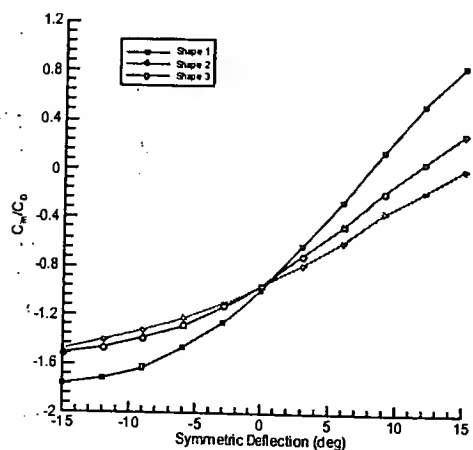


Figure 29. Pitching moment to drag ratio for shapes 1, 2, and 3 at $a = +6^\circ$.

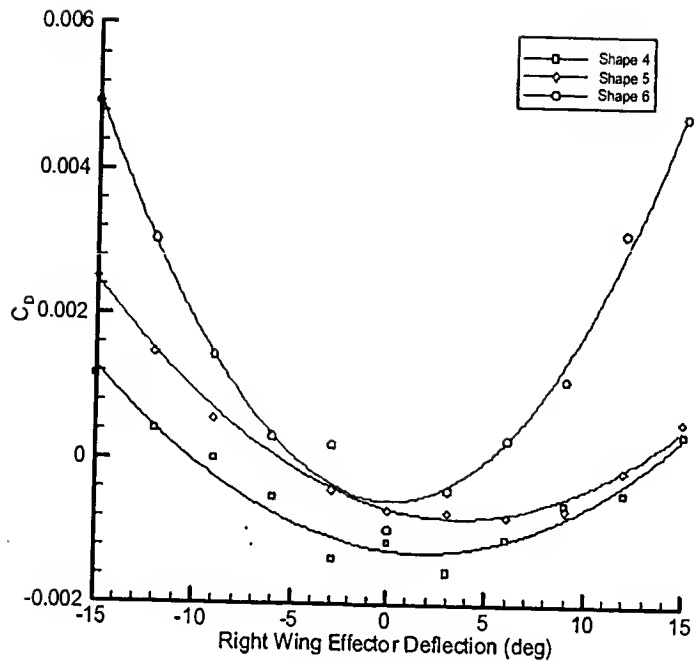


Figure 30. Drag coefficient for right wing deflections in shapes 4, 5, and 6 at $\alpha = +6^\circ$.

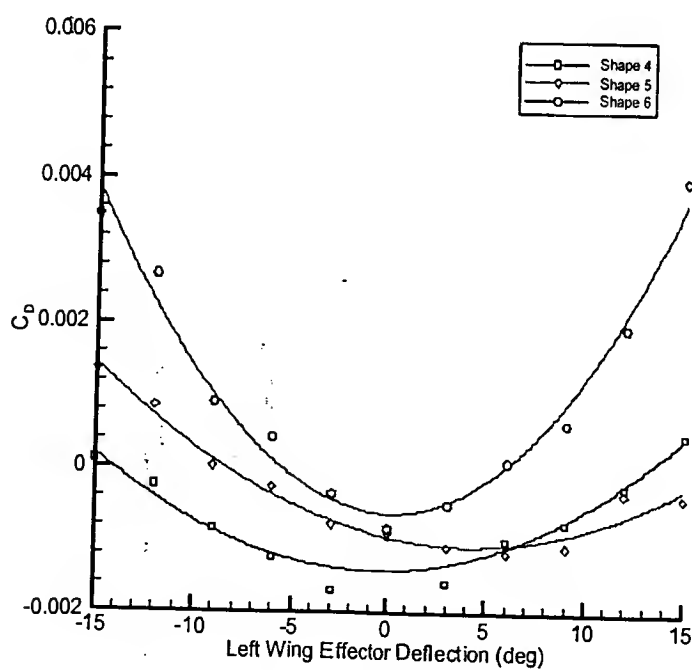


Figure 31. Drag coefficient for left wing deflections in shapes 4, 5, and 6 at $\alpha = +6^\circ$.

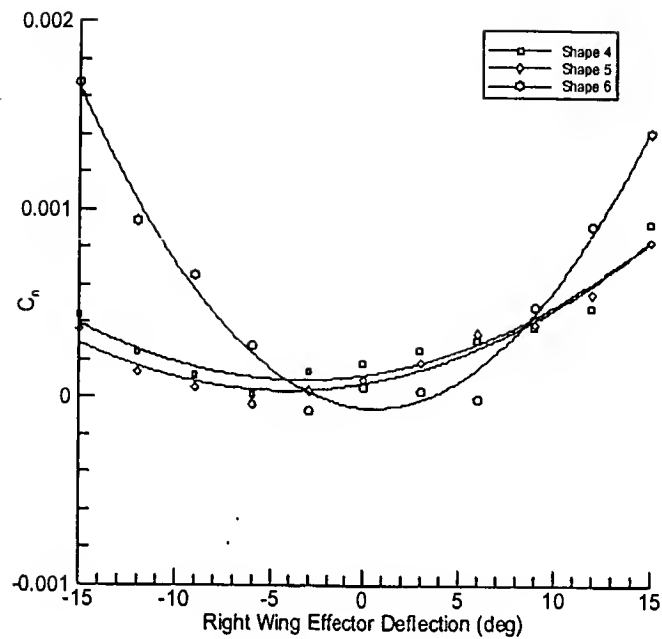


Figure 32. Yawing moment coefficient for right wing deflections in shapes 4, 5, and 6 at $\alpha = +6^\circ$.

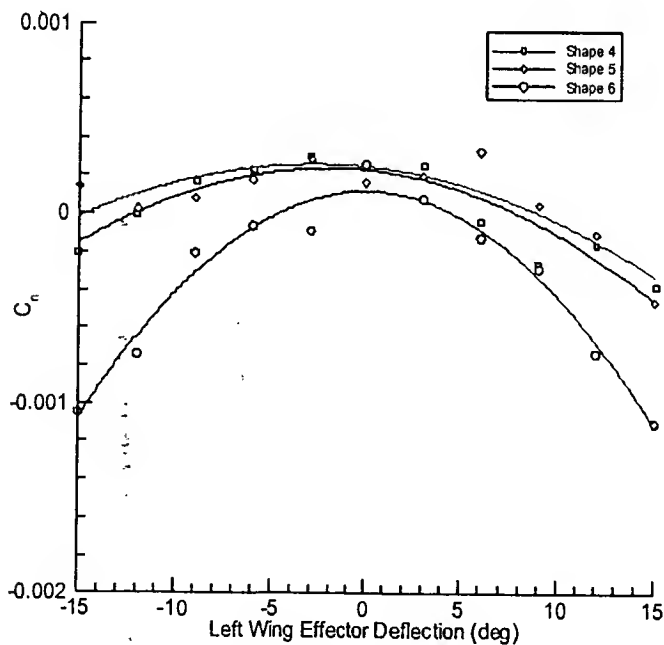


Figure 33. Yawing moment coefficient for right wing deflections in shapes 4, 5, and 6 at $\alpha = +6^\circ$.

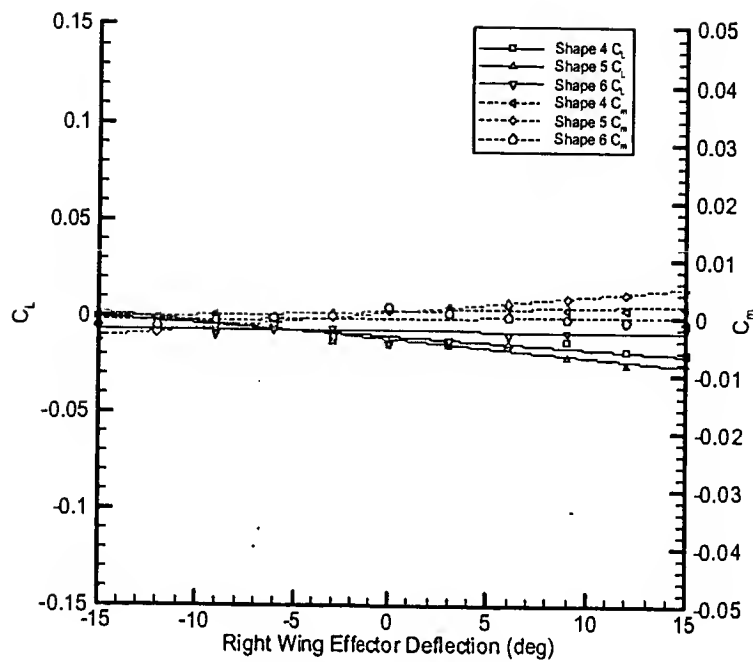


Figure 34. Pitching moment and lift coefficients for right wing deflections in shapes 4, 5, and 6 at $\alpha = +6^\circ$.

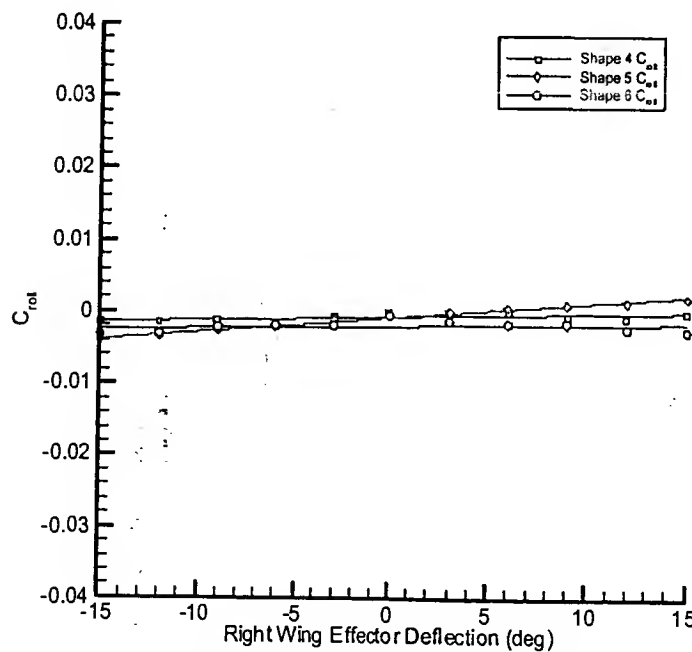


Figure 35. Rolling moment coefficient for right wing deflections in shapes 4, 5, and 6 at $\alpha = +6^\circ$.

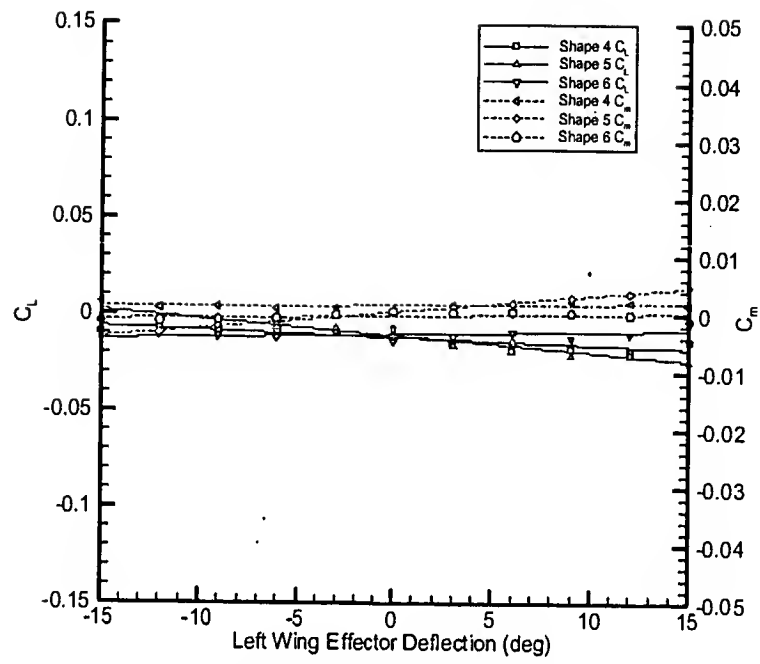


Figure 36. Pitching moment and lift coefficients for left wing deflections in shapes 4, 5, and 6 at $\alpha = +6^\circ$.

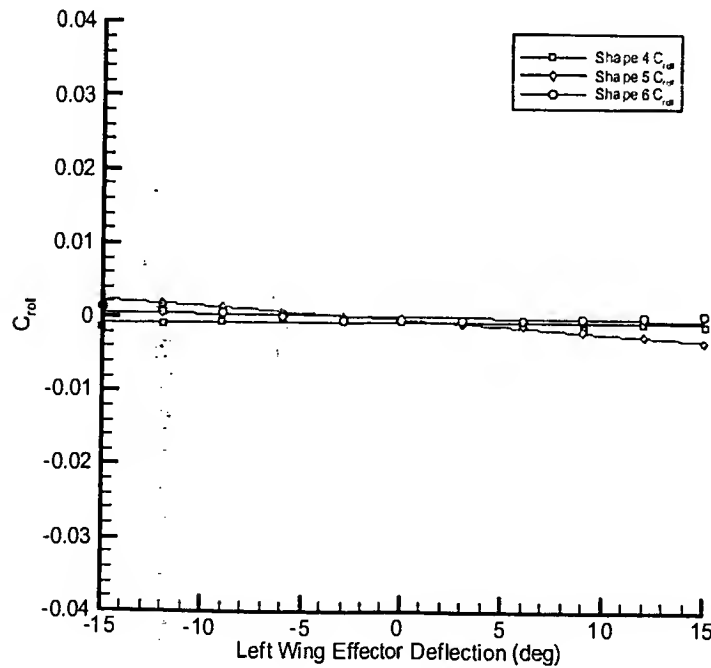


Figure 37. Rolling moment coefficient for left wing deflections in shapes 4, 5, and 6 at $\alpha = +6^\circ$.

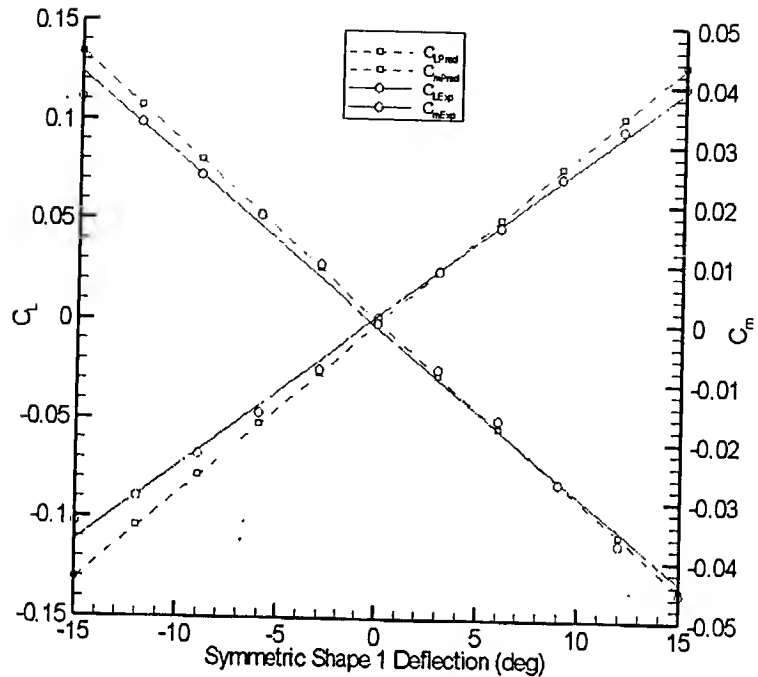


Figure 38. Predicted and experimental pitching moment and lift coefficients for symmetric shape 1 deflections at $\alpha = +6^\circ$.

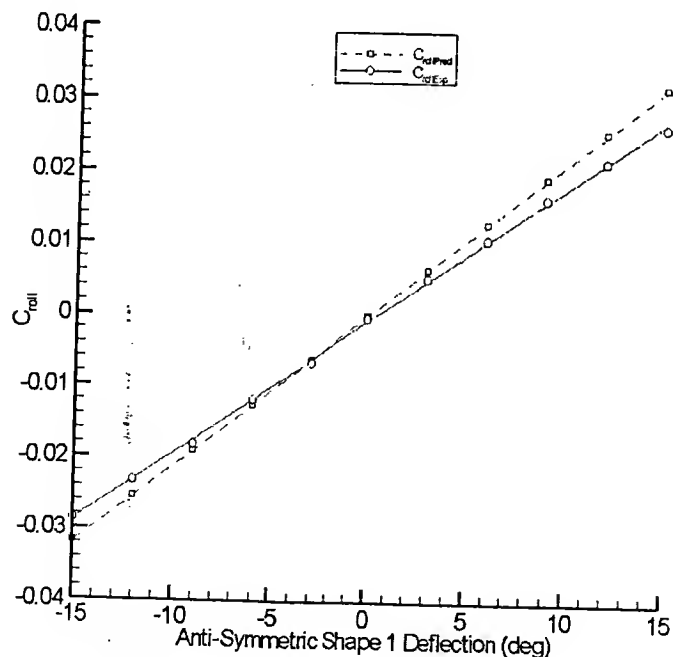


Figure 39. Predicted and experimental rolling moment coefficient for anti-symmetric shape 1 deflections at $\alpha = +6^\circ$.

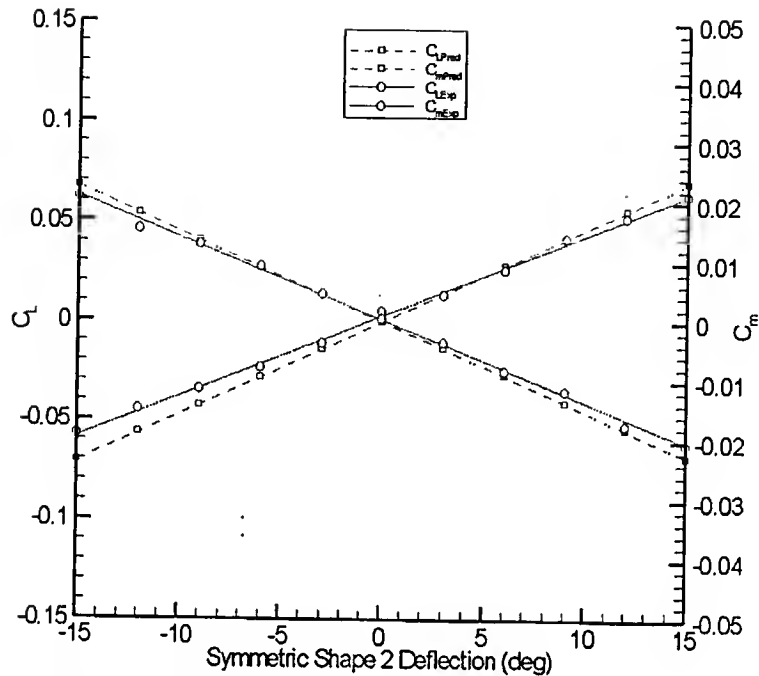


Figure 40. Predicted and experimental pitching moment and lift coefficients for symmetric shape 2 deflections at $\alpha = +6^\circ$.

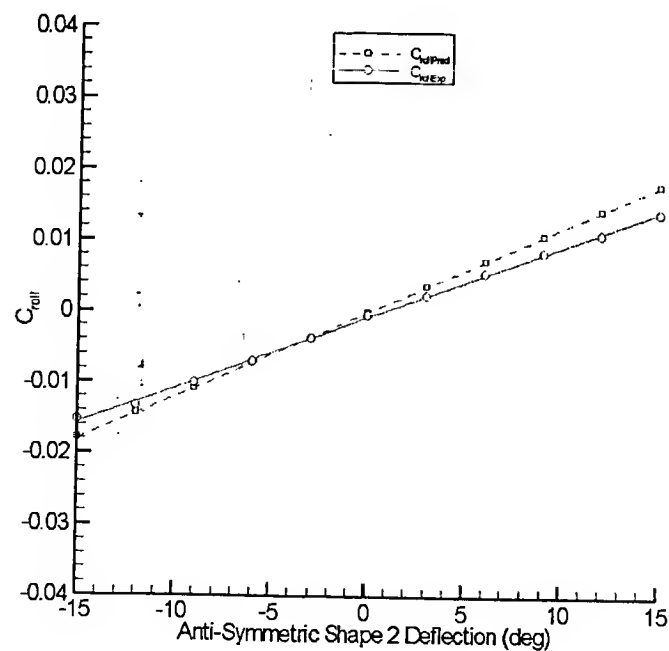


Figure 41. Predicted and experimental rolling moment coefficient for anti-symmetric shape 2 deflections at $\alpha = +6^\circ$.

8. REFERENCES

1. Raney, David L.; Cabell, Randolph H.: "Wind Tunnel Test of an RPV with Shape-Change Control Effector and Sensor Arrays", AIAA paper 2004-5114, August 2004.
2. Barnwell, William G.: *Distributed Actuation and Sensing on an Uninhabited Aerial Vehicle*, Thesis for Master of Science in Aerospace Engineering at North Carolina State University, MAE Dept, August 2003.
3. Liebeck, R.H.; Page, M.A.: "Evolution of the Revolutionary Blended-Wing-Body", NASA Center for Aerospace Information, 1996.
4. "UAV *Thunderstruck*: Fall Report," NC State University Senior Aircraft Design Class: Fall Report, December, 2001.
5. "UAV *Thunderstruck*: Spring Report," NC State University Senior Aircraft Design Class: Spring Report, May, 2002..